Max-Planck-Institut für Metallforschung
Stuttgart

Grain growth and texture evolution in copper thin films

Petra Sonnweber-Ribic

Dissertation
an der
Universität Stuttgart

Bericht Nr. 228
September 2010

GRAIN GROWTH AND TEXTURE EVOLUTION IN COPPER THIN FILMS

Von der Fakultät Chemie der Universität Stuttgart
zur Erlangung der Würde eines Doktors der
Naturwissenschaften (Dr. rer. nat.) genehmigte Abhandlung

Vorgelegt von

Petra Sonnweber-Ribic

aus Ehenbichl, Österreich

Hauptberichter: Prof. Dr. phil. Eduard Arzt
Mitberichter: Prof. Dr. rer. nat. Horst P. Strunk

Tag der mündlichen Prüfung: 27.09.2010

Institut für Materialwissenschaft der Universität Stuttgart
und
Max-Planck-Institut für Metallforschung Stuttgart

2010

Petra Sonnweber-Ribic

GRAIN GROWTH AND TEXTURE EVOLUTION IN COPPER THIN FILMS

Max Planck Institute for Metals Research and
Institut für Materialwissenschaft, University of Stuttgart;

Abstract

An improved basic understanding of mechanisms causing grain growth and texture evolution in Cu thin films contains the potential to improve performance and reliability of components and devices. In this work, the influence of film thickness, strain and temperature on grain growth and texture evolution in Cu thin films was investigated. By varying the parameters, information about the underlying mechanisms were revealed.

The 0.5 to 10 µm thick Cu films were deposited on 125 µm thick polyimide substrates (Kapton®, DuPont) using a UHV magnetron sputtering system. For detailed observation of grain growth and texture evolution an EBSD-based *in situ* testing appliance was constructed. This system allowed the simultaneous observation of grain growth and texture evolution, giving new insight into growth kinetics and details of grain growth.

In a first step, Cu thin films of thicknesses in between 0.5 and 10 µm were deposited on polymer substrates and annealed at 330°C for 30 min. Their resulting texture and microstructure were investigated by EBSD. A texture transition from (111) to (100) was observed at film thicknesses between 3 and 5 µm. The experimental findings were explained by the texture evolution model of Thompson and Carel. A significant observation which cannot be explained by a purely energetic argument is the broad texture transition. In order to get more information about the critical role of strain energy, uniaxial tensile tests were carried out on 3 µm thick films. In contrast to theoretical predictions, various tensile tests revealed no influence of strain on grain growth behaviour. Neither at room temperature nor at elevated temperatures, further (100) grain growth was observed. In a next step, the abnormal growth of individual (100) oriented grains was recorded for more than 24 hours at temperatures between 90 and 118°C. Annealing was carried out inside a Leo 1530-VP SEM equipped with a heating facility. Detailed analysis of grain growth and estimates of the possibly acting driving forces indicated that the reduction of dislocation density played an important role for abnormal grain growth. A further hint for the critical importance of defect density was given by the HWHM of the (100) texture fraction. Nevertheless, it was not clear why this driving force favours the growth of (100) oriented grains. A possible answer could be given by the strain energy release maximization (SERM) model developed by Lee. In addition, when analysing the activation energy for grain growth, they were found to possess a higher grain boundary mobility, supporting the preferred growth of (100) oriented grains. A new texture map, considering dislocation density as driving force, was constructed.

Assuming dislocation density to play a significant role for grain growth and texture evolution in Cu thin films, the influence of deposition parameters is pointed out.

Petra Sonnweber-Ribic

KORNWACHSTUM UND TEXTURENTWICKLUNG IN DÜNNEN KUPFERSCHICHTEN

Max-Planck-Institut für Metallforschung und
Institut für Materialwissenschaft, Universität Stuttgart

Kurzzusammenfassung

Ein verbessertes Verständnis der Texturentwicklung in dünnen Kupferschichten ist ein Beitrag, um Zuverlässigkeit und akzeptable Lebensdauer von elektronischen Geräten gewährleisten zu können. In dieser Doktorarbeit wurde der Einfluss von Schichtdicke, Spannung und Temperatur auf das Kornwachstum und die Texturentwicklung in dünnen Kupferschichten untersucht. Durch die Variation der unterschiedlichen Parameter war es möglich zugrunde liegende Mechanismen zu identifizieren.

Experimente wurden an Cu-Schichten mit Schichtdicken zwischen 0.5 und 10 µm durchgeführt. Die Proben wurden mittels Magnetron-Sputterns im Ultrahochvakuum hergestellt. Als Substrat wurde ein Polyimid (Kapton HN, DuPont) verwendet. Zur detaillierten Untersuchung des Kornwachstums und der damit verbundenen Texturentwicklung wurde eine *in situ* Apparatur entworfen, die es erlaubt im Rasterelektronenmikroskop Zugversuche und/oder Glühexperimente durchzuführen und dabei die Probe simultan mithilfe eines EBSD-Systems zu untersuchen.

Die Analyse der Textur von 500 nm bis 10 µm dicken Schichten, die direkt nach der Abscheidung für 30 min bei 330°C ausgelagert worden waren, brachte einen Texturwechsel von einer dominierenden (111) zu einer (100) Textur mit zunehmender Schichtdicke zu Tage. Der Wechsel der Textur erfolgt zwischen von 3 und 5 µm Schichtdicke. Vergleicht man diese Resultate mit den Vorhersagen des Texturentwicklungsmodells von Thompson und Carel, so können sie durch die Dominanz unterschiedlicher orientierungsabhängiger Triebkräfte beschrieben werden. Für den beobachteten, langsamen Wechsel der Texturen liefert dieses Modell jedoch keine Erklärung. Um die Rolle der Verzerrungsenergieminimierung genauer untersuchen zu können, wurden in einem nächsten Schritt einachsige Zugversuche an 3 µm dicken Cu-Schichten durchgeführt. Allerdings konnte das vom Texturmodell vorhergesagte Verhalten weder bei Raumtemperatur noch bei erhöhten Temperaturen beobachtet werden. Um diese Fragen klären zu können, wurden im nächsten Schritt systematisch *in situ* Glühexperimente für 1, 2, 3 und 5 µm dicke Schichten bei 90, 104 und 118°C durchgeführt. Die Untersuchung der daraus resultierenden Wachstumsgeschwindigkeit und die Bestimmung der Versetzungsdichte aus Röntgenmessungen konnten zeigen, dass die Versetzungsdichte eine wichtige Rolle als Triebkraft spielt. Durch diese Erkenntnis konnten nicht nur die erhaltenen Ergebnisse erklärt sondern auch offene Fragen aus der Literatur beantwortet werden. Diese Triebkraft allein konnte aber noch nicht erklären, warum die (100) orientierten Körner bevorzugt wachsen. Erst eine Abschätzung der Mobiltiät sowie das SERM-Modell von Lee lieferten mögliche Begründungen dafür. Durch die Identifikation der dominierenden Triebkraft wird die Bedeutung der Abscheideparameter deutlich, wodurch sich Möglichkeiten zur Einflussnahme auf die Texturentwicklung ergeben.

Danksagung

Die vorliegende Doktorarbeit wurde zwischen Mai 2004 und September 2010 am Max-Planck-Institut für Metallforschung in Stuttgart und dem Institut für Materialwissenschaft der Universität Stuttgart angefertigt.

Herrn Prof. Dr. Eduard Arzt gilt mein besonderer Dank für die Möglichkeit in seiner Abteilung zu promovieren, für die Betreuung der Doktorarbeit, die Übernahme des Hauptberichts und für die Unterstützung meiner Arbeit.

Bei Herrn Prof. Dr. Horst Strunk möchte ich mich ganz herzlich für die kurzfristige Übernahme des Mitberichts und das Interesse an meiner Arbeit bedanken.

Auch Herrn Prof. Dr. Gerhard Dehm danke ich für das Interesse an meiner Arbeit und für die Zeit, die er sich als Betreuer für mich genommen hat. Seine freundliche und positive Art war beeindruckend. Er hatte stets ein offenes Ohr für mich – selbst nach seinem Weggang aus Stuttgart stand er mir immer für Fragen zur Verfügung.

Bei Herrn Dr. Patric Gruber möchte ich mich ganz herzlich für die fachliche und freundschaftliche Unterstützung und Betreuung meiner Arbeit bedanken. Auch er stand mir immer für Fragen zur Verfügung – auch nach seinem Weggang aus Stuttgart. Besonders dankbar bin ich für die Kommentare zu meiner Arbeit und investierte Nachtschichten!

Ganz herzlichen Dank auch an das Dünnschichtlabor für die Herstellung der Schichten. Besonderer Dank gebührt in diesem Zusammenhang Frau Ilse Lakemeyer und Herrn Dr. Gunther Richter.

Besonders möchte ich mich bei der Christiane-Nüsslein-Volhard-Stiftung bedanken. Ohne ihre Unterstützung wären viele der zeitaufwändigen *In situ* Experimente nicht möglich gewesen. Herzlichen Dank dafür!

Bei Herrn Berkhemer möchte ich mich aufrichtig für die Unterstützung bei der Planung der Versuchsapparatur bedanken. Ganz besonderen Dank schulde ich in diesem Zusammenhang auch der Feinmechanischen Werkstatt und hier besonders Herrn Manfred Binder.

Für die Durchführung der Röntgenuntersuchungen bedanke ich mich bei Herrn Dr. Udo Welzel, Herrn Gerd Maier und Herrn Yener Kuru. Bei Herrn Welzel möchte ich mich auch für die freundliche Hilfe und hilfreiche Diskussionen bedanken. Außerdem möchte ich mich ganz besonders bei Herrn Yener Kuru bedanken, der röntgenographische Spannungsmessungen durchgeführt und Versetzungsdichten bestimmt hat. Seine Hilfsbereitschaft und Freundlichkeit waren beeindruckend.

Ein großes Dankeschön gebührt auch Herrn Kim Larsen für die Einweisung in die EBSD-Methode und die schnelle Hilfe bei Softwareproblemen.

Bei allen Arbeitskollegen möchte ich mich für die tolle Atmosphäre bedanken – es war mir jeden Tag eine Freude zur Arbeit zu gehen. Ganz besonders möchte ich mich dabei auch beim Herz unserer Abteilung – Frau Jutta Heß - für ihre Hilfe und ihr Engagement bedanken. Besonderes Glück hatte ich auch mit meinen Zimmerkollegen: Frau Boriana Rashkova, Frau Melanie Wirkner und Herrn Lifeng Ma. Es war eine wirkliche Freude mit ihnen zu arbeiten.

Meinen Kommilitonen Anja Krug, Steffen Orso, Holger Pfaff und Patric Gruber möchte ich für die freundschaftliche Unterstützung in all der Zeit danken.

Bei Herrn Prof. Dr. Helmut Clemens möchte ich mich noch für den Tipp „was Gscheides“ zu studieren bedanken!

Zum Abschluss will ich mich bei meiner Familie bedanken. Besonders meinem Mann, der mich immer ermutigt hat, unzählige Seiten Korrektur gelesen und Vorträge angehört hat, gebührt hier besonderer Dank. Mittlerweile hat er wohl schon eine werkstoffwissenschaftliche Grundausbildung absolviert.

Auch bei meinen Kindern möchte ich mich herzlich bedanken – dafür, dass sie meine Arbeit immer als etwas Positives und Faszinierendes betrachtet haben und Wissenschaft „echt cool“ finden.

Und ganz besonders möchte ich mich noch bei meinen Eltern bedanken – sie haben mir mein Studium erst ermöglicht, waren stets offen für Neues, haben mich jederzeit unterstützt und hatten stets Vertrauen in mich. Aufrichtigen Dank dafür!

Symbols and Abbreviations

α_f .... isotropic thermal expansion coefficients of the film [1/K]

α_s .... isotropic thermal expansion coefficients of the substrate [1/K]

a .... constant

b .... burgers vector [m]

b_f .... fraction of the grains which are favourably oriented in the as-deposited structure [/]

c .... final texture fraction [/]

C_{ijkl} .... stiffness tensor [Pa]

C_{ij} .... stiffness matrix [Pa]

ΔF_g .... stagnation force [J/m^3]

ΔU_ε .... driving force for strain energy minimization (uniaxial) [J/m^3]

ΔW_{dis} .... driving forces for dislocation density minimization [J/m^3]

ΔW_s .... surface/interface minimizing driving force [J/m^3]

ΔW_ε .... driving force for strain energy minimization (biaxial) [J/m^3]

$\Delta\gamma_i$ .... difference in the energies film-substrate interfaces for different grain orientations [J/m^2]

$\Delta\gamma_s$ .... difference in the energies of the surfaces for different grain orientations [J/m^2]

d .... grain diameter [m]

d_{hkl} .... mean grain sizes of (hkl) oriented grains [m]

d_{total} .... mean grain sizes of the entire amount of detected grain [m]

ε_{kl} .... strain tensor
ε_j .... strain matrix
ε .... biaxial thermal strain [/]
ε_u .... strain parallel to the applied stress [/]
E_a .... activation energy [eV/atom]
EBSD .... electron backscatter diffraction
E_{hkl} .... orientation-dependent Young's modulus [Pa]
γ_{gb} .... specific grain boundary energy [J/m^2]
γ_i .... energy of the interface [J/m^2]
γ_s .... energy of the free surface [J/m^2]
$\bar{\gamma}_S$ .... average surface energy [J/m^2]
$\bar{\gamma}_{gb}$ .... average grain-boundary energy [J/m^2]
G .... shear modulus [Pa]
h .... film thickness [m]
HWHM .... half width at half maximum [°]
κ .... curvature [1/m]
k .... Boltzmann constant
M .... grain boundary mobility [m^4/Js]
M_0 .... preexponential factor of mobility [m^4/Js]
M_{hkl} .... orientation-dependent biaxial modulus [Pa]
n .... Avrami exponent [/]
φ .... rotation angle around the specimen surface normal [°]
ψ .... inclination of the diffraction vector with respect to the specimen surface normal [°]
p .... driving force [J/m^3 = N/m^2]
ρ .... area density of dislocations [m/m^3 = 1/m^2]
r .... grain size, grain radius [m]
$\bar{r}$ .... mean grain size [m]
σ_{ij} .... stress tensor [Pa]
σ_i .... stress matrix [Pa]
$\sigma_{y,hkl}$ .... yield strength of the orientation (hkl) [Pa]

SEM ……………………………… scanning electron microscope

T ………………………………… temperature [K]

T_a ………………………………… annealing temperature [K]

TEM …………………………….. transmission electron microscopy

T_{dep} ……………………………… deposition temperature [K]

t ………………………………… time [s]

v ………………………………… grain growth velocity [m/s]

v_{mean} ……………………………… initial grain growth velocities for the mean grain size [m/s]

W_ε ………………………………… strain energy density [J/m^3]

$X(t)$ …………………………………volume fraction of abnormal grains,

XRD ……………………………… X-ray diffraction

Index

Danksagung 7

Symbols and Abbreviations 9

Index 13

Chapter 1 Introduction 15

Chapter 2 Theory and Literature Review 19

2.1 Grain Growth 20
2.1.1 Normal Grain Growth 21
2.1.2 Abnormal Grain Growth 22
2.1.3 Driving force: Surface/interface energy minimization 23
2.1.4 Driving force: Strain energy minimization 24
2.1.5 Stagnation force 27
2.2 Texture evolution 28
2.3 Texture and Grain Growth in Copper Thin Films 31
2.3.1 Texture and grain growth in sputtered Cu thin films 31
2.3.1.1 As-deposited state 31
2.3.1.2 Texture after annealing 37
2.3.2 Texture and grain growth in electroplated films 43
2.3.2.1 As-deposited state 43
2.3.2.2 Texture after annealing 45
Grain growth velocities and driving forces 50
2.3.4 Activation energy 53
2.3.5 Summary of the state of the literature and aim of the study 55

Chapter 3 EBSD 59

Chapter 4 Effect of Film Thickness on Texture 65

4.1 Introduction 65
4.2 Experimental 66
4.3 Results 70
4.3.1 Texture analysis 70
4.3.2 Grain size distribution 74
4.4 Driving force map 76
4.5 Discussion 78
4.6 Summary 82

Chapter 5 Effect of Uniaxial Stress on Texture Evolution 83

5.1 Introduction 83
5.2 Theoretical Predictions 84

5.2.1 Strain energy minimization – uniaxial stress 84
5.3 Experimental 87
5.3 Results 89
5.4 Discussion 92
5.5 Summary 96

Chapter 6 *In situ* Grain Growth Experiments - Effect of Temperature and Film Thickness on Grain Growth Kinetics 97

6.1 Introduction 97
6.2 In situ experiments 98
6.3 Results 98
6.3.1 As-deposited microstructure and microtexture 98
6.3.2 Texture evolution 102
6.3.3 Grain size evolution 107
6.3.4 XRD Results 109
6.4 Discussion 111
6.5 Summary 128

Chapter 7 Summary and Conclusions 129

Chapter 8 Appendix 133

8.1 Calculation of the strain energy density 133
8.1.1 Biaxial stress state 133
8.1.2 Uniaxial stress state 136

Chapter 9 Deutsche Zusammenfassung 137

Chapter 10 References 147

Chapter 1 Introduction

When John Ambrose Fleming presented the vacuum diode in 1904 probably no one could predict the various ways this idea would influence the future. His invention may be said to be the beginning of modern electronics, as it enabled electronic technology to move forward.

As a next important step, in 1947 John Bardeen, Walter Brattain and William Shockley observed that when an electrical contact was applied to a crystal of germanium the output power was larger than the input. Further work and studies resulted in the invention of the transistor. This is considered by many to be one of the greatest inventions of the twentieth century, as it is a key component in practically all modern electronics.

But further ideas and inventions were necessary on the way towards modern electronics. In 1958 Jack Kilby was working on circuit design: At this time, computers were typically built up from a series of modules, each of them containing the electronic components needed to perform a single function. A complex circuit

required several modules working together, therefore different modules were assembled and soldered by hand. As a result, they suffered major reliability problems and the computer engineers were unable to increase the performance of their designs due to the huge number of components involved. Assuming that germanium could be used to make all common electronic components – transistors, capacitors, resistors, etc. – Jack Kilby set about manufacturing the circuit components in mass in a single piece of semiconductor material. The integrated circuit was born. Beside the improved reliability, the two main advantages of integrated circuits are low cost and higher performance. Cost is low because the chips with all their components are printed as a unit by photolithography and the performance is high because the components switch quickly and consume little power.

While the first integrated circuits contained only a few transistors, their number and density was continuously increased – up to billion-transistor processors in 2008 (an example of which is Intels Montecito Itanium chip).

Nowadays, integrated circuits are used in almost all electronic equipment – computing, communication, manufacturing and transportation systems all depend on them and represent indispensable parts of modern society. The fabrication of the integrated circuits is a layer process based on photolithography. Usually, a single-crystal silicon wafer is used as a substrate and photolithography is used to define different areas of the substrate to be doped or to carry insulators or metal conduction lines. Typically, thin copper or aluminium lines or films are used for interconnection. And while miniaturization of the feature size leads to a decrease in cost and an increase in functionality, it also requires improved manufacturing techniques and an advanced understanding of material behaviour.

The main problems for Cu interconnects are electromigration, stress voiding and fatigue. Stress voiding is caused by the strain and stress that develop due to the difference in the thermal expansion coefficient between the metal and the substrate, while electromigration results from the high current density in the interconnect lines which causes diffusion of atoms and produces voids and hillocks. These voids or hillocks could lead to increased resistance in the Cu lines and eventually cause an open or closed circuit. Both have functional dependence on grain orientation [Mönig 2005, Koike *et al.* 2002, Sekiguchi *et al.* 2003, Schwaiger and Kraft 2003]. Consequently, the texture has influence on the main challenges associated with interconnects. Texture formation in Cu thin films is complex and depends on many

different factors, such as film thickness, substrate material, stress state, deposition method and annealing temperature. Its dependence on film thickness, heat treatment and time is investigated in this work.

In the last decade, the electron backscatter diffraction (EBSD) method became a widely used technique for the determination of microtexture, as the automated collection rate has steeply increased. The systematic use of EBSD measurements provides, apart from texture information with spatial resolution, access to neighbour relationships and grain size distributions. Furthermore, a combination of the EBSD-system and heating and/or tensile tests, gives insight in the basic mechanisms responsible for grain growth and texture evolution.

First, in chapter 2 theoretical aspects are reviewed. The different driving forces responsible for grain growth as well as a texture evolution model are presented. Chapter 2 also contains a literature review summarizing the current understanding of texture formation in Cu thin films. Finally, this chapter also outlines the motivation of this study.

In chapter 3, the basics and advantages of the EBSD technique are presented. In chapter 4, the microtextures of 0.5-10 µm thick Cu films annealed at 330°C are characterized. The transition from a dominant (111) to a (100) fibre texture with increasing film thickness is clearly evident. For interpretation of the texture evolution, a driving force map is constructed. The observations follow the predictions of the texture evolution model of Thompson and Carel [Thompson and Carel 1995, Thompson and Carel 1996a] but add new elements. Furthermore in this chapter a detailed comparison of EBSD results with results based on X-ray diffraction (XRD) is made. The results of this study by Sonnweber-Ribic, Gruber, Dehm and Arzt have been published [Sonnweber-Ribic *et al.* 2006b].

Up to this point strain was introduced through a change in temperature into the film – therefore it was impossible to vary temperature and strain independently. In the next chapter, this restriction is eluded by carrying out uniaxial tensile tests.

Theoretical calculations comparing the driving forces for a 3 µm thick Cu films in case of a uniaxial stress state are presented. Parts of the theoretical estimates by Sonnweber-Ribic, Dehm, Gruber and Arzt have been published [Sonnweber-Ribic *et al.* 2006a]. They revealed a dominant strain energy minimization above a specific strain. In contrast to these theoretical predictions, several tensile tests above this limit revealed no (100) grain growth. These observations provide again an indication that

pure energetic considerations are not sufficient. In order to get additional insight into grain growth, *in situ* tests have to be carried out.

Chapter 6 includes a detailed analysis of abnormal growth of individual (100) oriented grains for more than 24 hours at temperatures between 90 and 118°C. The EBSD data are then used to interpret the dynamics and kinetics of grain growth processes, leading to conclusions that would be unreachable without *in situ* capacity. Thus, analysis of grain growth velocities for different film thicknesses and annealing temperatures allows to get additional insight into the basic mechanisms of abnormal grain growth. This result provides a powerful tool to control texture evolution in Cu thin films through a change in fabrication.

Chapter 2 Theory and Literature Review

Thin films usually show strong fiber textures which develop during deposition and annealing. This texture – the dominant grain orientation - has great influence on the mechanical response of materials and consequently on the performance and reliability of components. Thus, the understanding and control of texture evolution provides at the same time a powerful tool for adjusting elastic and plastic properties.

Grain growth in preferred directions causing texture evolution in thin films is driven by energy minimization. Anisotropic energies such as surface, interface and strain energy result in an orientation-dependent driving force on the grain boundaries determining the resulting texture.

2.1 Grain Growth

Grain growth refers to the process by which the average grain size increases and the total grain boundary area decreases. It is one of the most important processes used to control microstructure and grain orientations in thin films. The driving force p for grain boundary migration has the dimension of energy per unit volume, which is equivalent to a force acting per unit area on a grain boundary. The resulting velocity v of a grain boundary is given by [Humphreys and Hatherly 1995]

$$v = \frac{dr}{dt} = M \cdot p \, , \tag{1.1}$$

where M is the boundary mobility, r the radius of curvature of the grain boundary and t is the time. This equation is based on the following assumption: Supposing that a chemical potential difference p exists between the atoms of two neighboring grains A and B, and that there is an energy barrier E_a for an atom to make the transition across the grain boundary, the total net transport and therefore the grain boundary velocity v, can be determined as follows.

The probability for an atom to move from A to B is proportional to exp($-E_a /kT$) while the probability to move from B to A will be proportional to exp($-(E_a+p)/kT$). Consequently, the net transport will be proportional to

$$v \propto \exp\left(-E_a / kT\right) \cdot \left[1 - \exp\left(-p / kT\right)\right] \tag{1.2}$$

Assuming that $p \ll kT$, it can be approximated by

$$v = \left(M_0 \exp(-E_a / kT)\right) \cdot p = M \cdot p \tag{1.3}$$

The driving force p is based on various sources – the most relevant ones for thin films are discussed in the following.

2.1.1 Normal Grain Growth

In the case of normal grain growth, the driving force is the reduction of the total grain boundary energy through the reduction of the total grain boundary area, which is not orientation-sensitive. Therefore the average grain size increases uniformly without any change in texture (Fig.2.1). Consequently, the grain size distribution is relatively narrow which makes the grain structure look uniform. The grain size distribution appears to be well fitted by a log-normal distribution with a maximum grain size being 3-5 times the average [Novikov 1997, p 116]. The curved grain boundary migrates in the direction of the centre of curvature.

An analytical model of normal grain growth was derived in the statistical theory of Hillert [Hillert 1965]. His approach starts from the assumption that the grain boundary velocity v is proportional to the local driving force p, which is proportional to the local curvature κ:

$$v = \frac{dr}{dt} = M \cdot p = M \cdot \gamma_{gb} \cdot \kappa \tag{1.4}$$

where γ_{gb} is the specific grain boundary energy. Due to different surroundings, grains of the same size r may not have the same value of average curvature but it is assumed that there is an average over all the grains of size r which will yield the average growth rate of those grains [Hillert 1996],

$$\frac{dr}{dt} = M\gamma_{gb} A \cdot \left(\frac{1}{\bar{r}} - \frac{1}{r} \right) \tag{1.5}$$

where A is a constant which is approximately one [Thompson and Carel 1996a] and $\bar{r}$ is the mean grain size – a time dependent characteristic size of the system. That means that grains with sizes larger than the average will grow while grains with radii smaller than the average will shrink.

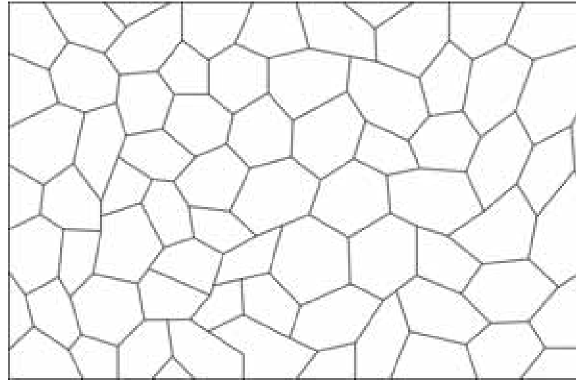

Figure 2.1: Microstructure for normal grain growth. Large grains tend to grow larger while small grains shrink and disappear – while the mean grain size increases, the grain structure is always uniform.

2.1.2 Abnormal Grain Growth

The beginning of abnormal grain growth is correlated to the sudden appearance of unusually large crystallites. This disturbs the microstructure uniformity – in other words, during abnormal grain growth, two different grain populations are observed (Fig. 2.2): the fine grained matrix and coarse grains. Therefore in the course of abnormal grain growth the grain size distribution appears bi-modal with each of the peaks representing one of the grain populations. The evolution of abnormal grain growth is described by the time or temperature dependence of the volume fraction of coarse grains. Their kinetic curve is in form similar to the kinetic curve of primary recrystallization. That is the reason why the abnormal grain growth process is often referred to as secondary recrystallization and can be described by the kinetic model of Johnson, Mehl [Johnson and Mehl 1939], Avrami [Avrami 1939] and Kolmogorov [Kolmogorov 1937], which is commonly known as JMAK model:

$$X(t) = 1 - e^{\left(-at^n\right)} \tag{1.6}$$

X(t) is the volume fraction of abnormal grains, a is a constant and n is referred to as the Avrami exponent.

To explain the appearance of abnormal grains in a fine-grained matrix an additional driving force is ascribed to them which is often grain orientation specific and therefore abnormal grain growth can lead to pronounced texture changes. The

driving forces can arise from different sources – the two most important ones for thin films are described in the following sections.

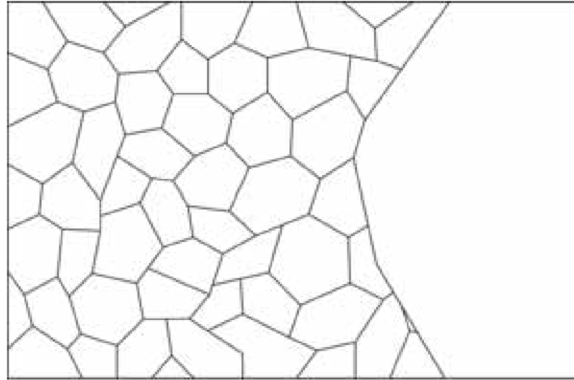

Figure 2.2: Microstructure during abnormal grain growth. A favoured, abnormal grain consumes the matrix grains.

2.1.3 Driving force: Surface/interface energy minimization

Thin films on substrates possess a free surface and an interface to the substrate. Both the energy γ_s of the free surface and the energy γ_i of the interface depend strongly on the orientation of the grain. For fcc metals on an amorphous substrate it is expected that the surface and the interface energy are minimized for grains with (111) plane parallel to the surface/interface, as this is the most densely packed lattice plane.

In this case the additional driving force can be defined as the change in energy ΔW_s caused by the reduction in the average surface energy γ_s and interface energy γ_i of the film [Thompson and Carel 1996a]

$$\Delta W_s = \frac{\Delta\gamma}{h} \tag{1.7}$$

where h is the film thickness and

$$\Delta\gamma = \Delta\gamma_s + \Delta\gamma_i \, . \tag{1.8}$$

$\Delta\gamma_s$ and $\Delta\gamma_i$ are the differences in the energies of the surface and film-substrate interface for different grain orientations.

2.1.4 Driving force: Strain energy minimization

Another source of orientation-dependent diving forces in thin films is the elastic anisotropy. This anisotropy results in different biaxial moduli for different crystallographic orientations and consequently in high strain energy differences.

The strain energy W is defined as

$$W = \int_V \sigma_{ij} d\varepsilon_{ij} dV \ . \tag{1.9}$$

The work W done by the applied stress can be calculated as the product of the stress tensor σ_{ij} and strain tensor ε_{ij}. The strain energy W per unit volume V is referred to as strain energy density W_ε

$$dW_\varepsilon = \sigma_{ij} d\varepsilon_{ij} \ . \tag{1.10}$$

Using Hooke's law this integral can be solved. The strain energy density can be calculated with the help of the strain tensor ε_{ij} and ε_{kl} and the stiffness tensor C_{ijkl}

$$W_\varepsilon = \frac{1}{2} \varepsilon_{ij} C_{ijkl} \varepsilon_{kl} \ . \tag{1.11}$$

Due to the symmetry of the stress tensor, strain tensor, and stiffness tensor, only 21 elastic coefficients are independent and it is useful to express this equation in matrix notation, also called Voigt notation

$$W_\varepsilon = \frac{1}{2}\varepsilon_i C_{ij} \varepsilon_j \, . \tag{1.12}$$

where C_{ii} is the stiffness matrix and ε_i is the strain vector (see section 8.1 in the Appendix).

The driving force for strain energy minimization is the difference between the strain energy density of the initial grain ($W_{\varepsilon,0}$) and the grown grain (W_ε).

$$p = W_\varepsilon - W_{\varepsilon,0} = \Delta W_\varepsilon \, . \tag{1.13}$$

As a thin film and its substrate generally have different thermal expansion coefficients, the different thermal expansion during heating and cooling can lead to a biaxial strain in the film. This biaxial thermal strain ε_{th} in a film on a constraining substrate is given by

$$\varepsilon_{th} = \int_{T_{dep}}^{T_a} \left(\alpha_s - \alpha_f\right) dT \approx \Delta T\left(\alpha_s - \alpha_f\right) = \left(T_a - T_{dep}\right)\left(\alpha_s - \alpha_f\right) \tag{1.14}$$

where α_s and α_f are the isotropic thermal expansion coefficients of the substrate and the film and T_a and T_{dep} are the annealing and deposition temperature. This biaxial thermal strain results in an orientation-dependent thermal stress and therefore in a texture-dependent strain energy density, as the elastic properties depend on the grain orientation. If the strain is accommodated elastically, the strain energy density W_ε can be calculated as

$$W_\varepsilon = M_{hkl} \cdot \varepsilon^2 \tag{1.15}$$

where M_{hkl} is the orientation-dependent biaxial modulus which can be derived from the stiffness tensor of the material (Appendix 8.1.1). Calculating the biaxial moduli for different grain orientations, Zhang et al. [Zhang *et al.* 2002b] found that the four lowest strain energy densities corresponded to grains with (100), (511), (310) and (311) planes oriented parallel to the film plane.

When the yield strength of an orientation is reached, the strain energy density is assumed to saturate at

$$W_{\varepsilon} = \frac{\sigma^{2}_{y,hkl}}{M_{hkl}}, \tag{1.16}$$

where $\sigma_{y,hkl}$ is the yield strength of the specific orientation (hkl).

Using equations (1.13) and (1.15), the difference in strain energy density between two neighbouring grains with orientation (111) and (100) is

$$\Delta W_{\varepsilon} = (M_{111} - M_{100})\varepsilon^{2} \quad \text{(all elastic case)}, \tag{1.17}$$

if both orientations deform elastically.

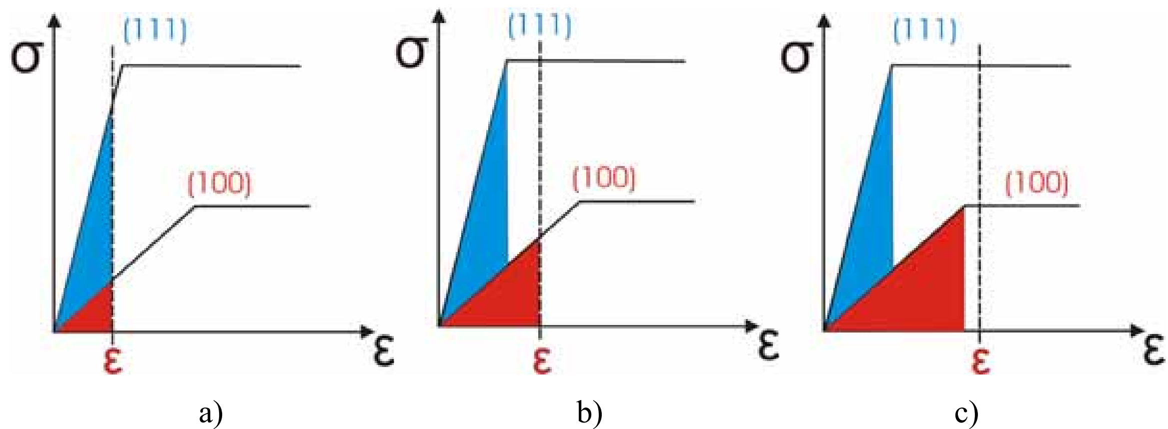

Figure 2.3: Schematic diagram of strain energy densities of (111) and (100) grain orientations. Coloured areas correspond to the stored elastic energy in each case. a) The strain is accommodated elastically in both orientations. b) While the (111) orientation has reached its maximum value, the (100) grains still deform elastically. c) Both orientations have reached their upper limit and yield.

This corresponds to the driving force available for grain-boundary motion. The driving force increases parabolically with strain (temperature) until the (111) orientation starts to yield. For this case the strain energy density of the (111) grains is constant, but the strain energy density of the (100) orientation can still increase (Fig. 2.3b). As a consequence the total driving force is then

$$\Delta W_{\varepsilon} = \frac{\sigma_{y,111}^{2}}{M_{111}} - M_{100}\varepsilon^{2} \quad \text{(111 plastic).} \tag{1.18}$$

This behaviour continues until the (100) oriented grains start to yield, too. Then the strain energy difference becomes (Fig. 2.3c):

$$\Delta W_{\varepsilon} = \frac{\sigma_{y,111}^{2}}{M_{111}} - \frac{\sigma_{y,100}^{2}}{M_{100}} \quad \text{(fully plastic).} \tag{1.19}$$

Equation (1.19) demonstrates that a further increase in strain does not result in an increased difference in strain energy density.

2.1.5 Stagnation force

Beside these driving forces for grain-boundary motion, there exists a stagnation force exerted by grain boundary grooving. Mullins [Mullins 1958] has calculated this stagnation force as

$$\Delta F_{g} = \frac{\bar{\gamma}_{gb}^{2}}{h \cdot \bar{\gamma}_{S}} \tag{1.20}$$

where $\bar{\gamma}_{S}$ and $\bar{\gamma}_{gb}$ are the average surface and grain boundary energies, respectively. Following Inman and Tipler [Inman and Tipler 1963] an approximate relationship between the surface and grain-boundary energy is given by $\bar{\gamma}_{gb} \approx 0.34 \cdot \bar{\gamma}_{S}$ for Cu. Consequently, eq. (1.20) can be written as

$$\Delta F_{g} \approx \frac{\bar{\gamma}_{S}}{9 \cdot h} \tag{1.21}$$

Assuming the average surface energy to be 2025 mJ/m² (arithmetic mean of the surface energies of (111) and (100) oriented grains [Skiver and Rosengaard 1992], the stagnation force can be estimated as a function of film thickness.

2.2 Texture evolution

Texture development in metallic fcc films usually occurs through grain growth and is controlled by the minimization of its total energy which consists of surface, interface and elastic strain energy. In the following section, the factors which control the texture selection are summarized.

Thompson and Carel [Thompson and Carel 1996a] express the rate of growth of an individual grain as

$$\frac{dr}{dt} = M\left[\bar{\gamma}_{gb}\left(\frac{1}{\bar{r}} - \frac{1}{r}\right) + \Delta W_s + \Delta W_\varepsilon\right] \qquad (1.22)$$

The first term results from the reduction of energy by elimination of grain boundaries assumed to be isotropic (normal grain growth). The other two terms are highly anisotropic and can therefore influence the orientation of the growing grain (abnormal grain growth).

As ΔW_ε and ΔW_s prefer different orientations, the favoured texture depends on whether ΔW_s or ΔW_ε dominates [Thompson and Carel 1996a]. The (100) strain energy minimizing texture dominates when $\Delta W_\varepsilon > \Delta W_s$ and the (111) surface and interface energy minimizing texture otherwise. By comparing the driving forces ΔW_s and ΔW_ε , it is possible to construct a “texture map” as illustrated in Fig. 2.4. There, the texture transition from (111) to (100) can be defined as a function of film thickness h and deposition temperature T_{dep} (which is related to the strain by eq. (1.14)). For the deposition temperature of -100°C, the (111) texture is favoured below the transition thickness h_t and (100), above.

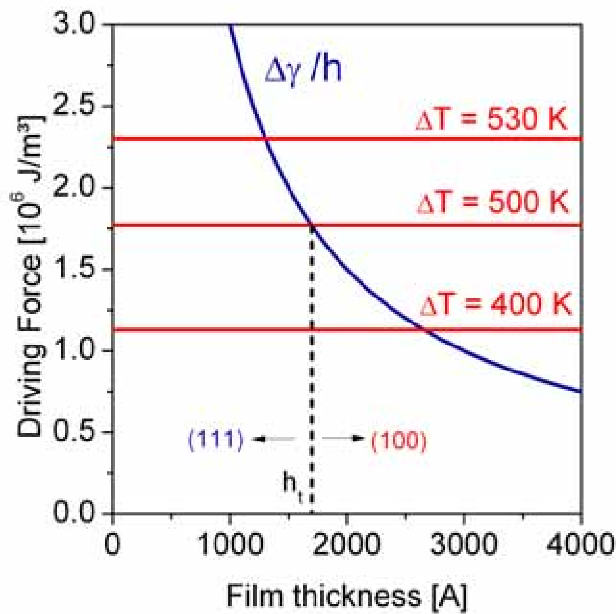

Figure 2.4: The driving force for surface/interface energy minimization $\Delta W_s=\Delta\gamma/h$, and the driving force for strain energy minimization ΔW_ε (horizontal lines) for Ag (111) and (100) textured grains as a function of the film thickness h and temperature difference ΔT. For a temperature difference of 500 K, below the transition thickness h_t the (111) texture is favoured as surface/interface energy minimization is dominant, and above h_t a (100) texture is favoured due to strain energy minimization. [Thompson and Carel 1995]

When defining this critical film thickness h_t for varying deposition temperatures, a plot of h_t vs. ΔT can be created (Fig. 2.5).

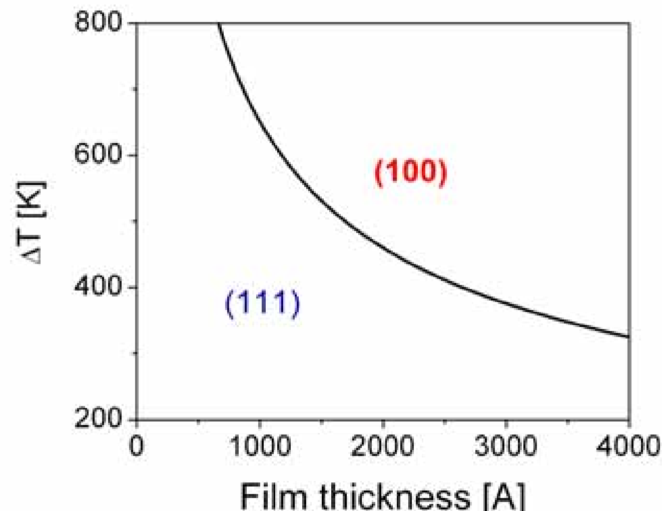

Figure 2.5: The texture transition thickness h_t versus the temperature difference ΔT. Films with h and ΔT below the blue line should develop a (111) texture and those above are assumed to prefer a (111) texture. The curve shown has been calculated for polycrystalline Ag on single crystal Ni on MgO [Thompson and Carel 1995].

Strain energy minimizing textures are favoured when films are deposited at temperatures well below the annealing temperature and in thicker films, while surface

and interface energy minimizing textures are favoured at low strains and thinner films.

Up to now, it was assumed that all the thermal strain is elastically accommodated (Fig. 2.4). And as polycrystalline thin films often have very high yield stresses, this assumption is valid to high stresses. But when the grain size is increased, the yield stress of individual grains will decrease so that their advantage will diminish and eventually disappear, therefore changing the shape of ΔW_ε (eq. (1.18) and (1.19)) and the texture map (Fig. 2.6). Again, at low film thicknesses h, the (111) surface and interface minimizing texture dominates. Between h_{t1} and h_{t2} a (100) "window" exists and above h_{t2} again the (111) orientation is energetically favoured.

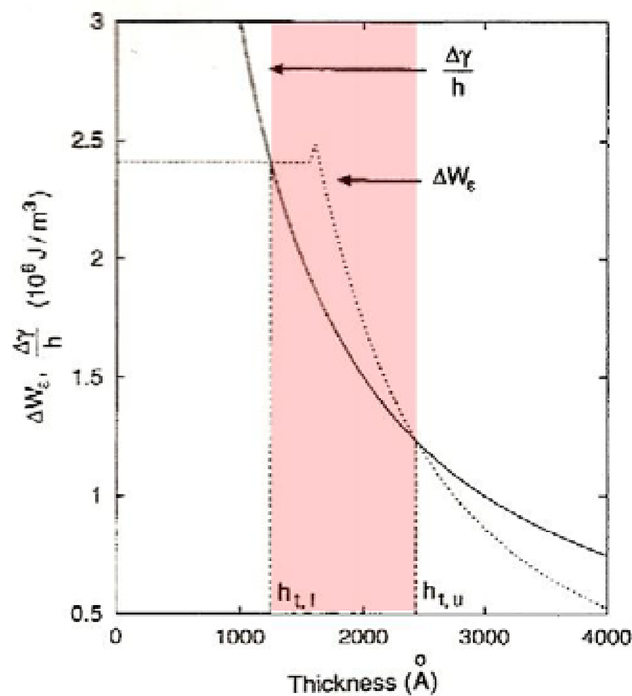

Figure 2.6: Analogous calculation as illustrated in Fig. 2.4 but showing the effect of yielding on ΔW_ε. The driving force for strain energy minimization exceeds the driving force for surface energy minimization in between h_{t1} and h_{t2}. As a consequence, there is now a thickness "window" (marked in red) over which the (100) texture is preferred [Thompson and Carel 1995].

2.3 *Texture and Grain Growth in Copper Thin Films*

In the last years, a large number of investigations have focused on textures and grain growth in Cu thin films. Not all of them showed the same results. The following chapter summarizes the literature results and tries to identify general trends, starting with the texture in sputtered Cu films, followed by electrodeposited films. Three types of textures are commonly reported in thin films:

1) the fiber texture, for which one crystallographic plane is parallel to the substrates surface, while the in-plane orientations of grains are random
2) the random texture, where grains have no preferred orientation
3) epitaxy, when the deposited film grows with one or several well-defined orienation relationships on the substrate

2.3.1 Texture and grain growth in sputtered Cu thin films

2.3.1.1 As-deposited state

Texture evolution during film deposition is sensitive to many parameters so that different results were observed by various authors for the as-deposited state. Most authors identified three main fiber components: (111), (100) and a random component [Tracy and Knorr 1993, Knorr and Tracy 1995, Kuschke *et al.* 1998, Zielinski *et al.* 1995a, Tracy *et al.* 1994] with varying distributions (Tab. 2.1).

While some found just a dominating (111) fiber texture [Dahlgren 1974, Lee and Park 2007, Park *et al.* 2005, Koike *et al.* 2002, Vinci *et al.* 1995b, Weihnacht and Brückner 2002, Okolo *et al.* 2005], other studies reported an additional texture component : Schell et al. [Schell *et al.* 2005] and Zhang et al. [Zhang *et al.* 2002a] found an extra (100) component, while Vanstreels et al. [Vanstreels *et al.* 2008] observed a weak (113) texture fraction and Flinn [Flinn 1991] found an additional (110) component. Finally, twinning of the (111) and (100) component creates additional texture components such as (511) and (221).

In the review of Knorr and Tracy in 1995, comparing the results of several studies and analysing the three texture fractions, the random fraction was found to

vary between a few percent to 75% and in most cases the (111)+(511) fractions were higher than the (100) fraction.

Tabel 2.1: Results of microstructural analysis of sputtered, as-deposited copper films. X marks the dominant texture component and x the observed minor components. The film thickness h as well as the barrier layer are listed. If known, the barrier layers orientation is added in brackets.

Literature	h [µm]	Barrier layer	(111)	(100)	random	others
Tracy and Knorr 1993	0.54	SiO_2	x	x	X	
	0.5	SiO_2	X	x	x	
	0.5	Ta	X	x	x	
	0.5	TaN	x	x	X	
Kuschke et al. 1998	0.3 - 1	Si_3N_4	X	x	x	
	0.6 - 1	Ta	X	x	x	
	0.6	TiN (111)	X	x	x	
	0.6	W (random)	x	x	X	
Tracy et al. 1994	0.5	SiO_2	X	x	x	
	0.5	Ti (0002)	X	x	x	(511)
	0.5	TiN (random)	x	X	x	
	0.5	Ti/TiN (111)	X	x	x	(511)
Lee and Park 2007	0.1	Ta	X			(511) (522) (211) (110)
	0.48		X			
	0.85		X			
Park et al. 2005	0.1	Ta	X			(511) (522) (211) (110)
	0.48		X			
	0.85		X			
Okolo et al. 2004	0.5	SiO_2 (amorphous)	X			(511) (5 7 13)
		Si_3N_4 (amorphous)	X			
Zielinski et al. 1995a	1.2	W (110)	X	x	x	
		C (amorphous)	X	x	x	
		Ta (100)	X	x	x	(511) (5 7 13)
Flinn 1991	1	SiO_2	X			(110)
Koike et al. 2002	0.05-0.9	Ta	X			
Vinci et al. 1995	0.2 – 1.2	Ta (unheated)			X	
		Ta (heated)	X			
Zhang e al. 2002	/	Si	X	x		(110)
Vanstreels et al. 2008	0.5	TaN/Ta	X			(113)
Weihnacht and Brückner 2002	0.54	SiO_2	X			
Schell et al. 2005	0.1 – 0.13	SiO_2	X	X		
Dahlgren 1974	100 - 1000	Cu	X			

Barrier layer

One reason for the large scatter in texture fractions can be identified when taking into account the underlying barrier layer, subsequently called interlayer. These interlayers have significant influence on the texture, especially at reduced atomic mobility conditions (high gas pressure or low substrate bias voltage). Fig. 2.7 summarizes the results for as-deposited (111) volume fractions determined in several studies. If possible, an orientation relationship between the film and substrate is built

up [Dehm *et al.* 2003, Ohmi *et al.* 1991, Kwon *et al.* 1997]. Dehm et al. [Dehm *et al.* 2003] found an epitaxial Cu ($\{111\}\pm\langle 11\overline{2}\rangle Cu \| (0001)\langle 10\overline{1}0\rangle \alpha - Al_2O_3$) microstructure with varying intensity of sputter cleaning of (0001)-oriented α-Al_2O_3 substrates and Kwon et al. [Kwon *et al.* 1997] studied epitaxial growth of (111) oriented Cu grains on (100) oriented Ta interlayer. The same observation was made by Zielinski et al. [Zielinski *et al.* 1995a]. The authors found the (111) texture on a Ta layer (100-textured) to be much stronger than on W (110-oriented) or C (amorphous). Again, textural inheritance is assumed to explain the stronger texture, due to a small mismatch in lattice spacing.

But even if epitaxy between the grains of the interlayer and the film is not possible, the interlayers have significant influence on the film microstructure. On amorphous or weakly textured interlayers, commonly (111), (200) and random texture fractions were observed in Cu thin films [Zielinski *et al.* 1995a, Jakkaraju and Greer 2002, Tracy *et al.* 1994]. Tracy et al. [Tracy *et al.* 1994] found a 500 nm thick Cu film on SiO_2 to have the typical three-component texture and twinning of the (111) and (200) component created two more texture components. Detailed analysis showed a rather broad (111) peak. Jakkaraju and Greer [Jakkaraju and Greer 2002] found a much weaker texture on the amorphous SiN_x interlayer than on Ta or TaN. Nevertheless, comparison of these results to other studies is difficult, as extensive grain growth has already taken place during deposition.

On the other hand, a highly textured interlayer often leads to an increased (111) fraction – making the (100) and/or random fraction decrease substantially or disappear. Kuschke et al. [Kuschke *et al.* 1998] revealed a preferred (111) texture for the fiber textured barrier layers in the as-deposited state. The same results were observed by Tracy et al. [Tracy *et al.* 1994]. The introduction of a textured interlayer such as Ti (0002) or Ti(0002)/TiN(111) strengthened the texture by increasing the fraction of (111) oriented grains. The authors proposed preferred nucleation of (111) oriented Cu islands due to interfacial energy minimization to be responsible for the texture strengthening on highly textured interlayers.

A randomly oriented interlayer resulted in steep decrease in (111) texture fraction (Fig. 2.7), while the random component increased substantially. Kuschke et al. [Kuschke *et al.* 1998] found a randomly oriented W layer to cause a nearly completely random grain orientation distribution and Tracy and Knorr [Tracy and Knorr 1993] identified for films sputtered on TaN a random component almost twice

as large as for the films sputtered on SiO_2. Unfortunately, no texture information of these interlayers is given in this study.

Vinci et al. [Vinci *et al.* 1995b] prepared two sets of Cu samples with film thicknesses between 0.2 and 1.2 µm. They were found to be either randomly oriented or with a strong (111) fiber texture when deposited at 250 °C on unheated or heated Ta barrier layers, respectively. No information about the interlayers texture is given but it is probable that a random texture of the unheated Ta layer is again the reason for the change in texture.

Tracy et al. [Tracy *et al.* 1994] observed that a nearly random TiN interlayer results in very weak texture.

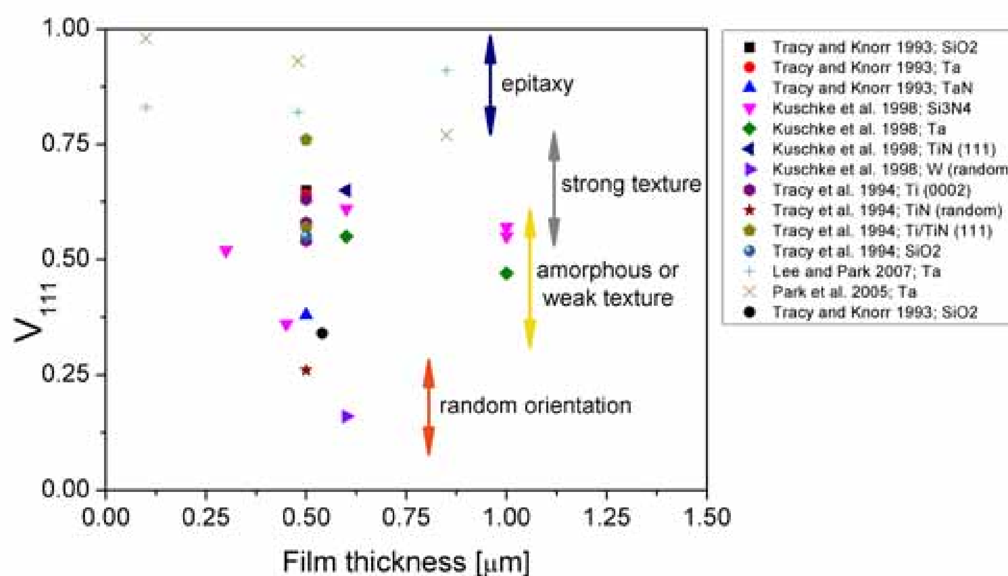

Figure 2.7: Summary of texture results for as-deposited Cu films of several studies. The volume fraction V_{111} is plotted as a function of film thickness. The interlayer material and its texture (if known) are shown in the legend. The influence of the barrier layer on (111) texture component is summarized by the arrows: while a randomly oriented interlayer results in a nearly random orientation (with a reduced amount of (111) fraction), amorphous or weak textured barrier layers result in an increase of (111) texture fraction. Further increase is induced by a strong underlying texture and a nearly complete (111) texture is found for epitaxial growth on Ta-interlayers.

Film thickness

Conflicting results have been published when investigating the influence of the film thickness on the as-deposited texture. While some authors [Kuschke *et al.* 1998, Lee and Park 2007, Vinci *et al.* 1995b] found no connection to the texture regarding film thicknesses from 0.1 to 1.2 µm. Park et al. [Park *et al.* 2005] found a decreasing

(111) fraction correlated to an increase in twin related orientations with increasing film thickness (0.1-0.85 µm) (Fig. 2.7). As the area indexed by EBSD was in the range of only 30% for the 0.1 and 0.48 µm thick films, a detailed comparison is difficult.

Jakkaraju and Greer [Jakkaraju and Greer 2002] investigated the texture and microsturcture of 120 to 1500 nm thick Cu films deposited under different conditions. An increase in (111) texture was found for an increased film thickness attributed to a higher substrate temperature due to an increased sputter time. The same trend was observed by Chan et al. [Chan *et al.* 2006] for 130 to 1050 nm thick films, who found the thicker films to exhibit enhanced crystalline nature than thinner films with a preferred (111) orientation.

The reason for the conflicting results may lie in the different deposition parameters which have significant influence on texture formation as outlined below.

Deposition parameters

Key parameters for texture and microstructure development during deposition are the deposition parameters such as substrate temperature [Flinn 1991], gas pressure [Jakkaraju and Greer 2002], the target-substrate distance or the substrate bias voltage (influencing the energy of the arriving atoms [Somekh 1984a, Somekh 1984b]) and the energy and flux density of the Ar ion bombardment [Ohmi *et al.* 1991, Nitta *et al.* 1992].

Ohmi et al. [Ohmi *et al.* 1991] found that the as-deposited texture of a Cu film could be influenced by the ion bombardment energy, which was controlled by changing the substrate bias voltage. When the incoming ions interact with the atoms in the surface layer, the ions lose most of their energy, thus activating the film surface. At relatively low ion bombardment energies, Cu films grew either epitaxially depending on the substrate orientation: (111) oriented films on (111) Si and (100) oriented films on (100) Si or a mixture of (111) and (100) texture was observed for Cu films on amorphous SiO_2. On the other hand, at relatively high bombardment energies (111) oriented films were grown regardless of the substrate orientation. The authors assume that this was due to the ion bombardment that aligned the most closely packed surface normal to the direction of ion bombardment. Another possible

explanation is that the increased mobility of the atoms allowed the system to build up the surface energy minimizing (111) texture.

The same observation was made by Jakkaraju and Greer [Jakkaraju and Greer 2002]. A higher deposition rate and a decreased Ar gas pressure, giving more bombardment during deposition, increased the (111) texture.

And Flinn [Flinn 1991] found the sharpness of the (111) peak to be increased when the deposition power is increased – and presumably the effective deposition temperature.

Furthermore Zielinski et al. [Zielinski *et al.* 1995a] found the Cu films to be sensitive to the chamber base pressure: in the HV chamber, the (111) texture was observed to weaken with increasing deposition temperature but the opposite trend was found in a UHV chamber with less contamination.

Theoretical models for texture formation during sputter deposition

Several theoretical models have been developed to explain texture formation during sputter deposition. The tendency to minimize the surface energy is widely accepted as the dominant driving force in thin films if the surface mobility of the atoms is sufficiently high [Thompson and Carel 1995, Knuyt *et al.* 1995, Lee 2002]. Knuyt et al. [Knuyt *et al.* 1995] proposed a model which is based on the assumption that atoms of grains with a higher surface energy situated at the boundary have a tendency to jump towards the grain with the lower surface energy. Therefore, an evolution from a random texture towards the texture with the smallest possible surface energy is predicted with increasing film thickness. Also, Lee [Lee 1989, Lee 1999b] proposed in his model that the texture of a film is controlled by the surface energy and the concentration of its atoms close to the film. For a low evaporation rate, grains with a minimum surface energy being parallel to the substrate are favoured, i.e. a (111) texture for Cu thin films. But changing deposition parameters led to other orientations – as observed experimentally. Nevertheless, all these models do not give a definite explanation for orientations other than (111).

2.3.1.2 Texture after annealing

Annealing of the as-deposited films resulted in different microstructural evolutions (Tab. 2.2). While some authors observed an increase in (111) texture, others found the (100) texture component to increase during annealing.

Increase in (111) texture component

Several authors found the (111) texture component to increase during annealing [Kuschke *et al.* 1998, Harper *et al.* 1994, Murakami *et al.* 2005, Moriyama *et al.* 2004, Moriyama *et al.* 2003, Takayama and Oikawa 2005, Weihnacht and Brückner 2002, Okolo *et al.* 2005, Schell *et al.* 2005,Tracy *et al.* 1994]. The driving force for this texture development is assumed to be the minimization of the surface energy. This behaviour was mostly reported for Cu thin films – the upper limit of film thickness lying between 500 nm and 1 µm [Kuschke *et al.* 1998, Harper *et al.* 1994, Weihnacht and Brückner 2002, Okolo *et al.* 2005].

Dehm et al. [Dehm *et al.* 2003] observed a strong (111) texture for even thicker films (100 nm to 2 µm) on Si-substrates which were annealed immediately after sputter deposition at 450-600°C.

But not every increase in (111) texture fraction can be attributed to surface energy minimization alone: Moriyama et al. [Moriyama *et al.* 2003] analyzed the microstructures of 100 nm thick Cu films freestanding, and on different substrates. They found an increase in the (111) peak intensity during room temperature storage for the films deposited on Si_3N_4 and rock salt, which was attributed to the growth of (111) oriented grains. On the other hand, no grain growth was observed during room temperature storage in the free standing films. This can not be explained by surface energy minimization but it is in agreement to the authors assumption that strains introduced by the substrate to the film provide energetic assistance for the grain growth.

In another study Moriyama et al. [Moriyama *et al.* 2004] observed that large grains at the bottom of the film grew towards the film surface. Thus, the authors assumed the rigid substrate, introducing strain to the film, to be the primary factor to induce grain growth.

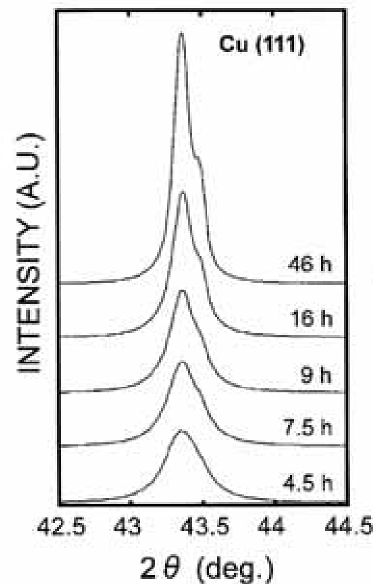

Figure 2.8: Changes of (111) XRD peak profiles of a 1 µm thick Cu film deposited by sputtering on a Si/Si_3N_4 substrate during room temperature storage. A steep increase in the (111) peak intensity was found [Moriyama *et al.* 2004].

Nevertheless it is not clear, how strain energy should be expected to prefer the growth of (111) oriented grains. Murakami et al. [Murakami *et al.* 2005] proposed a new grain growth model in which dislocation glide was assumed to be the dominant strain relaxation mechanism. Beside the elastic strain also the energy of the dislocation strain fields is assumed to contribute to the total strain energy of the thin film. As it is found that the energy of the dislocation strain field is reduced as the grain size increases, this is claimed to be the explanation for the observed grain growth. Nevertheless it is not clear why (111) oriented grains should be favoured as they are found to store a larger total strain energy than the (100) grains of the same grain size.

Takayama and Oikawa [Takayama and Oikawa 2005] investigated the influence of different sublayers (Ta and TaN) on the microstructure of Cu thin films (up to 300 nm). They found that Cu films on Ta recrystallized at temperatures lower than those on TaN. This result was again attributed to the larger internal stresses in Cu film on Ta than on TaN. After annealing, all the films exhibited a (111) texture, and an increasing grain size for an increasing film thickness.

Increase in (100) texture component

In contrast to these results, several authors observed a texture transition to a dominant (100) fiber texture during annealing (Tab. 2.2). This behaviour was found for films thicker than 300 nm. In general, this behaviour was ascribed to strain energy as the driving force. It was assumed to be caused by differential thermal expansion between the film and the substrate [Koike *et al.* 2002, Vook and Witt 1965a, Vook and Witt 1965b, Park *et al.* 2005, Park and Field 2006, Field *et al.* 2005b, Lee and Park 2007, Zhang *et al.* 2002a, Zielinski *et al.* 1995b].

Zhang et al. [Zhang *et al.* 2002a] observed increased (100) and (110) texture fractions in Cu films on a Si substrate after annealing at 300°C (Fig. 2.9). In contrast, no such texture transition was found for a free standing film, indicating strain energy minimization to be the dominant driving force for the grain growth.

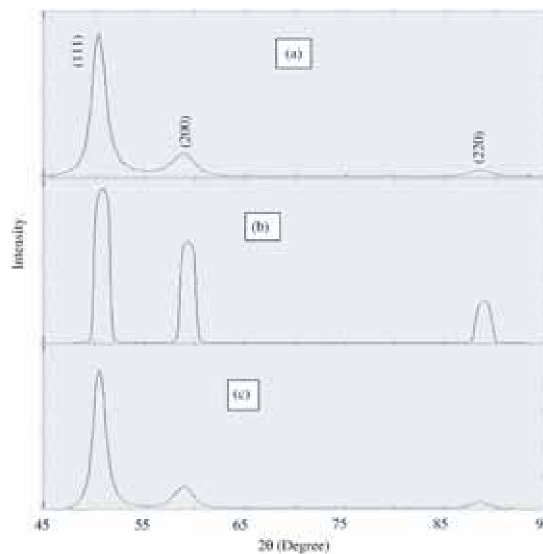

Figure 2.9: XRD line profiles of Cu thin films: (a) as-deposited; (b) attached to Si substrate and after annealing; (c) free-standing and after annealing [Zhang *et al.* 2002a].

An analogous result was found by Zielinski et al. [Zielinski *et al.* 1995b] who reported abnormal (100) grain growth for 1.2 µm thick Cu films on Si or Al substrates during annealing, while no such texture change was found for the films on Cu substrate.

Park et al. [Park *et al.* 2005, Park and Field 2006, Field *et al.* 2005b, Lee and Park 2007] found a texture change to a (100) fiber texture for the 480 nm thick film while only little changes in grain size and texture were found for the 100 nm thick

film. Interestingly, they observed a texture consisting of (100) and various other components for the 850 nm thick film after annealing which was attributed to multiple and extensive twinning.

Up to now, the strain was supposed to be induced through thermal mismatch between substrate and film when increasing the temperature. In some cases, high initial stresses were expected to act as dominant driving force.

Vanstreels et al. [Vanstreels *et al.* 2006,Vanstreels *et al.* 2008] studied the influence of film thickness and different interlayers on abnormal grain growth. Abnormal (100) grain growth was identified in a 500 nm thick Cu film on a TaN/α-Ta barrier layer. For thinner films or different sublayers (TaN, β-Ta), such abnormal grain growth was found to a much lesser extend. As the Cu film on the TaN/α-Ta barrier layer exhibited the highest initial stress, it was again assumed that strain energy minimization was the dominant driving force.

Field et al. [Field *et al.* 2003] found a strong (100) texture for the 300 nm thick film on an amorphous C layer, a (111) texture for the 300 nm thick film on Ta_3N_5 and only a weak texture for the 700 nm thick film on Ta_3N_5 (Fig. 2.10) after room temperature storage of several months. The authors attributed this observation to the fact, that the C layer was thicker and harder than the Ta_3N_5 sublayer. Therefore the Cu film on the C layer was constrained to a greater extent, resulting in a (100) texture.

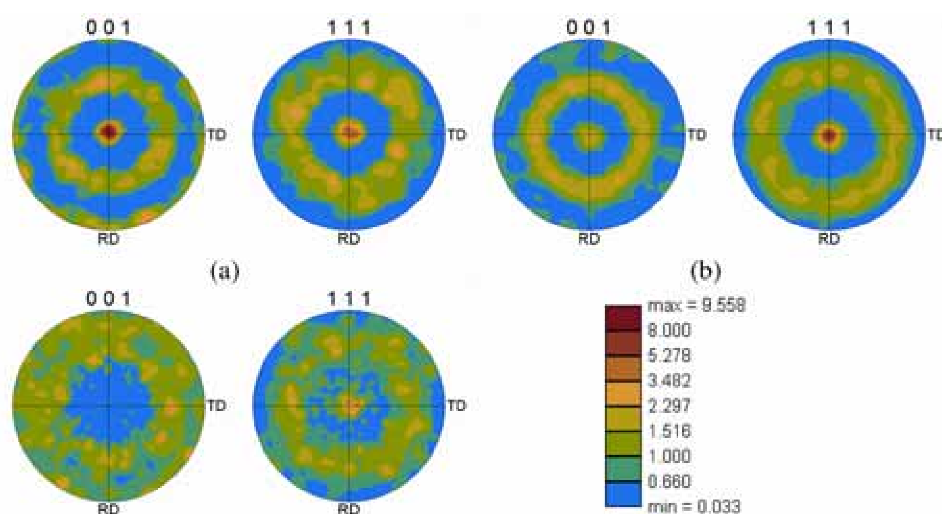

Figure 2.10: (001) and (111) pole figure of the structures of (a) the 300 nm Cu film on α-C:H, (b) the 300 nm Cu film on Ta_3N_5, and (c) the 700 nm Cu film on Ta_3N_5. The intensity colour scale is shown with units of times random. A strong (100) texture was found for the 300 nm thick film on the amorphous C layer [Field *et al.* 2003].

Tabel 2.2: Results of microstructural analysis of sputtered copper films after annealing or room temperature storage. The film thickness h, the annealing Temperature T_a, as well as the substrate and barrier layer are listed. A deposition temperature, T_{dep}, different from room temperature is mentioned.

Literature	h [µm]	Substrate/Barrier	T_a [°C]	Texture
Kuschke et al. 1998	0.3 - 1	(100)Si/SiO_2/Si_3N_4	650	(111)
		(100)Si/SiO_2/Ta		(111)
		(100)Si/SiO_2/TiN		(111)
		(100)Si/SiO_2/W		no change
Harper et al. 1994	1	Si/SiO_2	450	(111)
Dehm et al. 2003	0.1 - 2	(0001)α-Al_2O_3 (001)Si/SiO_x (001)Si/SiN_x/SiO_x	450 - 600	(111)
Murakami et al. 2005	0.1	NaCl Si/Si_3N_4	/	(111)
Moriyama et al. 2004	0.1 - 1	(100)Si/Si_3N_4	RT	(111)
Moriyama et al. 2003	0.1	NaCl Si_3N_4	RT – 400	(111)
Takayama and Oikawa 2005	0.3	(100)Si/SiO_2/Ta (100)Si/SiO_2/TaN	100 - 400	(111)
Weihnacht and Brückner 2002	0.5	(111)Si/SiO_2	150-500	(111)
Okolo et al. 2005	0.5	(510)Si/SiO_2 (100)Si/SiO_2/Si_3N_4	450 (T_{dep}=100°C)	(111)
Koike et al. 2002	0.3 -0.9	(100)Si/Ta/Cu	450	(100)
Vook and Witt 1965	0.3-0.9	glass	200 (T_{dep}=80K and RT)	(100)
Zhang et al. 2002b	/	(100)Si	300	(100)+(110)
		freestanding		(111)
Zielinski et al. 1995b	1.2	(100)Si/SiO_2/Si-N/W	300	(100)
		Al/Si-N/W		(100)
		Cu/Si-N/W		(111)+random
Park et al. 2005	0.1 0.48 0.85	(100)Si/SiO_2/Ta	150-300	(111)
			191	(100)
			200-400	(100)+twins
Vanstreels et al. 2006 and 2008	0.1 - 0.5	(100)Si/Si_3N_4/SiO_2/TaN/α-Ta	RT - 400	(100)
		(100)Si/Si_3N_4/SiO_2/TaN		
		(100)Si/Si_3N_4/SiO_2/TaN/β-Ta		
Field et al. 2003	0.3	(111)Si/SiO_2/α-C:H	RT - 550	(100)
	0.3	(111)Si/SiO_2/Ta_3N_5		(111)
	0.7	(111)Si/SiO_2/Ta_3N_5		weak texture
Dahlgren 1974	100 - 1000	Cu Al	T_{dep}= -196	(100)
			T_{dep}= 6	(100)
			T_{dep}= 13	(100)
			T_{dep}= 100	no change
Patten 1971	1000	Cu	RT	(100)
Nitta et al. 1992	1 – 1.5	(100)Si/SiO2	450	(100)

Analogous results were found by Dahlgren [Dahlgren 1974] for 100 µm to 1 mm thick Cu films. They found a texture transition from a (111) texture to a dominant (100) texture during room temperature storage for the films prepared at –196, 6 and

13 °C. On the other hand, no such transition was found for a sample deposited at 100 °C. The texture transition occurred even for Cu substrates, indicating that differential thermal expansion was not the source of strain energy. But as the deposits were observed to become concave when removed from the substrate, the author assumed internal strains produced during deposition to be the responsible driving force.

Also Zielinski, Vinci and Bravman found the deposition temperature to be an important factor for (100) grain growth. They [Vinci *et al.* 1995a, Vinci *et al.* 1995b, Zielinski *et al.* 1994, Zielinski *et al.* 1995a] carried out several studies on Cu thin films. They often observed (100) abnormal grain growth but in some cases they also reported that (100) grain growth was suppressed. Therefore Zielinski et al. [Zielinski *et al.* 1995c] tried to elucidate the driving force for the abnormal grain growth. (100) grain growth only occurred in the 1.2 µm thick Cu film which was deposited at room-temperature while no (100) grain growth was observed for films deposited at high temperature. Stress measurements indicated that the “iso-strain” assumption was only valid for films deposited at room temperature. High temperature deposition resulted in “iso-stress” like behaviour. Only the isostrain averaging would be consistent with a strain energy driving force favouring (100) grain growth. Cross-sectional TEM revealed that the room-temperature deposited film was non columnar, while the elevated deposition temperature samples were either fully columnar or had a significant fraction of regions with equiaxed grains. Therefore the authors suggested that the degree of columnarity controlled the behaviour.

Some authors assume the defect density in the sputter deposited films to be the source of driving force for (100) grain growth [Patten *et al.* 1971, Nitta *et al.* 1992].

In 1971, Patten et al. [Patten *et al.* 1971] observed (100) grain growth for very thick (1 mm) Cu films on a Cu substrate. The as-deposited Cu was strongly (111) textured, and after room temperature annealing an almost complete reorientation towards a (100) texture took place. By means of metallography and XRD, they found out that the transition rates were increased by increasing bias, gas purity and deposition rate. However, the driving force for this texture transition could not be thermal stresses, as the substrate was Cu. Another possible driving force may have resulted from internal stresses due to defects like dislocations which are produced during fabrication.

Nitta et al. [Nitta *et al.* 1992] observed a transition from a (111) to a (100) texture for 1-1.5 µm thick films deposited under relatively high ion bombardment energies (substrate voltage more negative than -50V) and/or high ion flux densities (number of bombarding Ar ions per single deposited Cu atom) during annealing at 450°C. Therefore revealing a high total amount of energy deposited to the film to be responsible for the observed texture transition, which is accompanied by the growth of giant grains as large as 100 µm. On the other hand, no such texture transition was found for a reduced Ar ion bombardment during film deposition.

The results of Park et al. [Park *et al.* 2007] support the assumption that the defects play an important role for (100) grain growth. When investigating the effect of loading frequency on thermal fatigue damage in sputtered Cu lines, they found deformation-induced growth of (100) oriented grains. The authors attributed this observation to an increased grain boundary mobility due to the motion of dislocations to the boundary.

2.3.2 Texture and grain growth in electroplated films

Electroplating of Cu exhibits superior filling properties; therefore it is the most popular method for Cu deposition in the microelectronics industry. But as there are various additives in the plating bath as well as differences in processing parameters, a wide variety of different results have been published. Nevertheless, interesting observations have been made, helping to get an overview of texture evolution in Cu thin films.

2.3.2.1 As-deposited state

Starting with the initial as-deposited texture, different observations have been made. As for the sputtered films, the most commonly observed texture components are (111), (100) and random [Gangulee 1972, Perez-Prado and Vlassak 2002, Pantleon and Somers 2006a]. Also twin orientations were found to appear [Field *et al.* 2005a]. But as electroplating offers even more differences in deposition parameters (e. g. current density, additives, bath concentration), the results are more varying.

Barrier layer

Sekiguchi et al. [Sekiguchi *et al.* 2003] observed different textures on varying interlayers for 900 nm thick films. The film prepared on Ta exhibited a strong (111) texture while a TaN sublayer caused a mixed texture consisting of (111), (100) and (110). On the other hand, Lingk et al. [Lingk *et al.* 2000] found a strong and sharp (111) fiber texture for their 1 μm thick Cu films on a TaN interlayer. Ueno et al. [Ueno *et al.* 1999] observed their as-deposited films to have almost the same texture as the underlying seed layer (either random or (111) oriented).

Bath chemistry

Field et al. [Field *et al.* 2005b] investigated the effect of bath chemistry on texture and microstructure evolution in Cu films. They found either a weak or strong (111) texture for different bath chemistries. Choi et al. [Choi *et al.* 2000] were able to produce either (111), (100) or (110) textured 35 μm thick Cu films, by changing electrodeposition conditions (concentration and current density) of copper sulphate baths. Interesting results were revealed by Yang and Lee [Yang and Lee 1999] for much thicker (10 to 60 μm) Cu films. Their texture changed from (110) to (111) with increasing cathode current density and with decreasing bath temperature. The authors attributed this change to the varying ion concentration which increased with increasing bath temperature and decreasing current density.

Hong et al. [Hong *et al.* 2007, Hong *et al.* 2006] found a dominant (110) texture for 8 to 60 μm thick, electroplated Cu films and they revealed an increasing in-plane rotation alignment parallel to the flow direction of the current with increasing film thickness.

Film thickness

Conflicting results have also been published concerning the influence of film thickness on the initial texture. Lagrange et al. [Lagrange *et al.* 2000] found a dominant (111) texture for their 0.5 to 3 μm thick films, while Perez-Prado and Vlassak [Perez-Prado and Vlassak 2002] found different results for varying film

thicknesses. With increasing film thickness the volume fraction of (111) oriented grains decreased, while the number of (100), (110) and randomly oriented grains increased. Also Pantleon and Somers [Pantleon and Somers 2006a] identified a decreasing (111) volume fraction for increasing film thickness. Their as-deposited films consisted of a dominant (111) fiber texture with a much weaker (100) component. This result was attributed to a decreasing influence of the underlying (111) textured barrier layer with increasing film thickness. Gangulee [Gangulee 1972] found a stronger (111) intensity for the thinner films when investigating the microstructure of 0.5 to 4 µm thick electroplated Cu films on a Ti interlayer. As the film thickness increase, he assumed them to approach a random orientation. Stangl et al. [Stangl *et al.* 2008] found the same behaviour for 50 nm to 2 µm thick electroplated Cu films on Ta interlayer. With increasing film thickness the strong (111) fiber texture disappeared and was replaced first by (511) twins and followed by other components like (311), (411) and (110). The decrease in (111) component was again attributed to the decreasing influence of the interlayer.

2.3.2.2 Texture after annealing

Again heating experiments as well as room temperature storage revealed different results (Tab. 2.3). As for sputter-deposited films, either an increase in (111) or (100) was observed. Additionally, in some studies a decrease in (111) fraction accompanied by the appearance of twin components was reported.

<u>Increase in (111) texture component</u>

Brongersma et al. [Brongersma *et al.* 2002b] found for a 1.15 µm thick Cu film after annealing at temperatures up to 95°C an increase in (111) volume fraction and a slight decrease in (100) concentration. Ritzdorf et al. [Ritzdorf *et al.* 1998] observed a strong increase for the (111) texture component during annealing at temperatures between 2 and 62 °C in the initially poorly textured 1.5 µm thick films (Fig. 2.11). Similarly, Cabral et al. [Cabral Jr. *et al.* 1999] identified such an increase in the (111) texture fraction for their 1 µm thick, electroplated Cu film during room temperature storage.

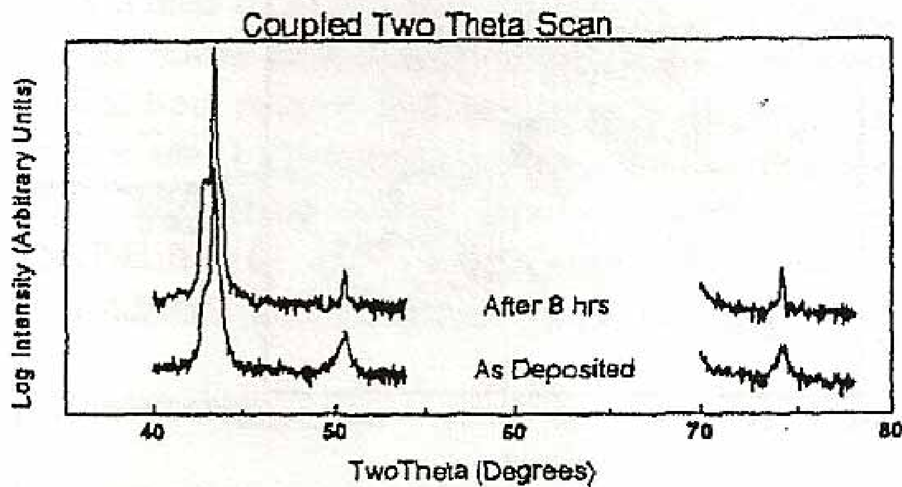

Figure 2.11: XRD line profiles for electrochemical deposited copper films: as deposited, and after self-annealing. A strong increase for the (111) texture component is observed for a 1.5 µm thick film [Ritzdorf *et al.* 1998].

Decrease in (111) texture component – multiple twinning

Some authors found a decrease in (111) texture component, which was attributed to multiple twinning [Lingk *et al.* 2000, Field *et al.* 2005a, Perez-Prado and Vlassak 2002, Mirpuri *et al.* 2006, Jiang *et al.* 1998]. Single twinning of the (111) peak results in a (511) component, while multiple twinning gives rise to (112), (5 7 13) and (522) orientations. The twinning occurred either at room temperature [Pantleon and Somers 2006a, Pantleon and Somers 2007, Lingk *et al.* 2000, Walther *et al.* 2000, Mirpuri *et al.* 2006] or at temperatures as high as 600°C [Perez-Prado and Vlassak 2002]. The twinning behaviour was found for a wide range of film thicknesses from 0.48 [Field *et al.* 2005a] to about 5 µm [Pantleon and Somers 2006a, Pantleon and Somers 2007, Walther *et al.* 2000]. Nevertheless, some authors found the film thickness to have significant influence on twinning capacity.

Field et al. [Field *et al.* 2005a] examined grain growth and texture evolution in electroplated Cu films of 480 and 750 nm thickness using EBSD measurements. The (111) texture weakened considerably with a significant increase of the twin fraction, as film thickness increased. The same result was reported by Pantleon and Somers [Pantleon and Somers 2006a, Pantleon and Somers 2007]. After room temperature storage, a texture consisting of multiple fiber components with a (111) fiber texture as the main component was identified for 0.4 to 4.8 µm thick Cu films. The strength of

the (111) component increased with decreasing film thicknesses. The minor texture components were related to multiple twinning. No texture evolution was observed for the 0.4 µm thick film.

In contrast, Perez-Prado and Vlassak [Perez-Prado and Vlassak 2002] identified a significant decrease in (111) fiber intensity only in their thinnest film (film thickness: 0.89 to 3 µm) after annealing at 400 or 600 °C. The texture randomization can be attributed to multiple twinning.

Park and Field [Park and Field 2006] tried to explain the tendency of some Cu films for multiple twinning. They proposed to consider the grain boundary energy as part of the total system energy. As the grain boundary energy of twins is much lower than that of random high angle grain boundaries, their formation contributes to a total energy minimization of the system. Assuming that a grain boundary existed, the total energy of the system with and without a twin was calculated. Following their model, twin boundaries were preferentially formed in thicker films annealed at lower temperatures (as strain energy is not significant there) but they were avoided in thin films annealed at high temperatures.

Increase in (100) texture component

On the other hand, an increase in (100) texture fraction was observed by various authors during annealing. The preferred growth of (100) oriented grain is mostly attributed to strain energy minimization and was observed for films thicker than 0.9 µm [Brongersma *et al.* 2002a, Brongersma *et al.* 2002b, Lee *et al.* 2000, Pantleon and Somers 2006a,Pantleon and Somers 2006b, Choi *et al.* 2000, Yang and Lee 1999].

Brongersma et al. [Brongersma *et al.* 2002a, Brongersma *et al.* 2002b] attributed the increase in (100) volume fraction to a tensile stress buildup due to grain boundary volume elimination. A similar explanation was given by Lee et al. [Lee *et al.* 2000] for 1 to 1.8 µm thick Cu films. After several hours, wafer curvature measurements revealed a strong tensile stress increase, which was attributed mainly to grain growth. However, the texture remained unchanged, until the stress exceeded a critical thickness-dependent value. Then the (100) texture component became

favoured over the (111) texture for minimization of strain energy in the films. No such change in stress and texture was found for films thinner than 1 µm.

Besides multiple twinning, Pantleon and Somers [Pantleon and Somers 2006a,Pantleon and Somers 2006b] also found a slight increase in (100) texture fraction during room temperature storage (Fig. 2.12). Analysis of the evolution of the line width of the (111) and (100) line profiles revealed a preferred growth of the (100) oriented grains. Their growth began earlier and faster than growth of the (111) oriented grains, although they were initially smaller (10 nm) than the (111) oriented crystallites (50 nm).

On the other hand, Vanstreels et al. [Vanstreels *et al.* 2006] observed abnormal (100) grain growth for 200 to 500 nm thick electrodeposited Cu films. But as grain growth was only observed for films deposited onto a 500 nm thick Cu seed layer, the total thickness is again increased. Neither for thinner seed layers nor varying barrier layers, abnormal grain growth was found. This behaviour could be understood assuming that the (100) oriented grains were initiated in the seed layer and then grew throughout the electroplated film. By changing the thickness of the electroplated films from 200 to 500 nm, an increase in abnormal grain growth velocity for the thicker film was revealed.

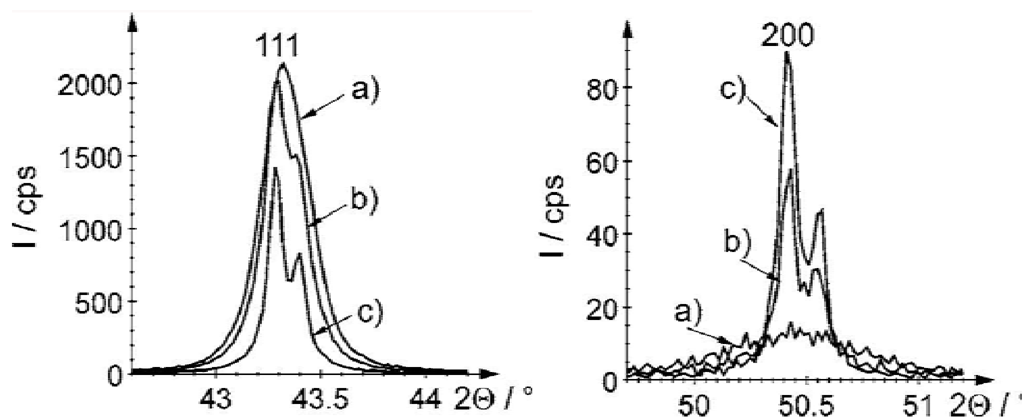

Figure 2.12: XRD line profiles for the (111) and (200) lattice planes, 5 min (a), 27 h (b), and 3 days (c) after deposition of a 2.7 µm thick Cu film. Note, the Kα_2 component is not stripped in the graphs. In the as-deposited state (111) grains have higher intensities than (100) grains. During room-temperature storage the volume fraction of the (111) component decreases drastically with time, while the (100) fraction increases [Pantleon and Somers 2006a].

Similar to sputtered Cu films, not all results can be explained by elastic strain energy minimization alone.

A transformation from a (111) textured as-plated 35 µm thick Cu film to a (100) texture during annealing was found by Choi et al. [Choi *et al.* 2000]. As these electrodeposits were peeled off from the substrate, strain due to different thermal expansion coefficients of deposit and substrate could not be responsible for the preferred growth of the (100) component. On the other hand, these results are in excellent agreement with the prediction of the strain energy release maximization model [Lee 2005b], assuming high dislocations densities to be the dominant driving force.

The same results were observed by Yang and Lee [Yang and Lee 1999] for a 60 µm thick, freestanding Cu film. The initially (111) texture changed to a dominant (100) texture when the samples were annealed at 600 °C.

Tabel 2.3: Results of microstructural analysis of electrodeposited Cu films after annealing or room temperature storage. The film thickness *h*, the annealing Temperature T_a, as well as the substrate and barrier layer are listed. Furthermore the seed layer and its thickness (in brackets) are shown. These seed layers were sputter deposited prior to electroplating and act as an anode in the electrochemical deposition of the Cu films.

Literature	h [µm]	Substrate/Barrier/Seed	T_a [°C]	Texture
Brongersma et al. 2002a/b	1.15	(100)Si /SiO_2/TaN/Cu(150nm)	50-90	(111)
			400	(100)
Ritzdorf et al. 1998	1.5	/	2 - 62	(111)
Cabral et al. 1999	1	/	RT	(111)
Lingk et al. 2000	1	Si /SiO_2/TaN/Cu(100nm)	RT - 400	twinning
Field et al. 2005a	0.48 0.75	Si/Ta/Cu(100nm)	400	twinning
Perez-Prado and Vlassak 2002	0.89	(100)Si/SiN_x/TaN/Cu	400 - 600	twinning
	1.81			no change
	3.0			no change
Mirpur et al. 2006	1	Si/SiO_2/Ta/Cu(50nm)	RT - 400	twinning
Jiang et al. 1998	0.96 1.72 3.39	SiO_2/…/Cu(100nm)	RT	twinning
Pantleon and Somers 2006a/b	0.4	(100)Si/Ti/Au	RT	no change
	0.9-4.8			twinning + (100)
Walther et al. 2000	0.25 0.5 - 5	Si/Ta/Cu(100nm)	RT	no change twinning
Lee et al. 2000	0.45-0.65 1.1 – 1.9	…/Ta/Cu(100nm)	RT	no change (100)
Vanstreels et al. 2006	0.7 - 1	(100)Si/SiO2/Si3N4/TaN/Cu	RT	/
		(100)Si/SiO2/Si3N4/β-Ta/Cu		
		(100)Si/SiO2/Si3N4/TaN/α-Ta/Cu(100nm)		
		(100)Si/SiO2/Si3N4/TaN/α-Ta/Cu(200nm)		
		(100)Si/SiO2/Si3N4/TaN/α-Ta/Cu(500nm)		(100)
Choi et al. 2000	35	freestanding	600	(100) (√3 1 0)
Yang and Lee 1999	30-60	freestanding	600	(100) (√3 1 0)

Grain growth velocities and driving forces

As described above, many authors adopted the texture evolution model of Thompson [Thompson and Carel 1995, Thompson and Carel 1996a]. Therefore they regarded surface energy minimization and strain energy minimization to be the main driving forces for texture evolution. However, analysing the transformation rate or grain growth velocity, some interesting results for the underlying driving force have been found. A general trend was identified, as an increasing transformation rate was found for increasing film thickness. Various attempts to explain these results were made.

Several authors assumed grain boundary energy to be the responsible driving force for the observed microstructural changes in Cu thin films. But as this driving force alone could not explain an increased grain growth velocity for an increased film thickness, different possible explanations have been proposed: Walther et al. [Walther *et al.* 2000] assumed impurities and hence grain boundary pinning to be responsible. The authors proposed that grain boundary pinning prevented the thinnest films (0.25 and 0.5 µm thick) from grain growth, and the increased transformation rate was attributed to a decreasing influence of the surface, as film thickness increases (Fig. 2.13).

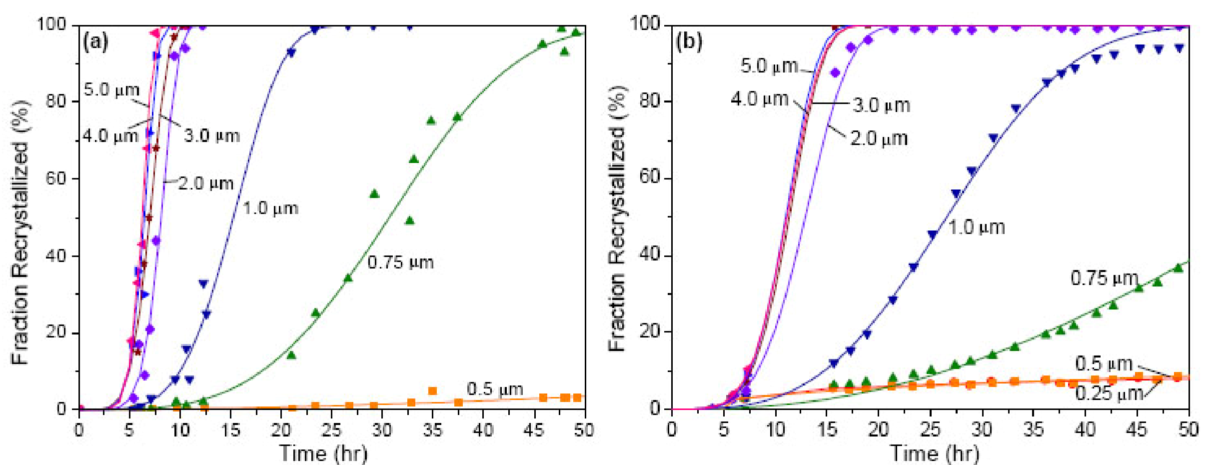

Figure 2.13: Fraction of recrystallized Cu as a function of time for electroplated Cu films of different thicknesses, as derived from (a) FIB secondary electron images, and (b) sheet resistance measurements. An increased transformation rate was observed for an increase in film thickness from 0.75 to 5 µm, while little recrystallization is reported in films thinner than 0.75 µm. The combination of the two techniques led to the conclusion that nucleation occurred near the surface of the film. [Walther *et al.* 2000].

Alternatively, Lagrange, Brongersma and Jiang [Lagrange *et al.* 2000, Brongersma *et al.* 1999a, Jiang *et al.* 1998] assumed a transition from a 3-dimensional to a 2-dimensional grain growth to explain the decrease in grain growth rate for thinner films when the film thickness approached the grain size of the new grains.

A similar approach was made by Brongersma et al. [Brongersma *et al.* 1999b] who found a faster decrease in sheet resistance as film thickness increased. Analysis of grain growth data from cross-sectional images, suggested a two step grain growth behaviour. First, an initial crystallization occurred from the top down and formed a recrystallized top-layer of about 500 nm thickness. Then in a next step, lateral abnormal grain growth took place, where large grains started to absorb the surrounding matrix grains. As more small grains were left underneath the initially crystallized layer, thicker films were able to transform much faster. Teh et al. [Teh *et al.* 2001] referred to this model to explain the observed shorter initiation time and faster transformation, when the Cu film thickness increased from 0.5 to 3 µm.

As in some cases, the observed changes in transition velocity were correlated to different initial textures, some authors assumed them to be responsible for varying grain growth velocities [Ueno *et al.* 1999, Pantleon and Somers 2006a, Pantleon and Somers 2007, Stangl *et al.* 2008]. Pantleon and Somers and Stangl et al. found increasing kinetics for increasing film thicknesses (Fig. 2.14). The authors attributed this behaviour to the different as-deposited textures: the thicker the films, the more grains with other orientations than (111) exist, i.e. (100) which form high angle grain boundaries to the surrounding matrix. As high angle grain boundaries were said to have a higher mobility [Humphreys and Hatherly 1995, p 134], this was said to cause a relatively rapid microstructure transformation. The larger the volume fraction of (111) oriented grains, the more likely is the dominance of low-angle grain boundaries and hence the slower is the kinetics of self-annealing.

The explanation given by Harper et al. [Harper *et al.* 1999] for the dependence of the transformation rate on film thickness is much simpler. The authors analysed the results of Gignac et al. [Gignac *et al.* 1999], who found that electroplated films of 1 µm thickness or greater had substantially the same transformation time (the time for half of the resistivity decrease to occur), while the transformation slowed down when film thickness decreased down to 0.1 - 0.2 µm. Harper et al. assumed that the area density of nucleation sites increased linearly with film thickness, therefore

predicting the transformation time to be inversely proportional to film thickness. A simple function which embodies this inverse dependence on film thickness fits well to the experimental results.

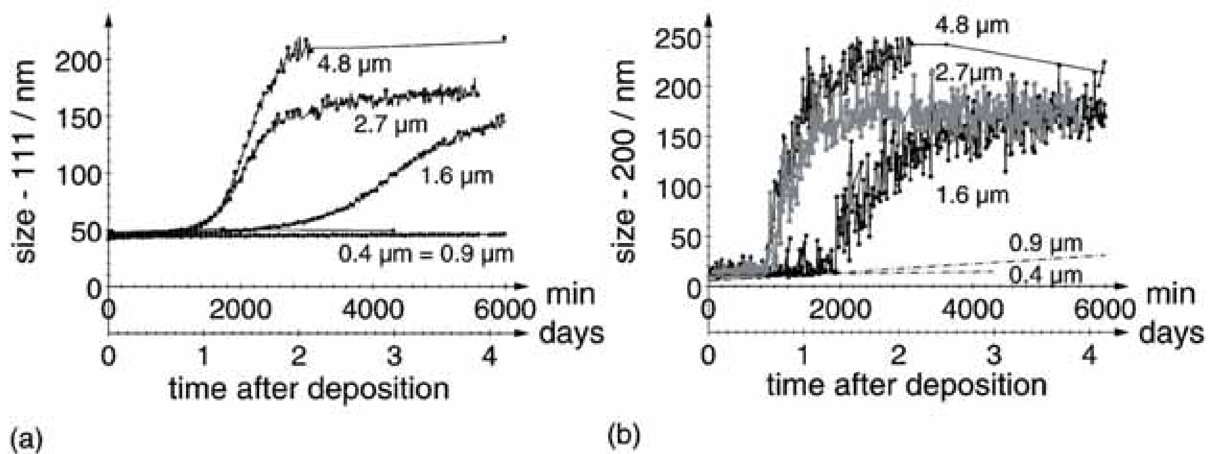

Figure 2.14: Crystallite size calculated from the broadening of (111) (a) and (100) (b) diffraction lines. The as-deposited crystallite sizes were 50 nm for (111) oriented grains and about 15 nm for the grains with (100) orientation. As grain sizes larger than 200 nm could not be determined by conventional XRD, it could not be concluded whether a stable grain size had actually been reached and what the final stable grain size was. [Pantleon and Somers 2006a].

Furthermore, defect densities were supposed to act as dominant driving force. When Jiang et al. [Jiang *et al.* 1998] found an increasing transformation rate towards a more random texture for the thicker films of their 0.96 to 3.39 µm thick films, they supposed the higher total amount of free energy in the thicker films to be responsible for the increased velocity.

Similarly, several other authors assumed the initial defect density, in as-deposited grains, to be the reason for the observed microstructural changes [Detavernier *et al.* 2003a, Detavernier *et al.* 2003b, Patten *et al.* 1971, Nitta *et al.* 1992, Choi *et al.* 2000, Yang and Lee 1999, Lee *et al.* 2004, Lingk and Gross 1998, Stangl *et al.* 2008, Schell *et al.* 2005]. When varying parameters like the current density and plating temperature which are assumed to have influence on the defect density, big variations in grain growth velocities were reported. Several authors [Stangl *et al.* 2008, Lee *et al.* 2000, Ritzdorf *et al.* 1999, Lagrange *et al.* 2000, Lee *et al.* 2004] observed an increased transformation rate for an increasing current density. They attributed the increase in grain growth velocity to a higher defect density. Similarly, Lee et al. [Lee *et al.* 2004] observed faster grain growth for increasing plating current densities. By TEM imaging the authors were even able to prove the

existence of a high density of dislocation loops in as-deposited grains and they reported an increased dislocation density for higher plating current densities. For sputter-deposited films, Schell et al. [Schell *et al.* 2005] found a decrease in grain growth rate when increasing the substrate bias voltage for 100 - 130 nm thick Cu films. This decrease is proposed to depend on a decrease in defect concentration as the mobility of the surface atoms increases. When Vanstreels et al. [Vanstreels *et al.* 2008] observed a increased grain growth velocity for decreased sputter-bias conditions (250 to 0W), they proposed defect concentration to act as a driving force. Nevertheless, no clear differences in defect densities for different sputter-bias conditions were found by TEM-studies. Harper et al. [Harper *et al.* 1999] ruled out the dislocation density as a major driving force for grain growth, as they observed no increase in the as-deposited resistivity. Dislocations are known to increase the resistivity. And Militzer et al. [Militzer *et al.* 2004] and Freundlich et al. [Freundlich *et al.* 2002] proposed another explanation for an increased annealing rate for increasing current density. They assumed grain boundary energy to be the dominant driving force as the increase in current density was accompanied by a decreasing grain size.

2.3.4 Activation energy

The activation energy of grain growth was determined by several authors. Not all of them give additional information about the grain growth mode and texture evolution. Nevertheless, a value of about 0.9 eV/atom was found in several studies.

Schell et al. [Schell *et al.* 2005] found the measured activation energy for grain growth to be 0.90±0.08 and 0.82±0.07 eV, for bias voltages of -75 and -150 V, respectively. These values correspond to grain boundary self-diffusion (0.88 – 0.92 eV/atom [Surholt *et al.* 1994, Gupta 1994]). Furthermore, these activation energies were in good agreement with the measurements of Detavernier et al. [Detavernier *et al.* 2003b], who found a corresponding value of 0.9 to 1 eV in sputter-deposited and electroplated Cu films. Similarly, Cabral et al. [Cabral Jr. *et al.* 1999] found the activation energy to be 0.9 eV for 1 µm thick, electroplated Cu films.

Brongersma et al. [Brongersma *et al.* 2002a, Brongersma *et al.* 2002b] found the activation energy of the occurring grain growth to be 0.92 eV for an observerd increase in (111) texture fraction.

Ritzdorf et al. [Ritzdorf *et al.* 1998] found a activation energy of 1.1 eV for 1.5 µm thick Cu films annealed at temperatures between 2 and 62 °C. The activation energy was calculated based on time that it took to complete half the sheet resistance change. This grain growth resulted in an increase in (111) texture fraction.

Based on differential scanning calorimetry, Yin et al. [Yin *et al.* 2008] determined an activation energy of 0.85 eV for 18 µm thick electroplated copper deposits.

Vanstreels et al. [Vanstreels *et al.* 2008] determined the activation energy of the abnormal grain growth to be 0.77 eV ± 0.05 eV. This value is lower than the value of 0.93 eV that is found for normal grain growth.

Thompson obtained values from DSC (0.62 eV) and *in situ* TEM (0.9 eV) [Hau-Riege and Thompson 2000, Donthu *et al.* 2003].

All of these results are close to the reported activation energies for grain boundary self-diffusion (0.88 eV – 0.92eV).

The observed activation energies are summarized in Tab. 2.4, together with important experimental parameters and measurement techniques.

Tabel 2.4: Activation energies E_a as determined by different authors for grain growth in Cu thin films. An increase in (111) or (100) texture is marked by (111)↑ and (100)↑, respectively.

Reference	E_a [eV/Atom]	Deposition	Method	Film thickness	Texture
Schell *et al.* 2005	0.90 0.82	-75 V sputtered -150V sputtered	XRD	100-130 nm	(111)↑
Detavernier *et al.* 2003b	0.9 – 1	sputtered and electroplated	Resistivity change	100-970 nm	/
Cabral Jr. *et al.* 1999	0.92	electroplated	Resistivity change	1 µm	(111)↑
Brongersma *et al.* 2002a	0.92	electroplated	Resistivity change	1.15 µm	(111)↑
Ritzdorf *et al.* 1998	1.1	electroplated	Resistivity change	1.5 µm	(111)↑
Yin *et al.* 2008	0.85	electroplated	DSC	18 µm	/
Vanstreels *et al.* 2008	0.77 0.79	50 W sputtered 250 W sputtered	EBSD	100-500 nm	(100)↑
Hau-Riege and Thompson 2000	0.9	electroplated	TEM	300 nm	/
Donthu *et al.* 2003	0.62	electroplated	DSC	1.5 µm	/

2.3.5 Summary of the state of the literature and aim of the study

In the past years, numerous studies have been carried out on Cu thin films, giving insight into texture formation and grain growth.

Concerning the initial texture, consistent results were observed: Three main fiber components are identified in most of the studies for sputtered as well as electrodeposited as-deposited Cu films: (111), (100) and a random component – but their fraction varies. On amorphous or weakly textured interlayers, all three texture fractions are observed, while a highly textured interlayer leads to an increased (111) fraction – weakening the (100) and/or random fraction. On the other hand, a randomly oriented interlayer results in a random Cu texture. Furthermore, twinning of the (111) and (100) component creates additional texture components such as (511) and (221). Beside the interlayer, the microstructure development during deposition is influenced by deposition parameters such as gas pressure, the target-substrate distance or the substrate bias voltage as well as current density, additives and bath concentration for electroplated films.

Annealing of the as-deposited films resulted in different final textures: some authors found the (111) texture component to increase during annealing. This behaviour is mostly reported in Cu thin films – the upper limit of film thickness mostly lying between 500 nm and 1 µm. It is likely that the driving force for this texture development is the minimization of the surface energy. For electroplated Cu films, some authors found a decrease for the (111) texture component which was attributed to multiple twinning. In contrast, several studies show a texture transition to a dominant (100) fiber texture during annealing for sputtered and electrodeposited Cu films. Mostly, this behaviour was found for films thicker than 500 nm. In general, this behaviour is ascribed to strain energy, due to differential thermal expansion, as the dominant driving force. But that does not hold for all studies, as an increase in (100) was also observed for free-standing Cu films and for Cu substrates.

Several authors reported increased grain growth velocities for thicker films and various attempts to identify the underlying driving force have been made. Some authors assume grain boundary energy to be the responsible driving force. Walther et al. [Walther *et al.* 2000] proposed that the decreasing influence of grain boundary pinning gives the explanation for the higher grain growth rate for thicker films. On the

other hand, Lagrange and Brongersma [Lagrange *et al.* 2000, Brongersma *et al.* 1999a] assumed a transition from 3-dimensional to 2-dimensional grain growth to explain the decrease in grain growth rate for thinner films. While others propose the defect density, incorporated in as-deposited grains, to be the reason for the observed microstructural changes. As in some studies the observed increase in transition velocity is correlated to different initial textures, several authors assume them to be responsible for varying grain growth velocities. The larger the volume fraction of (111) oriented grains, the more likely is the dominance of low-angle grain boundaries and hence the slower is the kinetics.

It is obvious that further work is necessary to find explanations for the various conflicting observations. Deeper insight into the basics of grain growth in thin films would allow to develop new deposition, fabrication or heat treatment rules to improve future nano-technological devices. Therefore, the EBSD technique is used in this study, giving simultaneously information about the microstructure and texture.

The texture evolution model developed by Thompson and Carel [Thompson and Carel 1995, Thompson and Carel 1996a] was a first step to predict textures for annealed thin films as a function of film thickness and annealing temperature. While some general trends can be explained by this model, it is impossible to predict the details of grain growth and texture evolution. The first aim of this study was to determine the texture of 0.5 to 10 µm thick Cu films after annealing. This observation indicated again that more information is needed about the details of grain growth.

As most of the studies on texture development in thin films used XRD methods for orientation determination, another goal of this study was the comparison of EBSD and XRD results. Detailed comparison with results based on X-ray diffraction (XRD), using both $\theta/2\theta$ and ψ scans, was made, discussing the pros and cons of each technique.

Up to this point, strain was introduced through a change in temperature into the film – therefore it is impossible to vary temperature and strain independently. In the next step, this restriction is removed by carrying out uniaxial tensile tests. As a polyimide foil can be deformed elastically to strains of more than 3%, it is possible to induce strain energy by uniaxial loading. A new testing appliance was constructed, which allows to carry out tensile tests and/or heating experiments in a SEM. Thus, it was possible to conduct tensile test while observing grain growth via EBSD.

In order to get additional insight into grain growth, a systematic series of measurements for varying film thicknesses and annealing temperatures were carried out. Detailed analysis of the abnormal growth of individual (100) oriented grains for more than 24 hours at different temperatures lead to conclusions that would be unreachable without *in situ* capacity. Analysis of grain growth velocities for different film thicknesses and annealing temperatures allowed to reveal more information about basic mechanisms of abnormal grain growth.

Chapter 3 EBSD

Conventional light microscopy allows to image grain boundaries and therefore to investigate grain growth. But no information about the orientation of the grains is given. On the other hand, XRD techniques provide textural information but no image of the grain structure is available. Therefore, it is not possible to trace a specific grain and investigate its growth. Electron backscatter diffraction (EBSD) combines both advantages: it is possible to gain microstructure and orientation information simultaneously. Nevertheless, in the beginnings of this technique measuring times were very high and indexing was complex and time consuming. Automation of pattern indexing strongly facilitates this procedure and has greatly reduced the measuring time.

Nowadays, the EBSD technique in a SEM is a powerful method for different applications. The automated collection rate of EBSD data has steeply increased in the last years, making acquisition rates of about 100 patterns/second possible

[Oxford 2007]. This allows microstructural investigations of extended areas in relatively short time. The nominal angular resolution is 0.3° [Oxford 2007] and the spatial resolution is related to the resolution of the SEM. In modern field emission SEMs several tens of nanometers can be measured with reasonable accuracy.

EBSD works by arranging a flat sample at an angle of usually 70° below the incident electron beam (Fig. 3.2). Tilting the specimen reduces the path length of backscattered electrons, thus allowing a greater proportion of them to escape towards the detector. At an accelerating voltage of 20 kV and a high incident beam current (1 – 50 nA), electron diffraction occurs from the point where the beam hits the sample surface. Holding the beam stationary, an EBSD pattern is formed from the top 10 - 50 nm of the specimen and eradiates spherically from this point. When the primary beam interacts with the crystal lattice, low energy loss backscattered electrons are created and path differences lead to constructive and destructive interferences. On a phosphor screen, placed a short distance from the tilted sample, a diffraction pattern can be seen (Fig. 3.1). The detector is a digital camera. Its CCD chip is illuminated by the phosphor screen that intersects the spherical diffraction pattern. The phosphor converts the diffracted electrons into light suitable for the CCD camera.

The Kikuchi pattern (Fig. 3.1) consists of a several pairs of parallel lines where each pair (or band) corresponds to a specific crystallographic plane and the intersection of bands corresponds to a zone axis. Therefore, the Kikuchi pattern includes all the angular relationships in the crystal – and hence embodies the crystal symmetry.

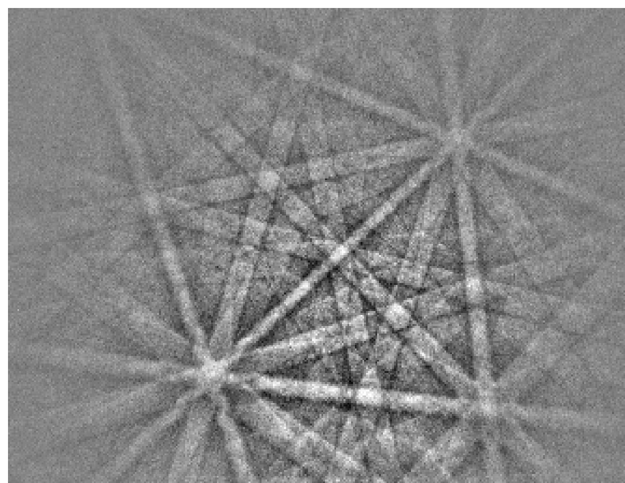

Figure 3.1: Kikuchi pattern from Cu sample (accelerating voltage 20 kV).

Specialized computer software analyzes the EBSD pattern by detecting a number of Kikuchi bands using an optimized Hough transform. This Hough transformation converts lines into points in Hough space. Kikuchi bands are transformed into bright regions in Hough space, which are used to calculate the original position of the bands. Then the angles between the planes can be calculated and compared to a list of angles for the analysed structure. Finally, the orientation of the crystal with respect to a fixed sample coordinate system is calculated.

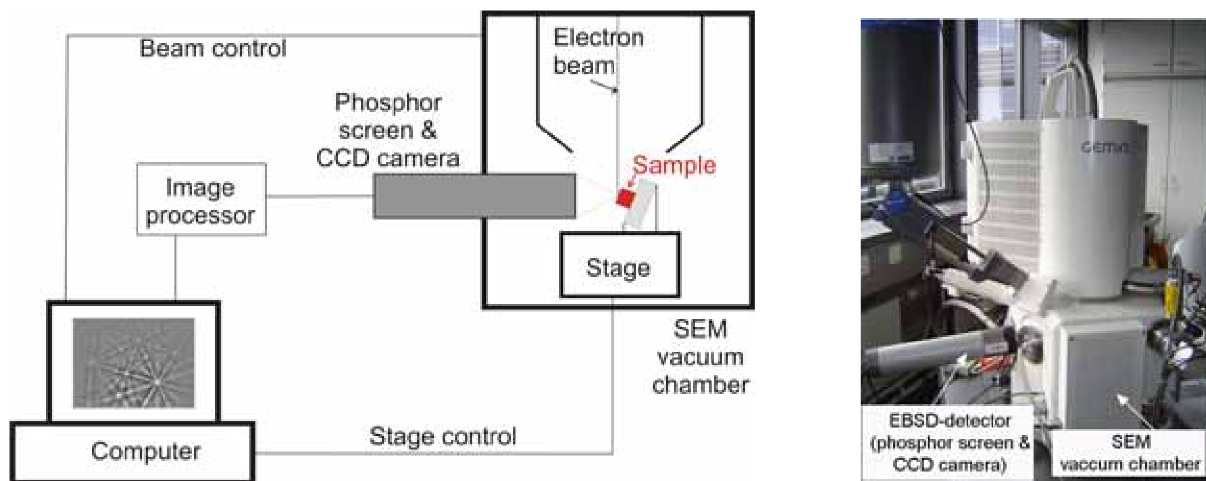

Figure 3.2: Components of an EBSD system working in a SEM (left) and real setup at a Leo 1530-VP with EBSD-detector (right).

As with conventional microscopy, EBSD maps can be used to show visually the microstructure. In order to present the crystallographic orientation, often the inverse pole figure (IPF) is used. This orientation information uses a basic RGB (Red-Green-Blue) colouring scheme which is fitted to an inverse pole figure. For cubic phases, red, green, and blue are assigned to grains whose (100), (110) or (111) axes, respectively, are parallel to the projection direction of the IPF (typically, the surface-normal direction). Intermediate orientations are coloured by an RGB mixture of the primary components (Fig. 3.3).

The band contrast is a pattern quality factor which describes the average intensity of the Kikuchi bands with respect to the overall intensity within the pattern.

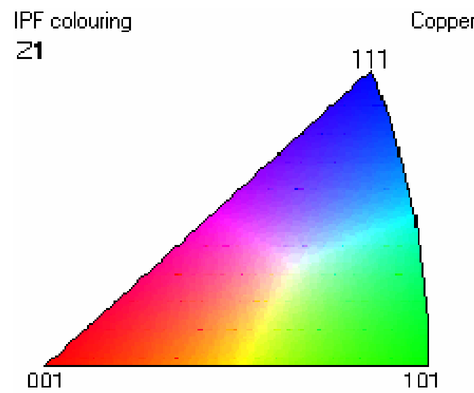

Figure 3.3: IPF: A basic Red-Green-Blue colouring scheme is fitted to an inverse pole figure. For cubic phases, red, green, and blue are assigned to grains whose (100), (110) or (111) axes, respectively, are parallel to the projection direction of the IPF (typically, the surface-normal direction).

With a scale mapped to a greyscale, maps can be plotted which show the microstructure in a fashion like in the SEM or light microscopes. The superposition of EBSD patterns of adjacent crystals at grain boundaries results in a remarkable reduction of the band contrast. In this way grain boundaries and grains become visible (Fig. 3.4).

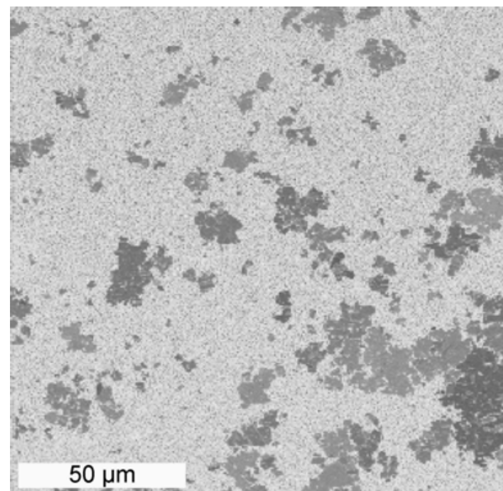

Figure 3.4: EBSD band contrast map of a 5 µm thick film during annealing at 118°C

The various textures components in a sample can be separated. With the help of the HKL software Tango, e. g. the (111) and (100) texture components are divided into subsets in order to allow a separate analysis (Fig. 3.5). A grain is allotted to a particular texture component if at least 50% of the grain possessed this particular orientation. This is especially important, as some grains included twins.

For grain detection, a critical misorientation of 5° was specified and the twin boundaries were ignored. Furthermore, the boarder grains were excluded from the grain size statistics.

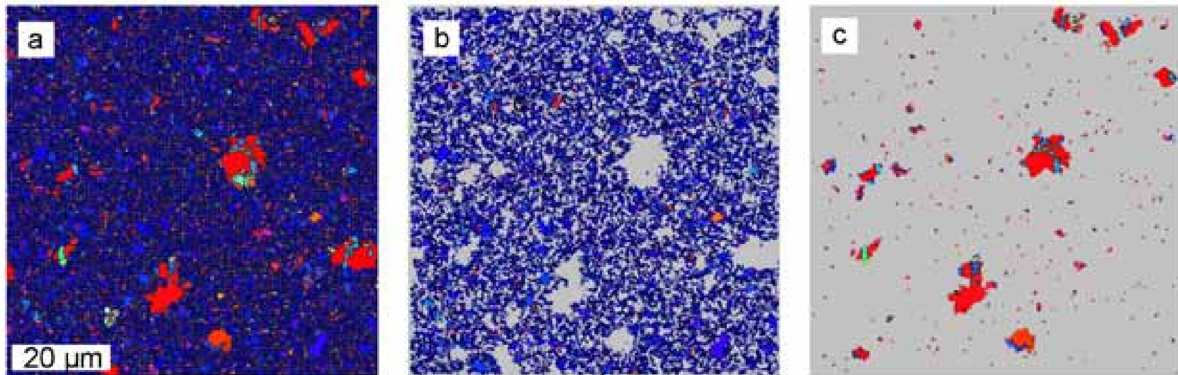

Figure 3.5: EBSD orientation maps of 2 µm thick Cu films on polyimide during annealing at 118°C. a) The orientation normal to the film surface is represented with the help of the orientation colour key shown in Fig. 3.3. b) Blue (111) oriented grains. c) Red (100) oriented grains. A grain is ascribed to a particular texture component if at least 50% of the grain possessed this particular orientation.

Chapter 4 Effect of Film Thickness on Texture

4.1 Introduction

Controlling the texture of materials is a possible route to tailor their properties: as elastic and plastic properties of crystals depend on the crystallographic direction, the preferred orientation of grains influences the mechanical behavior of a material and thus the performance and reliability of components and devices. This is especially important for thin films where defined textures develop during deposition and annealing treatments. Texture evolution is mediated by grain-boundary motion in preferred directions caused by anisotropic driving forces. While the mere reduction of grain-boundary energy, as in normal grain growth, does not favour specific grain orientations, the anisotropy of surface and interface energy can supply an orientation-dependent driving force. This results often in a (111) orientation of face-centred cubic (fcc) metal films, because the (111) plane has the lowest surface energy. In contrast, the strain energy of an fcc metal film under thermal strain favours

(100) oriented grains, which possess the smallest strain energy density. Whereas the surface/interface energy is independent of film thickness, the strain energy scales with film thickness and depends on the applied strain. Hence different textures are predicted for varying film thicknesses and strains as described in detail by Thompson and Carel [Thompson and Carel 1995]. Experiments on polycrystalline Ag films gave indeed a predominance of (111) orientations for small film thicknesses and low thermal strains, and a strong (100) texture component for thicker films and high thermal strains [Thompson and Carel 1995, Thompson and Carel 1996a].

In this study the transition in microtexture was characterized quantitatively for the first time by using electron backscatter diffraction (EBSD) in a scanning electron microscope (SEM). Cu films with different thicknesses (0.5 to 10 µm) were analysed by EBSD and, for comparison, XRD measurements. The systematic use of EBSD measurements provides, apart from texture information with spatial resolution, access to neighbor relationships as well as grain-boundary characteristics and grain size distributions. This information can provide important input for texture evolution models. The results of this study by Sonnweber-Ribic, Gruber, Dehm and Arzt have been published [Sonnweber-Ribic *et al.* 2006b].

4.2 Experimental

99.996 at% pure Cu films were deposited on 125 µm thick polyimide substrates (Kapton®, DuPont) using a UHV magnetron sputtering system (DCA Instruments). The thickness of the Cu layers was varied from 0.5 to 10 µm.

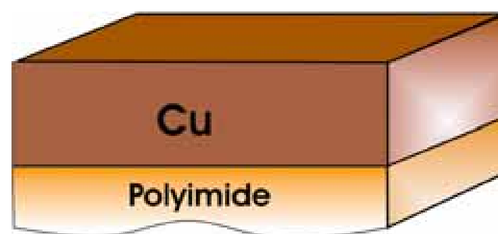

Figure 4.1: Cu thin films of thicknesses in between 0.5 and 10 µm were deposited on 125 µm thick polyimide substrates (Kapton®, DuPont).

The film deposition was performed at nominally room temperature at a base pressure of 10^{-8} Pa and a deposition rate of 28 nm/min[1]. After deposition some samples were annealed at 330 °C for two hours without breaking vacuum to obtain a stable microstructure with predominantly columnar grains. Higher annealing temperatures were not possible due to the limited thermal stability of the polyimide. Another set of samples were prepared without any heat-treatment, as-deposited for *in situ* experiments.

Table 3.1: Properties of Kapton® HN film [Dupont 2006]

Thermal coefficient of linear expansion α	$20 \cdot 10^{-6}$ 1/K
Young's modulus	2.5-2 GPa
Density	1.42 g/cm³
Poisson's ratio	0.34

Table 3.2: Properties of Cu

Component of stiffness matrix C_{11}	168.4 GPa
Component of stiffness matrix C_{12}	121.4 GPa
Component of stiffness matrix C_{44}	75.4 GPa
Young's modulus in (111) plane E_{111}	130 GPa
Young's modulus in (100) plane E_{100}	93 GPa (67-130 GPa)
Biaxial modulus in (111) plane M_{111}	261 GPa
Biaxial modulus in (100) plane M_{100}	115 GPa
Thermal coefficient of linear expansion α	$16.6 \cdot 10^{-6}$ 1/K
Density	8.92 g/cm³

The macrotexture of the heat-treated films was examined by XRD while the local orientation distribution was investigated by EBSD measurements in an SEM. $\theta/2\theta$ scans were performed with a Philips X'Pert MRD diffractometer operating in parallel-beam geometry[2]. Cu K_α radiation emerging from a sealed X-ray tube operated at 45 kV and 40 mA was paralleled by an X-ray lens (polycapillary collimator). The diffracted beam passed a parallel plate collimator (0.18° acceptance angle) and a flat graphite analyser before being detected by a proportional counter. Diffraction patterns were recorded in continuous mode. The scans were carried out

[1] The films were deposited in the thin film laboratory of the MPI for Metals Research by Ilse Lakemeyer.
[2] The XRD measurements were carried out in the ZWE of the MPI for Metals Research by Gerd Maier, Yener Kuru and Udo Welzel.

between 20 and 130° with a step size of 0.04° and a scan time of 2 sec/° (Fig. 4.2). Based on the Harris method [Harris 1952], the strength of the texture can be quantified by direct comparison of the integrated peak intensities of a textured film with those of an untextured powder sample. This normalisation takes into account the influences on the measured peak intensities which do not depend on the volume fractions of the different texture components, i.e. the multiplicity, the atomic scattering factor, the Lorentz polarisation factor and possible instrumental effects. The resulting strength of the texture gives a relative measure for the volume fraction of grains oriented with specific hkl planes parallel to the film surface.

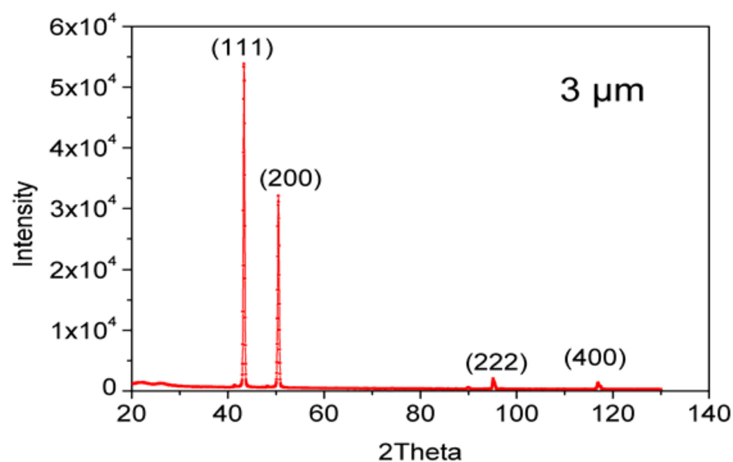

Figure 4.2: XRD line profile of the 3 µm thick Cu film after annealing at 330°C.

Pole figure measurements were performed for the Cu (111) and (200) reflections using an Eulerian cradle. The measurement direction (i.e. the direction of the diffraction vector) with respect to the specimen frame of reference is defined by the angles ψ and φ, where ψ is the inclination of the diffraction vector with respect to the specimen surface normal and φ is the rotation angle around the specimen surface normal. The integrated intensity depended on the sample tilt angel ψ but was independent of the rotation angle φ. Thus, it can be concluded that the films exhibited a fiber texture. Pole figure sections (ψ scans) for the (111) and the (200) reflections were generated from the intensity of the diffraction lines measured as a function of ψ (Fig. 4.3).

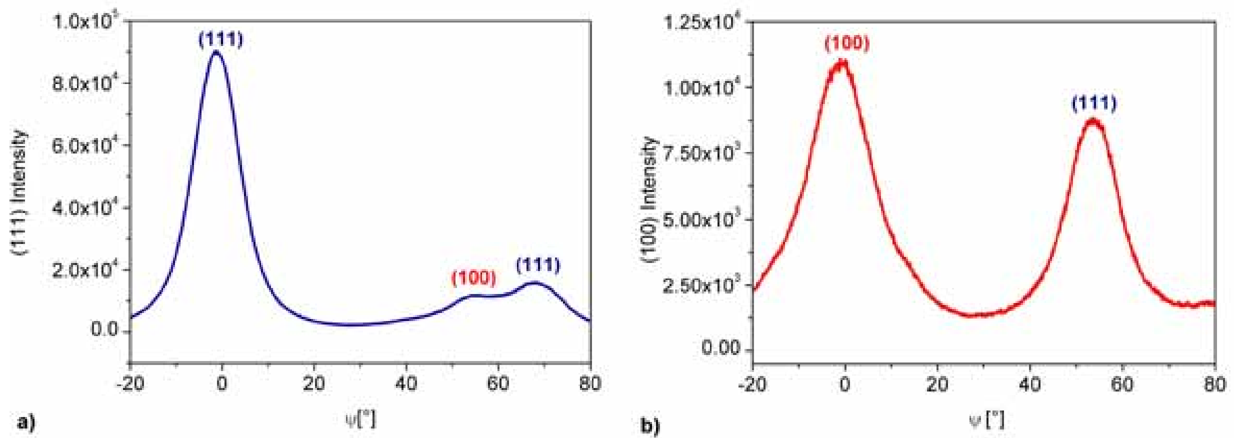

Figure 4.3: a) (111) and b) (100) pole figure scans of a 1 µm thick Cu film after annealing at 330°C.

These ψ scans were corrected for background, absorption, tilting and instrumental intensity loss, as in Welzel and Leoni [Welzel and Leoni 2002]. For texture quantification, the measured and corrected ψ scans were fitted with pole figure sections calculated from theoretical, idealized orientation distribution functions (ODFs).

The EBSD system (HKL, channel 5) used in this study is attached to a Leo 1530-VP SEM equipped with a field emission gun. The measurements were carried out at a working distance between 13 mm and 16 mm and an accelerating voltage of 20 kV. Areas of 10^2 to 10^4 µm² were scanned at step intervals of 0.05 to 0.4 µm to determine grain orientations, size and shape. The approximate time per scan was in the range of one hour. Longer scan times were avoided in order to prevent drift problems. EBSD analyses were repeated over eight to fifteen different regions for each film thickness to obtain reliable and reproducible data.

The number of grains investigated via EBSD varied from 2300 to 4100 for the different film thicknesses.

4.3 Results

4.3.1 Texture analysis

EBSD orientation maps for the Cu films are shown in Fig. 4.4. Grains marked blue are oriented with the (111) plane parallel to the surface and grains in red are (100) oriented, grains labelled green possess a (101) orientation. In order to achieve sufficient resolution as well as a large measuring area without prolonging the required scan time, the step size was increased from 0.05 to 0.4 µm with rising film thickness. The maps clearly reveal a change from a preponderance of (111) oriented grains for the thinnest film to a predominant (100) texture component for the 10 µm thick film. This change can be described quantitatively by the volume fractions of grains possessing a particular orientation (Tab. 4.1, Fig. 4.6a). These volume fractions were calculated from the area fractions of pixels of a particular orientation assuming a columnar microstructure. A maximum misorientation angle of 15° was allowed for assignment of orientations to each texture component. All other grains were classified as “random”; their volume fraction is also displayed in Fig. 4.6a. The microtexture of the 500 nm thick film consisted of 75.9 ± 1.9 % (111) and 10.0 ± 1.3 % (100) grains; for the thickest film (10 µm) the fraction of (111) grains decreased to 17.7 ± 0.7 % while the (100) fraction increased to 55.9 ± 1.7 %. Between these values, a transition in texture was observed. The interpolated “cross-over” occurred at a film thickness of about 4.2 µm. The random fraction increases to a maximum of about 25%.

Tabel 4.1: Results of EBSD measurements: V_{111} and V_{100} are the volume (area) fractions of (111) and (100) oriented grains.

Film thickness	V_{111} [%]	V_{100} [%]	Total area [µm²]	Number of specimen sites
0.5 µm	75.9 ±1.9	10 ± 1.3	1250	8
1 µm	57.7 ±2.5	19.8 ± 2.8	1250	8
3 µm	44 ± 3.5	27.5 ± 2.8	12500	8
5 µm	28 ± 4.2	38.8 ± 3.2	10000	4
10 µm	17.7 ± 0.7	55.9 ± 1.7	40000	4

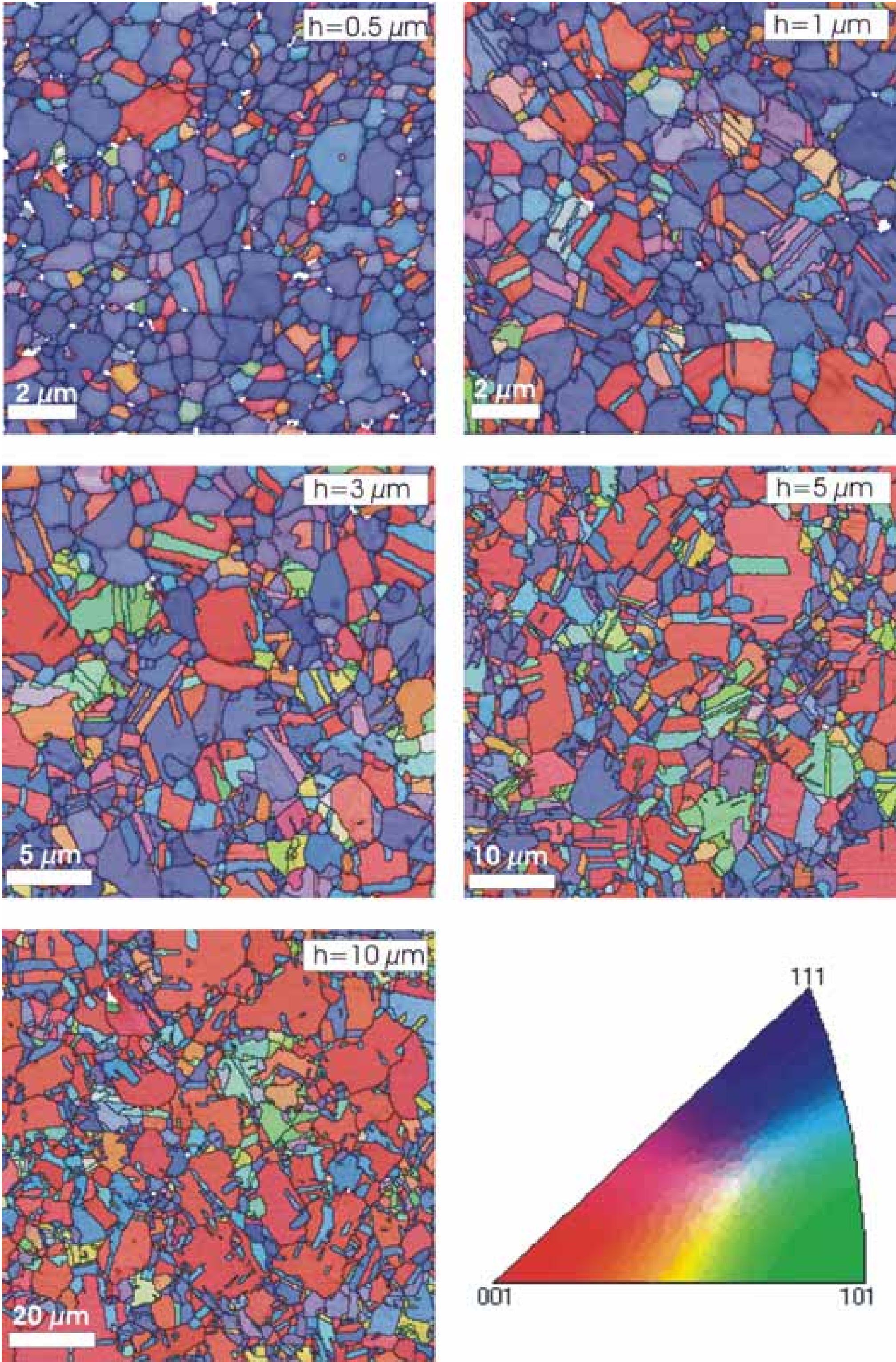

Figure 4.4: EBSD orientation maps of Cu films on polyimide with different film thicknesses: 0.5 µm, 1 µm, 3 µm, 5 µm, 10 µm. The orientation normal to the film surface is represented with the help of the orientation colour key. Note that the scale bar increases from 2 to 20 µm.

The XRD *θ/2θ* scans (Fig. 4.5) revealed also a predominance of the (111) and (100) texture components, with a negligible (311) peak (less than 2%).

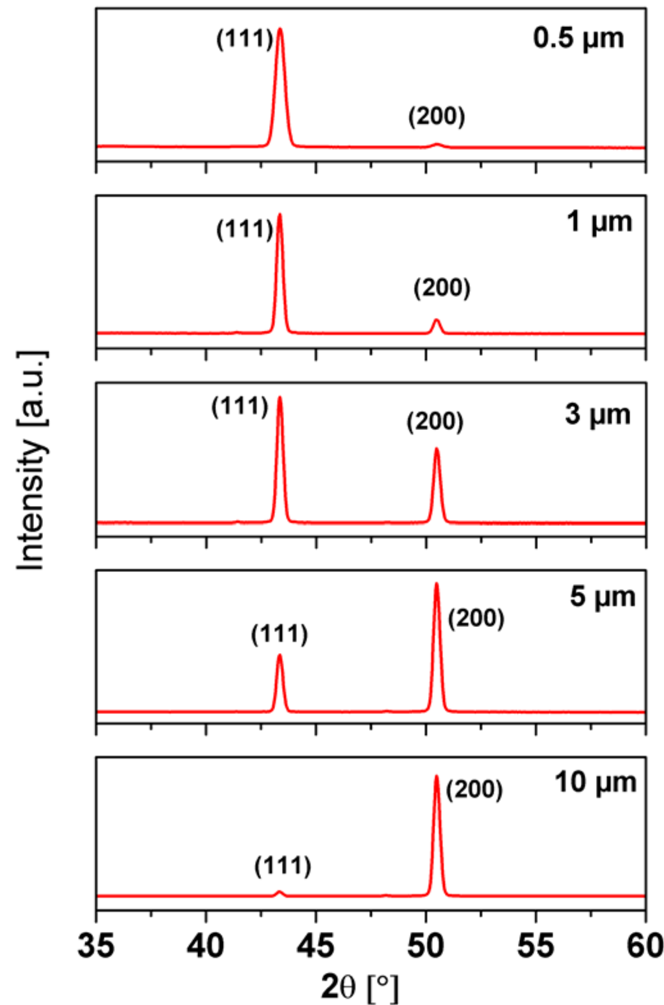

Figure 4.5: XRD *θ/2θ* scans of 0.5 to 10 µm thick Cu films after annealing at 330°C for 2 h. An increasing fraction of (100) oriented grains is found for an increased film thickness.

In Fig. 4.6b, the relative strengths of the (111) and (100) textures are plotted against the film thickness. Again a transition is found, with the cross-over now located at a film thickness between 1 and 3 µm. The standard deviation lies in the range of the symbol width. The limitations of this method will be discussed in the next section.

The volume fractions resulting from the XRD ψ measurements are shown for the different film thicknesses in Fig. 4.6c and Table 4.2. Again a cross-over in dominating texture is found at a film thickness between 3 and 5 µm. The corresponding texture

sharpness, presented by the half width at half maximum of the texture poles, is given in Table 4.2.

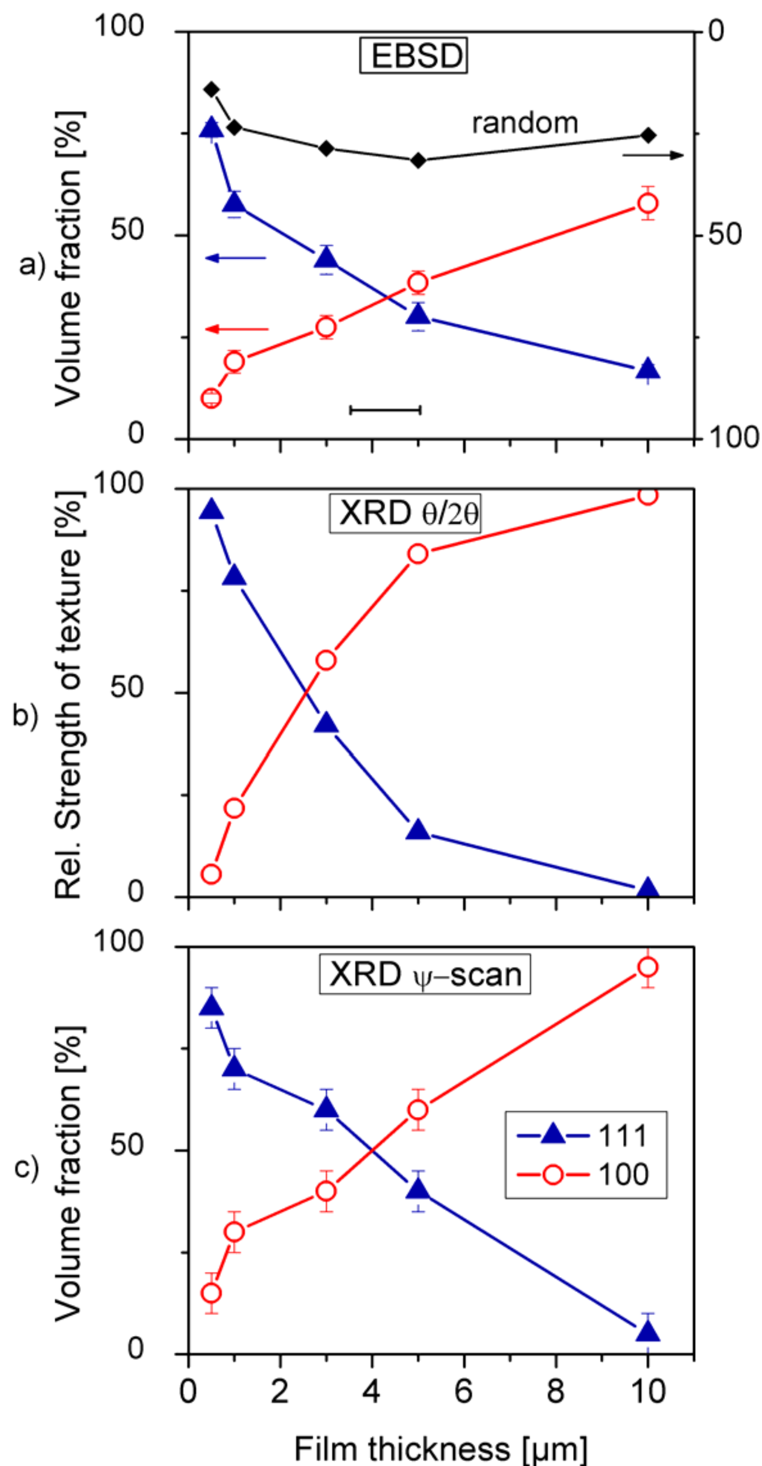

Figure 4.6: a) EBSD results: Volume fraction of (111) and (100) oriented grains as a function of film thickness. A maximum misorientation angle of 15° was allowed for assignment of orientation to each texture component. The random fraction includes all other orientations. The error bars represent the standard deviation of the measurements. If the maximum misorientation angle were changed by ± 5%, the cross-over would shift by ± 0.7 µm (see horizontal bar).b) *θ/2θ* XRD results: Texture strength as a function of film thickness. The error bar lies within the symbols. c) Results of *ψ* scans: Volume fraction of (111) and (100) oriented grains as a function of film thickness. The error is less than 5 vol%.

Tabel 4.2: Results of XRD ψ scans: V_{111} and V_{100} are the volume fractions of (111) and (100) oriented grains (error less than ± 5 vol%) , and the sharpness of the distribution is given by the half width *w* at half maximum.

Film thickness	V_{111} [%]	w_{111} [°]	V_{100} [%]	w_{100} [°]
0.5 µm	85	7	15	32
1 µm	70	8	30	15
3 µm	60	12	40	8
5 µm	40	16	60	10
10 µm	10	25	90	6

4.3.2 Grain size distribution

EBSD analyses were repeated over eight to fifteen different regions for each film thickness to obtain reliable and reproducible data. The number of grains investigated via EBSD varied from 1800 to 3200 for the different film thicknesses. The resulting grain size distributions are shown in Fig. 4.7. Both the relative and the cumulative frequency (normalized to the total number of (111) and (100) grains) of the (111) and (100) oriented grains are plotted as a function of grain size for the different film thicknesses. Separate analysis shows that the films have roughly a log-normal distribution; their median grain size increases with film thickness (Fig. 4.8). It is especially noticeable that the median grain sizes for the two texture components agree up to film thickness of 3 µm; above this value, (100) grains show increasingly larger grain sizes. Finally, the relative number of (111) and (100) oriented grains normalized to the total number of grains (including also randomly oriented grains) is shown in Fig. 4.9.

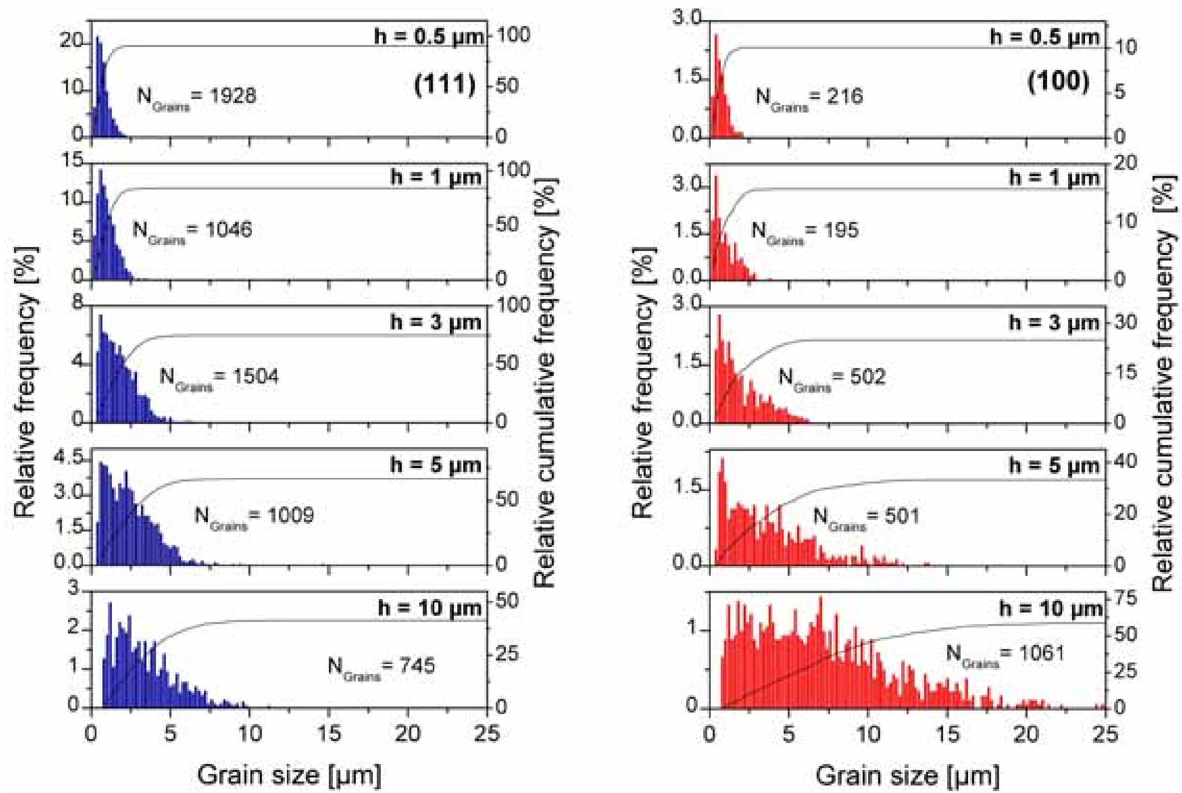

Figure 4.7: Grain size histograms and cumulative distributions for (111) and (100) oriented grains. N_{grains}, the number of grains in a particular orientation, was normalized to the sum of (111) and (100) oriented grains.

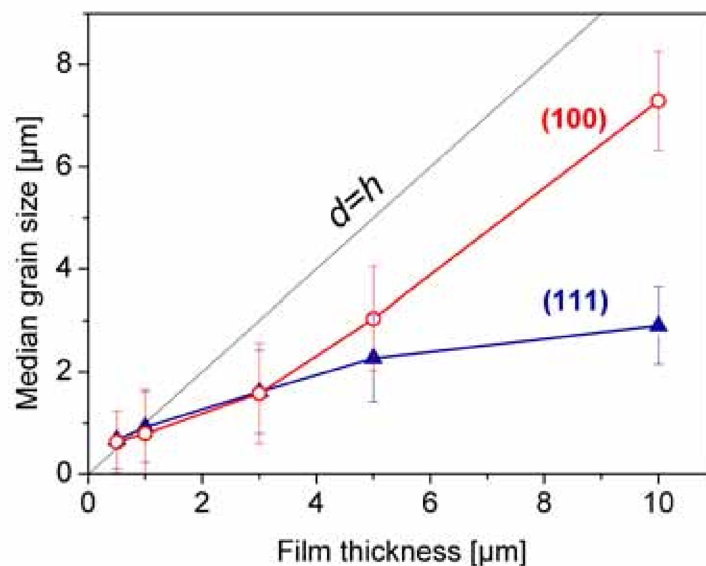

Figure 4.8: Median grain sizes for the (111) and (100) texture components as a function of film thickness. The black line corresponds to a simplified stagnation criteria [Mullins 1958].

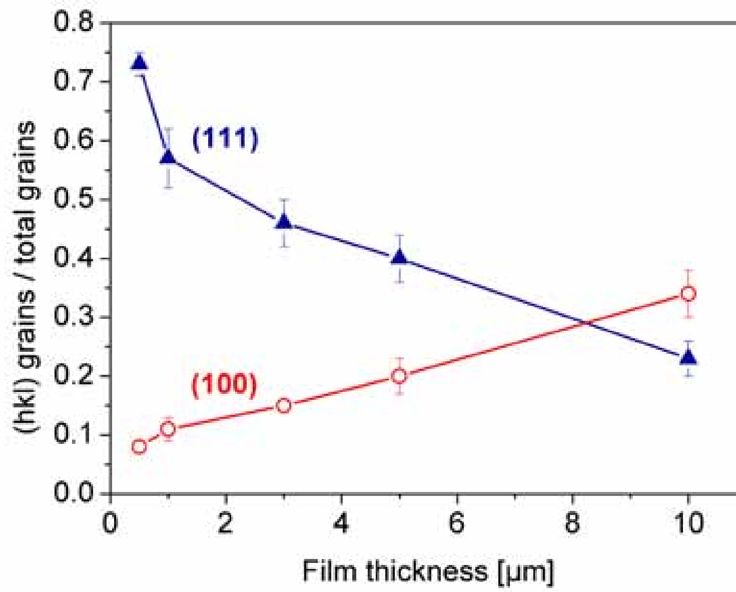

Figure 4.9: Number of (111) and (100) oriented grains normalized to the total number of detected grains as a function of film thickness. The error bars represent the standard deviation of the measurements.

4.4 Driving force map

The result of the calculations of the orientation dependent driving forces (ch. 2.2) can be shown in a "driving force map" (Fig. 4.10). The thermal expansion coefficients are α_f = 16.6 $\cdot 10^{-6}$ K^{-1} for Cu and α_s = 20$\cdot 10^{-6}$ K^{-1} for the polyimide substrate [Dupont 2008]. For Cu grains with (100) and (111) orientation, M_{hkl} is isotropic in the plane of the film and is given by M_{100} = 115 GPa and M_{111} = 261 GPa. Skriver et al. [Skiver and Rosengaard 1992] calculated the surface energies for the different orientations in Cu as 1960 mJm^{-2} for (111) and 2090 mJm^{-2} for (100) grains. There are no values available for the Cu/polyimide interface, thus the same difference of 130 mJm^{-2} as for the free surfaces was taken for calculations. For yield stress values we resort to experimental measurements. Hommel and Kraft [Hommel and Kraft 2001] have determined the yield stress of the (111) and (100) texture component of Cu films on polyimide substrates for film thicknesses between 0.4 and 3.15 µm. Assuming the validity of the Von Blanckenhagen model [Von Blanckenhagen 2002], the experimental yield stress values were fitted by the following $\ln(h)/h$ –functions:

$$\sigma_{y,111} = 7.49 \cdot \frac{\ln\left(\frac{h}{2.56 \cdot 10^{-10}}\right)}{h} + 164.2 \cdot 10^{6} \quad (4.1)$$

$$\sigma_{y,100} = 8.55 \cdot \frac{\ln\left(\frac{h}{2.56 \cdot 10^{-10}}\right)}{h} + 21.21 \cdot 10^{6} \quad (4.2)$$

where $\sigma_{y,111}$ and $\sigma_{y,100}$ are given in Pa and h is expressed in meter. An equivalent fit would result using the Nix-Freund model [Nix 1989, Freund 1990].

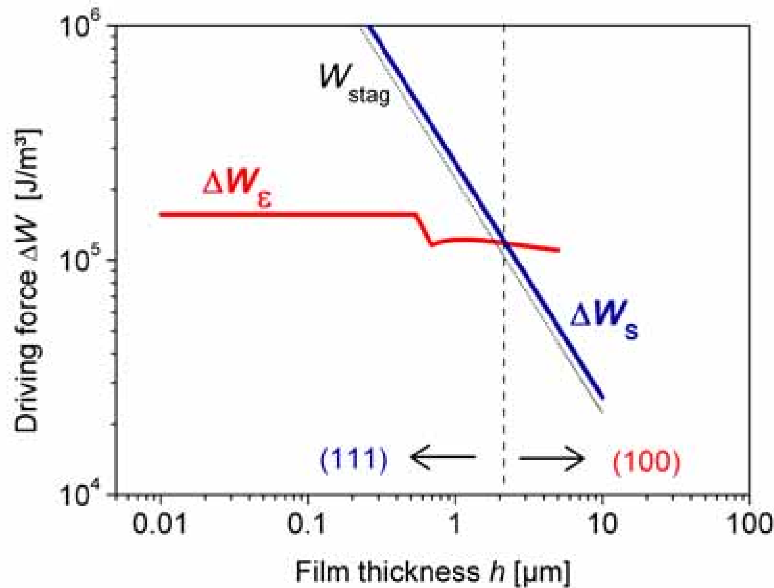

Figure 4.10: Driving force map: Estimated driving force for strain energy minimization, ΔW_ε, and surface/interface energy minimization, ΔW_s, for Cu thin films on polyimide. Surface and interface energy minimization (111 texture) dominates below a film thickness of h = 2.2 µm while strain energy minimization (100 texture) dominates above this value. The stagnation force due to grain-boundary grooves is shown by a black dotted line.

The blue curve (ΔW_s) represents the driving force due to surface/interface energy minimization; it scales inversely with film thickness. The red curve marks the difference in thermal strain energy ΔW_ε between (111) and (100) textured grains for a temperature difference ΔT = 305 K. It is seen that ΔW_ε is constant for small film thicknesses; this is the fully elastic case (eq. 1.17). The end of the elastic regime is reached first for the (111) orientation at a film thickness of 0.5 µm. The elastic driving

force then drops according to eq. 1.18. At a film thickness of 0.7 µm, the yield stress is also exceeded in the (100) grains and the driving force reaches a lower level (eq. 1.19). In this region (fully plastic), the curve is determined by the difference in yield stresses between the (111) and (100) orientation. The “cross over” in driving forces occurs at a film thickness of about 2.2 µm (dashed vertical line), indicating the energetic preference of the (111) texture for film thicknesses smaller than this critical value and of a (100) texture for larger film thicknesses. Finally, also the stagnation force due to grain-boundary grooves is shown in Fig. 4.10 by a black dotted line; it also scales inversely with film thickness.

4.5 Discussion

We first direct attention to a comparison of the different analytical methods employed in this study. EBSD is a powerful tool for microtextural analysis: it has the advantage of giving access to all orientations and allows the direct determination of volume fractions. In particular, also information about the microstructure is included in the data. The analysis of the results revealed a broad texture transition from a dominating (111) to a (100) texture with increasing film thickness (Fig. 4.6a). Similar results were obtained by XRD measurements, especially when using ψ scans (Fig. 4.6c): the value for the cross-over in dominating texture is almost identical.

The discrepancy in the total values of volume fractions to the EBSD results, and particularly its increase for thicker films, can most likely be attributed to the role of the random fraction. Whereas the random fraction is explicitly considered in the EBSD analysis, it is neglected in XRD. Okolo et al. [Okolo *et al.* 2005] demonstrated for Cu films on SiO_2 and Si_3N_4 substrates that pole figure scans do not show unambiguously either the presence or absence of a random fraction; fits of the same quality are possible to ψ scans independent of whether a random fraction is assumed or not. By considering the random fraction (determined by the EBSD measurements in calculating the (111) and (100) volume fraction), excellent agreement between the results of the EBSD and XRD ψ method is reached (Fig.4.11).

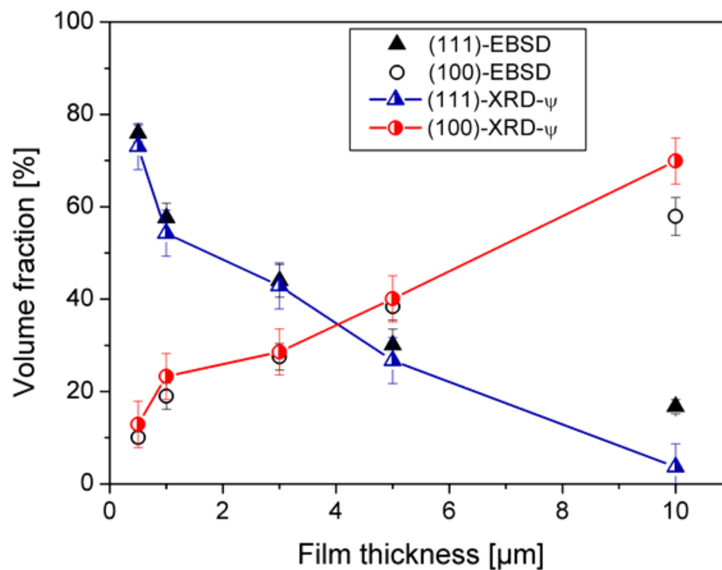

Figure 4.11: Comparison of results of EBSD measurements and XRD ψ scans. The random fraction determined by EBSD measurements is considered for the XRD results.

The difference in volume fractions between the two methods lies even within the standard deviation of the XRD ψ results for film thicknesses from 0.5 to 5 µm. On the other hand, it is not possible to reach such an agreement with the $\theta/2\theta$ results. A possible explanation lies in the fact that only planes parallel to the surface are detected and, consequently, these scans are unable to detect an increase in volume fraction due to an increased width of the texture. The width of the (111) texture increases for thicker films (Table 4.2) while that for the (100) texture decreases; hence the $\theta/2\theta$ method tends to underestimate the (111) volume fraction and to overestimate the (100) fraction for thicker films. Furthermore, the $\theta/2\theta$ scans do not have access to all crystal orientations, e.g. the (511) reflection is not available for these measurements with Cu K_α radiation. Thus, it is difficult to define a possible random fraction. But the $\theta/2\theta$ scans do provide a quick method for preliminary texture information.

Also the EBSD and the XRD ψ scans have their limitations. The EBSD method is not volume-related, as the penetration depth lies in the range of several tens of nm. Consequently, the assumption of a columnar grain structure is necessary to obtain the volume fraction of a texture component. And although a predominantly columnar structure was found on cross-sections produced by the focussed ion beam, variations in the grain structure, especially for the thicker films, do occur. Furthermore, the

measuring area for EBSD measurements is much smaller than for XRD scans. While EBSD samples an area in the range of 10^2 to 10^4 µm², XRD collects data from an area of several mm² and is volume-related due to its penetration depth.

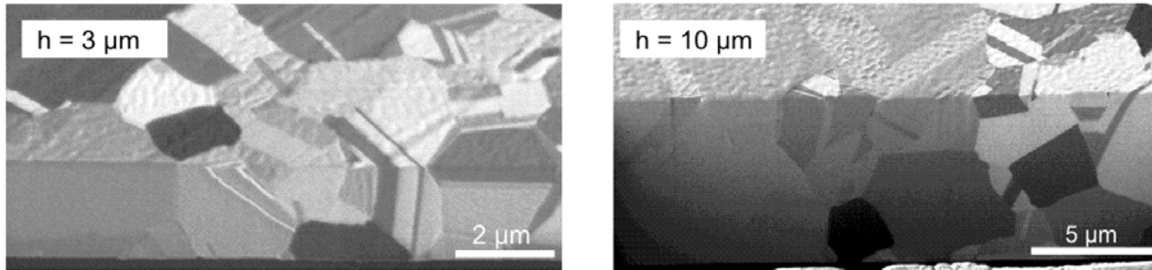

Figure 4.12: FIB cross sections of 3 and 10 µm thick Cu films. The films were annealed at 330°C for 30 min after deposition.

One of the main benefits of the EBSD method is that it provides detailed insight into grain size statistics (Figs. 4.6 to 4.9). It is apparent from Figure 4.6 that the differences in the grain size distribution between the two texture components increase for larger film thicknesses. Analysis shows that the standard deviation of the near-log-normal distributions are very similar, while the difference in median grain sizes increases for thicker films. Thus, the development of the median grain size (Fig. 4.8) as well as of grain number (Fig. 4.9) is texture-specific. It is interesting that the median grain sizes for (100) and (111) grains coincide up to a film thickness of about 3 µm; this is at first sight surprising as the (111) orientation is energetically favoured for small thickness. The explanation may lie in the vicinity to the stagnation criterion, drawn as *d*=*h* in Figure 4.5, which impedes boundary motion even for (111) grains. Above a film thickness of 3 µm, the median grain sizes diverge. Now the (100) grains are energetically favoured and grow until they approach the stagnation limit. The unfavourable (111) grains reach a lower saturation size. The dominance of the (111) texture in thin films is therefore not due to the larger grain size, but to their much larger number (Fig. 4.9). In thicker films, the grain numbers seem to converge for the two orientations; the dominance of the (100) texture can now be attributed to their larger size.

An important observation in Fig. 4.9 is the fact that the difference in grain numbers between the two texture components is much larger for the thin films than for the thick ones. This behavior can be explained with reference to Fig. 4.10: the (111) component in thick films has a much larger driving force advantage (of order

10^6 J/m³) than the (100) component in thicker films (of order 10^5 J/m³). This again confirms the good correspondence between the experimental results and the energetic interpretation.

This also applies to the cross-over in driving forces and therefore to the point of texture transition, which is predicted to occur at a film thickness of about 2 µm (Fig. 4.10). Nevertheless, there is a difference to the experimentally observed texture transition at a film thickness of 4.2 µm. But as the assumed yield stresses enter in a sensitive way (eq. 1.19), a difference of only 20 % between (111) and (100) oriented grains would cause a shift in the cross-over point to 4 µm as observed experimentally. Therefore the agreement between experiment and theory is satisfactory.

A significant observation which cannot be explained by a purely energetic argument is the broad texture transition. The reason for this behaviour must lie in the kinetics of texture evolution which will also depend on the details of the microstructure: grain neighbour interactions or local stagnation conditions can possibly lead to a "sluggish" transition. Such an effect could be accessible by numerical simulation of grain-boundary motion, e.g. as in Carel et al. [Carel *et al.* 1996]. But also *in situ* grain growth experiments give some deeper insight into mechanisms responsible for grain growth in these films (ch. 6).

4.6 Summary

1. Electron backscatter diffraction (EBSD) microtexture measurements of Cu thin films on polyimide substrates revealed a texture transition from (111) to (100) at film thicknesses between 3 and 5 µm. With the EBSD technique, the dominating texture component and the grain size distributions were successfully determined.

2. Detailed comparison with results based on X-ray diffraction (XRD), using both $\theta/2\theta$ and ψ scans, was made. Considering the random fraction accessible only by EBSD measurements, the XRD ψ scan results are in good agreement with EBSD data.

3. The analysis of microtexture by EBSD has provided valuable additional insight. The grain size distributions for the (111) and (100) oriented grains show an increasing difference of the median grain size with increasing film thickness. This is explained by a decreasing role of the stagnation force due to grain-boundary grooves.

4. In contrast to theoretical predictions, the texture transition is not abrupt but a continuous change from a dominating (111) to (100) texture component is observed. The random component increases with film thickness but remains below 25 %.

5. The experimental findings can be explained by the texture-evolution model of Thompson and Carel [Thompson and Carel 1996a, Thompson and Carel 1996c]. A mapping of the driving forces for strain energy and surface/interface energy minimization predicts a texture transition at a similar film thickness as in the experiments.

Chapter 5 Effect of Uniaxial Stress on Texture Evolution

5.1 Introduction

The growth of grains with preferred orientations causing texture evolution in thin films is driven by energy minimization. Anisotropic energies such as surface, interface and strain energy result in an orientation-dependent driving force on the grain boundaries determining the resulting texture. Thompson and Carel [Thompson and Carel 1996a] developed a texture evolution model by comparing the orientation-dependent driving forces.

As the driving force for surface/interface energy minimization scales inversely with the film thickness, and the driving force for strain energy minimization is determined by the elastic strain, different textures are expected for varying film thickness and stress state [Thompson and Carel 1996c]. In this chapter we adopt the Thompson-Carel approach and modify it for the case of uniaxial stress. Doing so, the

modified approach predicts preferred (100) grain growth above a critical strain level. Parts of the theoretical estimate by Sonnweber-Ribic, Dehm, Gruber and Arzt have been published [Sonnweber-Ribic *et al.* 2006a]. Tensile tests with maximum strains even higher than this critical value were carried out to validate this theory.

5.2 Theoretical Predictions

The calculation of the driving forces for the biaxial stress state is described in chapter 2 – now we consider a uniaxial stress state and modify the equations accordingly. While there is no change for the driving force due to surface and interface energy minimization, several modifications have to be introduced for the strain energy minimization.

5.2.1 Strain energy minimization – uniaxial stress

The strain energy density of an (hkl) oriented grain under uniaxial stress is (see Appendix 8.1.2):

$$U_\varepsilon = \frac{1}{2} E_{hkl} \cdot \varepsilon_u^{\ 2}, \tag{5.1}$$

where ε_u is the strain parallel to the applied stress and E_{hkl} is the orientation-dependent Young's modulus.

After reaching the yield stress, the strain energy density is limited to the value

$$U_\varepsilon = \frac{1}{2} \frac{\sigma_{y,hkl}^{\ 2}}{E_{hkl}} \tag{5.2}$$

where $\sigma_{y,hkl}$ is the yield strength of the specific orientation (hkl). Similar to chapter 4, the experimental yield stress values as determined by Hommel and Kraft [Hommel and Kraft 2001] are used for the calculations.

Using equations (5.1) for the elastic case, the difference in strain energy density between two neighbouring grains with orientation (111) and (100) is

$$\Delta U_{\varepsilon} = \frac{1}{2}(E_{111} - E_{100})\varepsilon^2 \quad \text{(all elastic).} \tag{5.3}$$

This corresponds to the driving force available for grain boundary motion. The driving force increases parabolically with strain until one orientation starts to yield. For this case the strain energy density of the plastically deforming grains remains constant, but the strain energy density of the other orientation can still increase. The total driving force still increases according to

$$\Delta U_{\varepsilon} = \frac{1}{2}E_{111}\varepsilon^2 - \frac{1}{2}\frac{\sigma_{y,100}^{\;2}}{E_{100}} \quad \text{(100 plastic).} \tag{5.4}$$

This behaviour continues until the (111) oriented grains start to yield as well. Then the strain energy density difference becomes:

$$\Delta U_{\varepsilon} = \frac{1}{2}\frac{\sigma_{y,111}^{\;2}}{E_{111}} - \frac{1}{2}\frac{\sigma_{y,100}^{\;2}}{E_{100}} \quad \text{(fully plastic).} \tag{5.5}$$

These equations are used to estimate the driving forces due to surface/interface energy minimization and strain energy minimization for a 3 µm thick Cu film. The results are shown in Fig. 5.1.

For Cu grains with (111) orientation, the elastic modulus is isotropic in the film plane and is given by E_{111} = 130 GPa. For a (100) oriented grain the Young's modulus is not isotropic, but varies between 67 GPa and 130 GPa (Fig. 5.2). The mean value for all possible orientations within the film plane is E_{100} = 93 GPa.

Again, similar to the considerations for the biaxial stress state, the comparison of the driving forces is used to predict the energetically favoured grain orientation. While surface energy minimization dominates the texture evolution below a strain of 0.12 ± 0.02 %, the strain energy minimization prevails for higher strains; this is again connected with an energetic advantage of the (100) oriented grains.

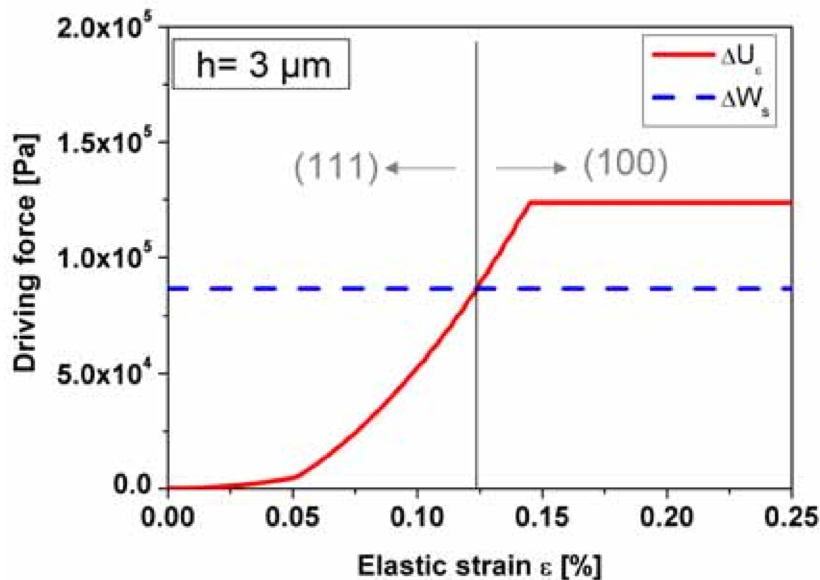

Figure 5.1: Driving forces for strain energy minimization ΔU_ε and surface/interface energy minimization ΔW_s for a 3 µm thick Cu film on polyimide under uniaxial stress. There is a cross-over in driving forces: above a total strain of ε = 0.12±0.02% the strain energy minimization dominates.

Thus, assuming sufficient grain boundary mobility, the growth of (100) oriented grains should be observed when a strain of more than 0.12 ± 0.02 % is applied to a 3 µm thick film.

To estimate the accuracy of this strain level, the entering parameters have to be considered. For the calculation of the strain energy density, yield stresses enter in a sensitive way. For yield stress values we resort to experimental measurements, which have been conducted by Hommel and Kraft [Hommel and Kraft 2001] for 0.4 to 3.15 µm thick Cu films. An error of ±10% for the yield stresses would cause a shift of the cross-over of ±0.005%. On the other hand, the error in interface energy is assumed to have a higher effect. There are no values available for the Cu/polyimide interface, thus the same difference of 130 mJm^{-2} as for the free surface was taken for the calculations. A deviation of 50% would lead to a change in critical strain of 0.015%. Using these estimates, the total deviation of the critical strain is estimated to ±0.02%

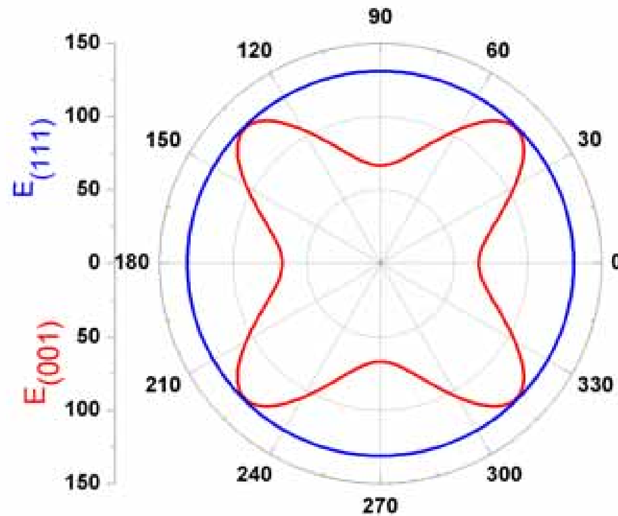

Figure 5.2: Young's modulus in the (111) and (100) plane of Cu. While the Young's modulus is isotropic in the (111) plane, it is a function of the in-plane angle in the (100) plane.

5.3 Experimental

99.996 at% pure Cu films were deposited on 125 µm thick polyimide substrates (Kapton®, DuPont) using a UHV magnetron sputtering system (DCA Instruments). The thickness of the Cu layers was 3 µm. Film deposition was performed at nominally room temperature using a base pressure of 10^{-8} Pa and a deposition rate of 28 nm/min. In order to carry out *in situ* tensile tests, the substrates were cut into a dog-bone shape (Fig. 5.3). The polyimide foil can be deformed elastically to strains of more than 3%.

Important microstructural changes occur often at elevated temperatures and/or during deformation. Nevertheless, most investigations in literature were carried out after heat or deformation treatment – examining just the initial and final microstructure. Therefore an experimental setup providing the opportunity to observe these changes *in situ* was developed.

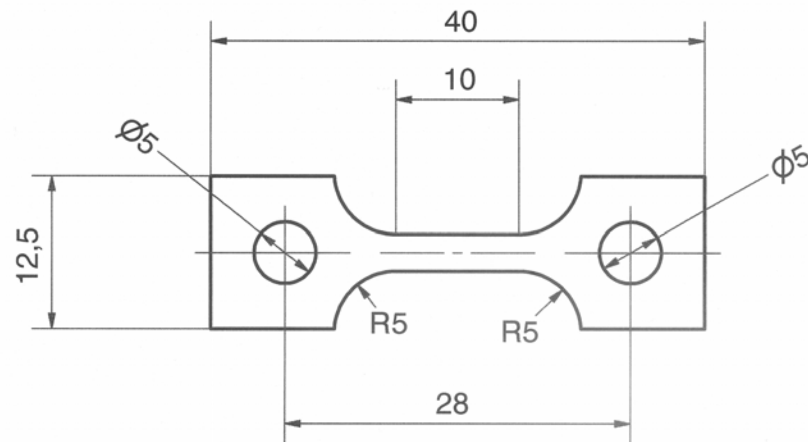

Figure 5.3: Dog-bone shape of the polyimide substrates.

Tensile testing and annealing was carried out inside a Leo 1530-VP SEM equipped with a heating and tensile testing device. In this set-up, which was developed at the Max Planck Institute for Metals Research, the samples are oriented at 70° to the electron beam, as it is required for the EBSD measurements.

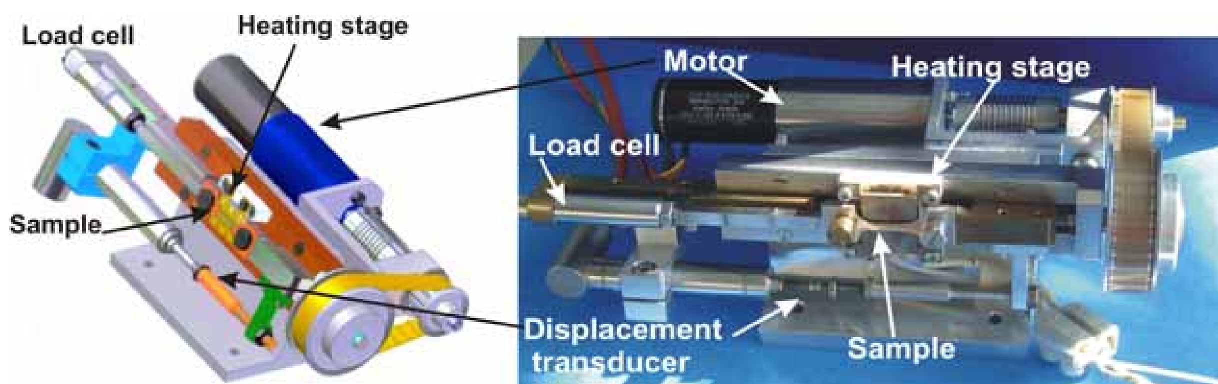

Figure 5.4: *In situ* tensile testing and heating appliance.

With this setup, deformation and/or heating experiments and EBSD investigations were carried out simultaneously.

The general construction of the *in situ* tensile testing and heating appliance is shown in Fig. 5.4 and contains three basic components. The main body consists of steel and includes the sample holder, the load cell and the displacement transducer. The load cell has a testing range of ±200 N and an accuracy of 0.2 N. It is connected to the main part with the help of two internal threads. The displacement transducer

allows the measurement of the sample elongation and has a testing range of 10 mm and an accurancy of 2 µm.

The second component is the motor and the gears which are needed to drive the crossheads. They are arranged behind the main part in order to allow a compact and spacesaving design. The heating stage consists of a tungsten wire embedded between a ceramic isolator and a Cu sheet. It is heated resistively to temperatures as high as 250 °C. The maximum sample temperature which is heated by radiation is 143°C.

5.3 Results

In order to validate the preferred growth of (100) oriented grain above an elastic strain of 0.12 %, several *in situ* tensile tests were carried out inside the SEM. EBSD maps were made before and after deformation in order to observe microstructural changes.

For the first experiment, a 3 µm thick Cu film annealed at 330°C in vacuum for 2 h was used. Prior to the tensile test, small arrays of grains were defined with the help of a FIB in order to focus on specific (100)-(111) grain boundaries and minimize grain interactions form above and below (Fig.5.5). Two small cuts were made with the help of the focused Ga beam. In order to minimize surface damage through the energy of the Ga ions, these cuts were made very sensitively and only low Ion beam currents were used. EBSD measurements were made in non-radiated and irradiated areas but no considerable differences were observed.

In the next step, a uniaxial strain of 1 % was applied at room temperature. EBSD maps of the strained microstructure were taken 23 and 73 h later on. The results are shown in Fig. 5.5.

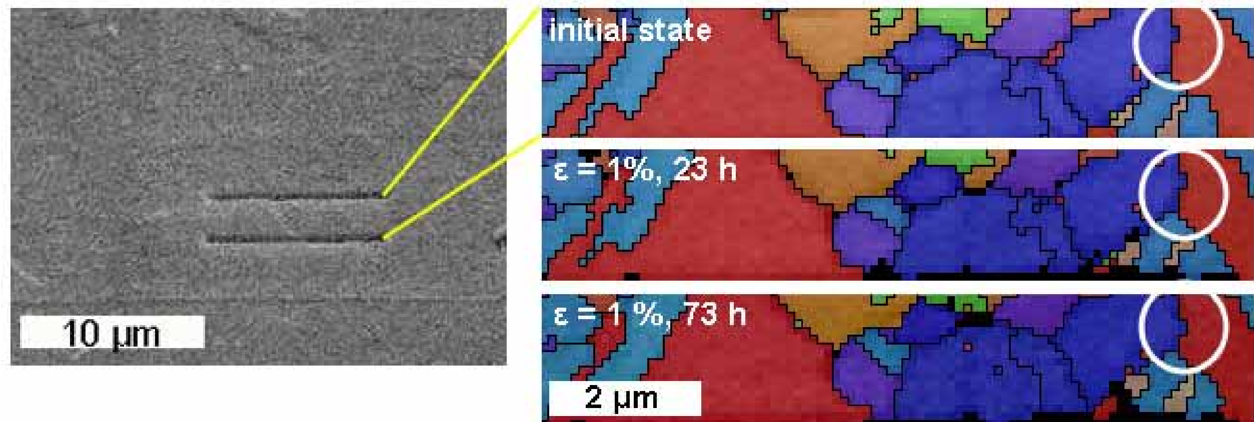

Figure 5.5 left: SEM image of 3 µm thick Cu film with two cuts; right: EBSD maps (step size: 100 nm) of the predefined area. Prior to the experiment, the sample was annealed at 330°C for 2 hours. The highlighted area (white circle) shows the grain boundary between a blue (111) grain and a red (100) oriented grain. No grain boundary motion is detected during the experiment.

In a further experiment the temperature was increased to 143 °C. The schematic course of this experiment as well as the point of time for the four EBSD maps is shown in Fig. 5.6. The corresponding EBSD maps are given in Fig. 5.7.

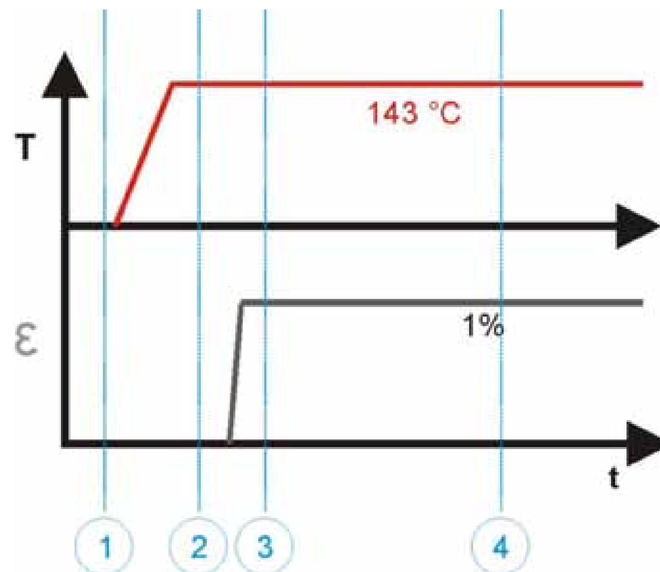

Figure 5.6: Schematic course of the tensile test at 143°C. The vertical lines show thepoints of time, when EBSD maps were made.

Similar experiments were performed using as-deposited 3 µm thick Cu films. First, for comparison, an unstrained sample was annealed at 104°C. EBSD measurements were carried out in hourly intervals to investigate the grain growth. After about 9 hours the intervals were increased as the microstructural changes became small. The same procedure was carried out for samples which were

uniaxially strained to 0.8 and 1% at 104°C. The final microstructures are shown in Fig. 5.8. The final fraction of (100) oriented grains is 26.7, 30.9 and 28.9% for the unstrained sample, and samples with 0.8% and 1% strain, respectively. As the additional driving force is assumed to increase the growth rate of the (100) grains, the increase in mean grain size is represented in Fig. 5.9.

The initially linear grain growth rates are marked in Fig. 5.9 and their values are summarized in Tab. 5.1.

Tabel 5.1: Initial grain growth rate [nm/h] for unstrained and uniaxially strained samples.

unstrained	strained to 0.8 %	strained to 1%
230 ± 32	261 ± 33	229 ± 30

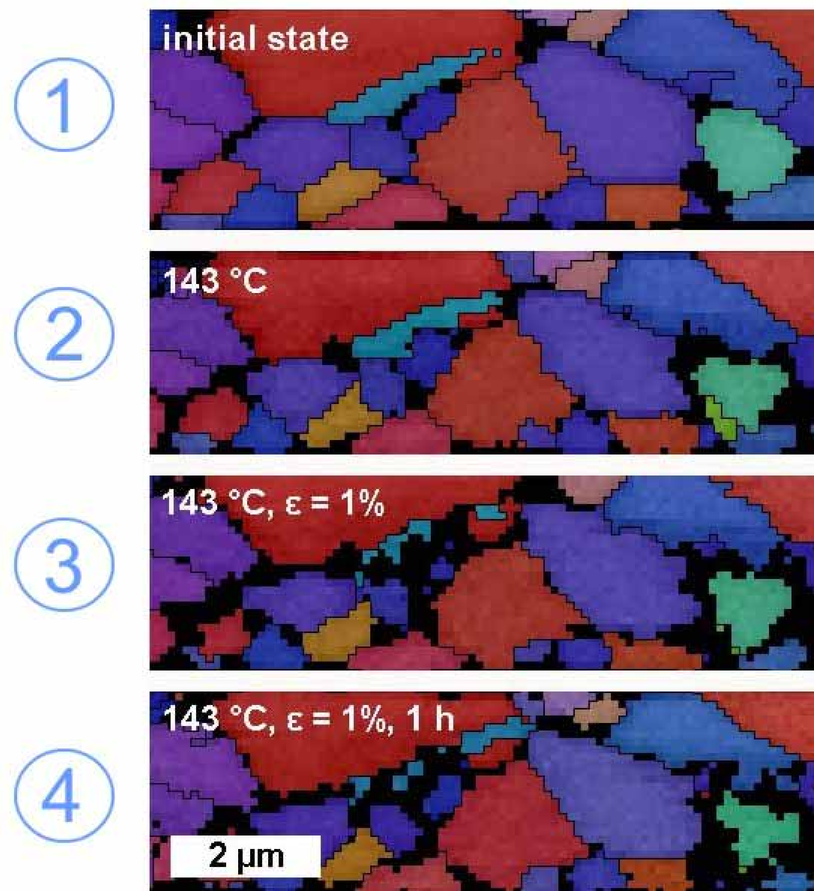

Figure 5.7: EBSD maps (step size: 100nm) of a 3 µm thick Cu film. First the temperature was increased to 143 °C and then a uniaxial strain of 1% was applied to the sample. In the center of the maps, a grain boundary between a (111) and (100) grain can be observed. No grain boundary motion is found during the experiment. Black colour represents non-indexed points.

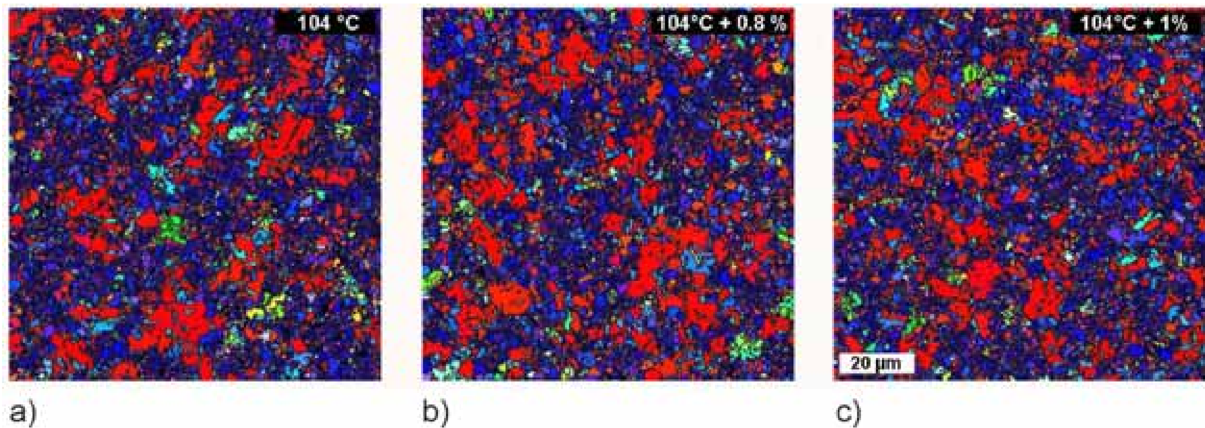

Figure 5.8: EBSD-maps of 3 µm thick Cu films tested at 104 °C subjected to different treatments: a) unstrained, b) 0.8 % uniaxially strained sample, c) 1% uniaxially strained sample. Final fractions of (100) oriented grains of a) 26.7, b) 30.9 and c) 28.9% were observed.

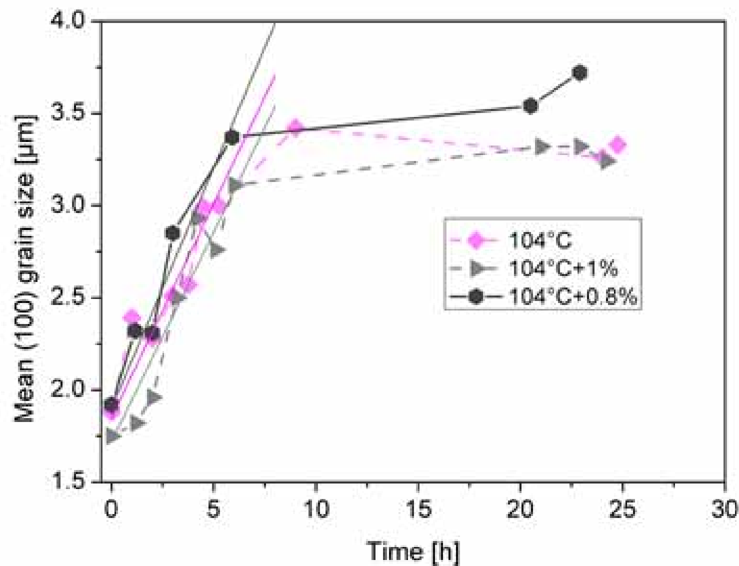

Figure 5.9: Mean grain size as a function of time during annealing at 104°C. The pink points show the results of the unstrained sample, whereas the grey and black symbols represent the results of the strained samples.

5.4 Discussion

During the first tensile test, a strain of 1% was applied to a 3 µm thick film – but, in contrast to theoretical predictions, no growth of the (100) oriented grain was observed (Fig. 5.5). An estimate of the grain growth velocity is expected to give an explanation for this result. Vandermeer et al. [Vandermeer *et al.* 1997] measured a mobility of $6.31 \cdot 10^{-16}$ m^4/Js at 121°C when analysing the recrystallization of cold-

deformed Cu. Using the known activation energy of 0.62 eV/atom (Donthu *et al.* 2003) and the mobility measured by Vandermeer, the preexponential factor M_0 is determined (eq. 1.3) to $5.38\cdot10^{-8}$ m^4/Js. Now it is possible to extrapolate the mobility at room temperature to $M_{RT} = 1.27\cdot10^{-18}$ m^4/Js. The applied total strain of 1 % lied far above the estimated critical elastic strain of 0.12 %. Nevertheless, the maximum driving force due to strain energy minimization cannot overcome $1.24\cdot10^5$ J/m³ (Fig. 5.2), as only the elastic strain is assumed to contribute to strain energy. Thus, the rate of grain growth at room temperature is calculated to be 0.570 nm/h (eq. 1.1). That means that a (100) oriented grain is expected to move 41 nm in 73 hours (Fig.5.5). As the step size of the EBSD-measurements is 100 nm, such a motion is hardly detected – giving a possible explanation for the absence of (100) grain boundary motion.

In order to increase the mobility and reduce the measuring time, the next experiment was carried out at an elevated temperature of 143 °C. The corresponding grain boundary mobility can be estimated to $M_{143} = 1.66\cdot10^{-15}$ m^4/Js. This increase in mobility drives the grain growth rate to 740 nm/h, a value which should be easily detectable by EBSD-measurements. But again, no microstructural changes towards a more pronounced (100) texture were found (Fig. 5.7) after one hour. The increasing amount of non-indexed points (marked black in Fig. 5.7) can be attributed to increasing carbon contamination of the scanned area with repeated scanning. In order to exclude this carbon contamination to be responsible for the stagnation of grain growth, a “fresh” area was analysed after deformation. But again, no increase in (100) texture fraction was revealed.

An alternative explanation for the absence of any grain boundary motion could be a stagnation force (eq. 1.20), which pins the grain boundaries. As the samples were annealed at 330°C prior to the tensile tests, this stagnation force may have been induced by thermal grooves formed during annealing.

Therefore, the following experiments were carried out with as-deposited (not annealed) 3 µm thick films. A first test, carried out with a uniaxial unstrained sample at 104°C, shows abnormal (100) grain growth, accompanied by a texture change towards a dominant (100) texture (Fig. 5.8a). In a next step, analogous experiments were carried out with uniaxially strained samples at total strains of 0.8 and 1% (Fig. 5.8 b and c). Again abnormal (100) grain growth was observed. The final (100) volume fractions were 26.7, 28.9 and 30.9%, which is not considered as statistically

significant variation. Also the mean (100) grain size evolution with time does not reveal clear differences (Fig. 5.9 and Tab. 5.1). This is again contradictory to the expectation that the applied strain should have enhanced grain boundary velocity. An explanation for this may results from a closer look into the driving forces.

1. Annealing experiment at 104°C (uniaxially unstrained):

For a 3 µm thick Cu film the driving force for surface energy minimization $\Delta\gamma/h$ can be estimated to $8.7\cdot10^4 \pm 2.2\cdot10^4$ Pa (ch. 4.4, eq. 1.7). The error originates from an accepted deviation of 50% for the Cu/polyimide interface energy difference. On the other hand, the biaxial strain energy minimizing driving force ΔW_ε due to the increase in temperature to 104°C is about $1.2\cdot10^4 \pm 0.3\cdot10^4$ Pa (eq. 1.17, tab. 3.2). This estimate indicates the dominance of the surface energy associated with the preferred growth of (111) oriented grains. In contrast, abnormal growth of (100) oriented grains was found. Even, when the interface energy difference is totally neglected ($\Delta\gamma_i = 0$), ΔW_s still exceeds ΔW_ε .

2. Tensile test at 104 °C

Now the strain energy is increased as an uniaxially strain is applied to the sample. A strain energy minimizing driving force $\Delta U_\varepsilon = 1.24\cdot10^5 \pm 0.25\cdot10^5$ Pa was calculated (see Fig. 5.2 – maximum strain energy minimizing driving force). This strain energy alone already exceeds the driving force for surface energy minimization $\Delta\gamma/h$. This dominance can give an explanation for the preferred growth of (100) oriented grains.

Nevertheless, as no differences either in the final amount of (100) texture or in the growth velocity of the (100) grains for the uniaxial strained and unstrained samples were found, there are even more questions which have to be answered. The main question is why a uniaxial strain does not have any effect on grain growth kinetics. Wikström and Nyårds [Wikström and Nygards 2002] simulated the effective behaviour of columnar grained textured Cu thin films under tensile loading within a continuum framework. Polyimide was used as a substrate. They found the mean stress in the (111) and (100) grains to be quite similar when subjected to small tensile loading – therefore reducing the strain energy minimizing driving force. Their results implied that the strain energy driving force due to a tensile load is significantly

reduced. While this assumption allows to explain why there is no difference between strained and unstrained samples, no explanation for the abnormal (100) grain growth is given.

As strain energy density due to thermal mismatch or uniaxially loading is excluded as dominant driving force, another driving force has to be responsible for the preferred growth of (100) oriented grains. A possible alternative driving force can result from the defect density in the as-deposited grains.

In order to get more information about grain growth kinetics, systematic *in situ* measurements were made. The results are presented in the following section.

5.5 Summary

1) The theoretical comparison of driving forces for a 3 μm thick Cu films in the case of a uniaxial stress state revealed a dominant strain energy minimization above a strain of 0.12%. Therefore (100) grains were expected to grow when applying an elastic strain of more than 0.12%.
2) In contrast to these theoretical predictions, a tensile test to a total strain of 1%, carried out at room temperature, revealed no (100) grain growth.
3) A tensile test to 1%, carried out at 143°C, again showed no (100) grain growth.
4) Abnormal grain growth of (100) oriented grains was observed for 3 μm thick, as-deposited, Cu films annealed at 104°C. But further uniaxial stress resulted in no difference, neither in grain growth velocity nor in the final (100) texture fraction.
5) Purely energetic considerations cannot explain these results. In order to get additional insight, a systematic study on abnormal grain growth has to be carried out. The influence of film thickness and temperature on grain growth kinetics may include additional information about basic mechanisms.

Chapter 6 *In situ* Grain Growth Experiments - Effect of Temperature and Film Thickness on Grain Growth Kinetics

6.1 Introduction

As purely energetic considerations, made in chapters 4 and 5, can neither explain the lack of grain growth for annealed Cu films nor the characteristics of abnormal grain growth in as-deposited films, *in situ* annealing experiments were carried out. These systematic experiments were carried out to get more information about kinetics and basic mechanisms.

In this section we follow the abnormal growth of individual (100) oriented grains in 1 to 5 μm thick films for more than 24 hours at temperatures between 90 and 118°C. The EBSD data are then used to interpret the dynamics and kinetics of

grain growth processes, leading to conclusions that would be unreachable without *in situ* capacity.

6.2 In situ experiments

Growth of abnormal (100) grains in these Cu films was investigated at three different annealing temperatures. Annealing was carried out inside the Leo 1530-VP SEM equipped with a heating facility. During the experiments the specimens were heated up to temperatures of 90, 104 or 118°C, all high enough to induce grain growth processes. After reaching the pre-defined temperature, grain growth was recorded by hourly EBSD (HKL/Channel5) measurements. After about 10 hours the intervals between EBSD measurements were increased, and terminated after about 27 hours. For the *in situ* tests, areas of 300x300 steps were scanned repeatedly at step intervals of 0.1 to 0.5 µm. Approximate duration of each scan was 43 min. In order to analyse the initial, as-deposited, small grained microstructure, scans with a smaller step size (50 nm) were carried out prior to annealing.

6.3 Results

6.3.1 As-deposited microstructure and microtexture

Figure 6.1 shows the EBSD orientation maps of the as-deposited Cu films for the film thicknesses from 1 to 5 µm. Grains are colour coded in the following way: “blue” corresponds to grains oriented with the (111) plane parallel to the surface, while (100) oriented grains are marked “red” and (110) grains in “green” (see orientation colour key). The initial structure consisted of a homogeneous microstructure with a preponderance of the (111) orientation (Fig. 6.1). Also (100) oriented grains were present, but abnormally large (100) grains were absent. Below, the texture information is summarized in inverse pole figures, revealing again the dominant (111) texture for all different film thicknesses. The intensity colour scale is shown with units of times random, the ratio of the measured volume fraction over the calculated random probability of this orientation. Fig. 6.2 presents the (111) and (100)

volume fractions as a function of film thickness. A slight decrease in (111) texture component, was found with increasing film thickness. The fraction of (100) oriented grains remained roughly constant at about 5 to 7% for all film thicknesses.

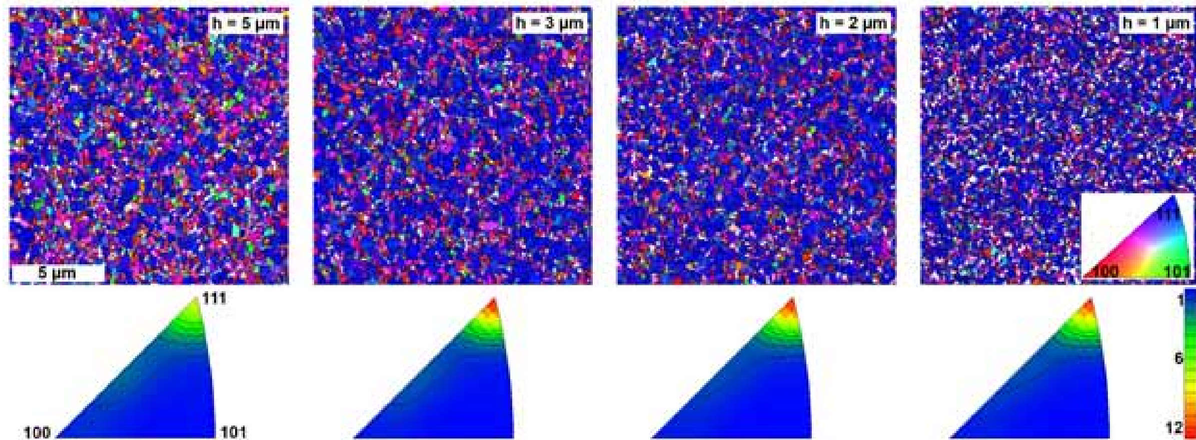

Figure 6.1: EBSD orientation maps and inverse pole figures of Cu films on polyimide showing the initial as-deposited texture for different film thicknesses: 1, 2, 3 and 5 µm. In the EBSD maps the orientation normal to the film surface is represented with the help of the orientation colour key. In the pole figures, the populations are measured in units of times random, the ratio of the measured volume fraction over the calculated random probability of this orientation.

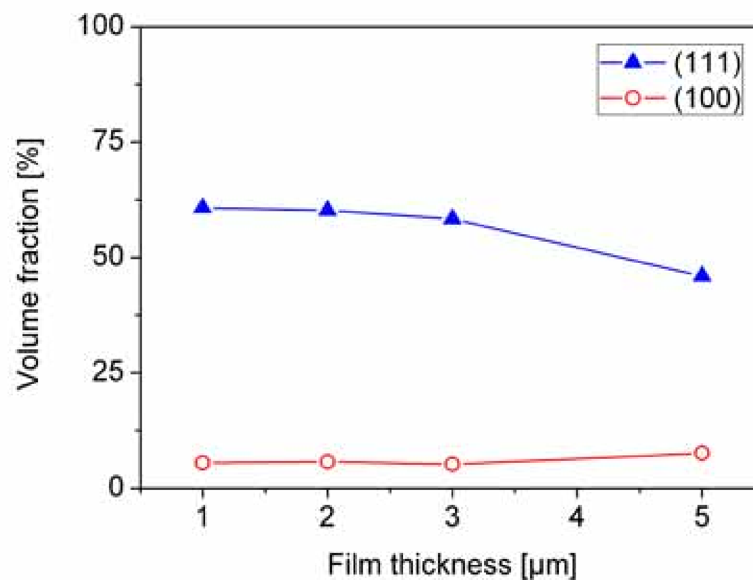

Figure 6.2: Volume fractions of texture components (111) and (100) for different film thicknesses of the as-deposited Cu films.

Using the Tango HKL software, the (111) and (100) texture components were divided into subsets allowing a separate analysis. For grain detection, a critical misorientation of 5° was specified and the twin boundaries were excluded.

The resulting grain size distributions are shown in an exemplary way for the 5 µm thick film in Fig. 6.3. The absolute frequency of the grains is plotted as a function of grain size for the entire grains, the (111) oriented grains and the (100) oriented grains, respectively. Additional analysis showed that the films had roughly a log-normal distribution; The mean grain sizes for the different film thicknesses are summarized in Tab. 6.1 and Fig. 6.4.

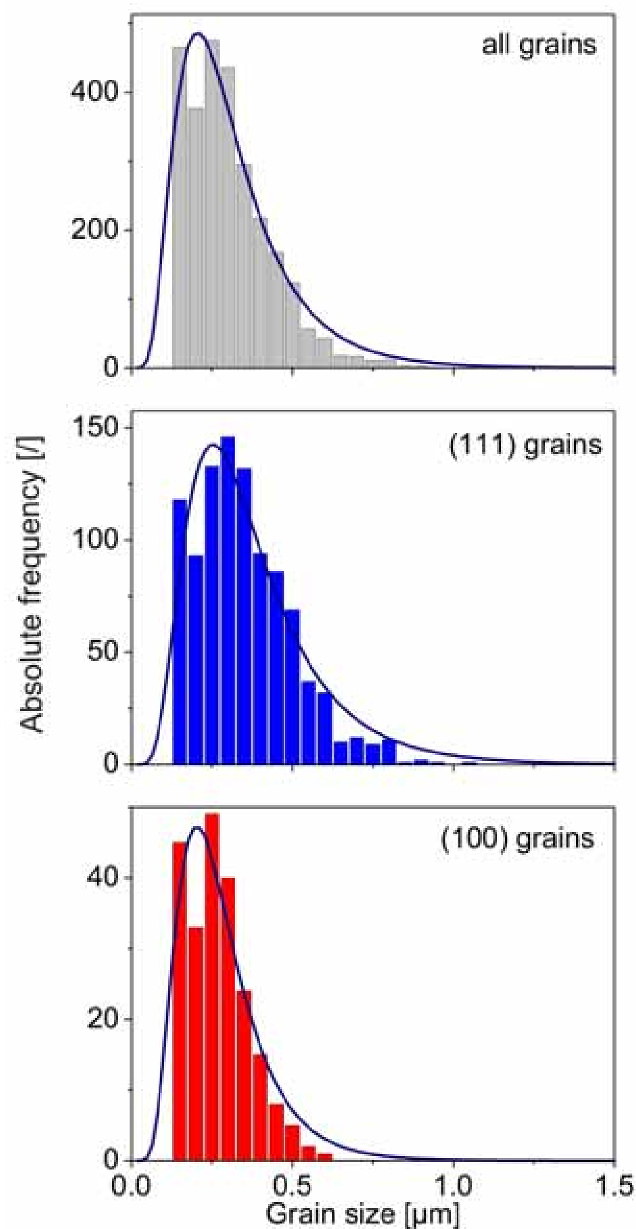

Figure 6.3: Grain size histograms for the entire number of grains, the (111) and (100) oriented grains of the 5 µm thick film.

Table 6.1: Results of EBSD measurements – mean grain size and standard deviation for the different film thicknesses: d_{total}, d_{111} and d_{100} are the mean grain sizes of the entire amount of detected grains, the (111) oriented grains and the (100) oriented grains, respectively.

Fim thickness [μm]	d_{total} [nm]	d_{111} [nm]	d_{100} [nm]
5	280±130	327±150	247±96
3	272±138	320±162	224±92
2	249±119	288±136	205±73
1	208±86	229±97	173±52

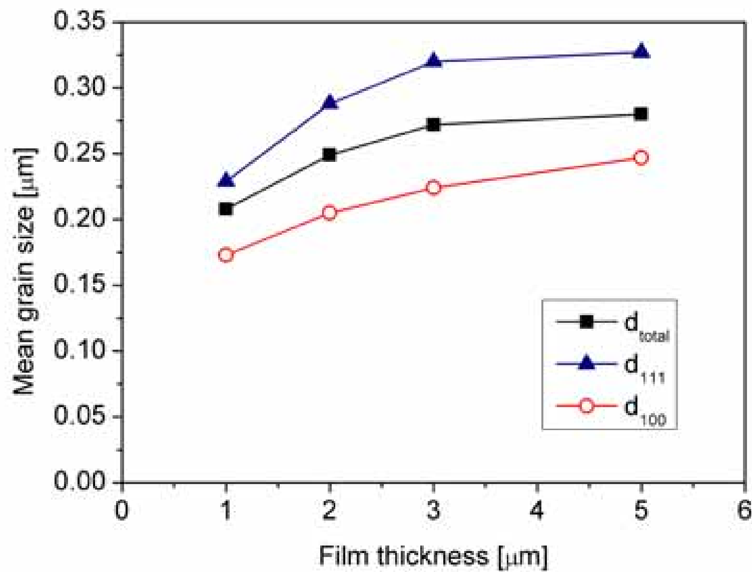

Figure 6.4: Initial mean grain size of the entire amount of detected grains, d_{total}, the (111) oriented grains, d_{111}, and the (100) oriented grains, d_{100}.

The results show a remarkably smaller amount of (100) oriented grains (Fig. 6.1 and 6.3), combined with a smaller grain size of the (100) oriented grains (Tab. 6.1 and Fig. 6.4) compared to the (111) grains. This observation holds for all the different film thicknesses.

6.3.2 Texture evolution

The typical development of the grain structure after different annealing times at 104 °C for the 5 μm thick film is shown in figure 6.5. After 2 hours, preferred "abnormal" grain growth of the (100) oriented grains becomes evident, while the "matrix" grains remained mainly (111) oriented. Preferred grain growth continued during the next 24 hours. Analogous experiments were carried out at 90 and 118°C and for 1, 2 and 3 μm thick films.

The final microstructures and microtextures obtained are presented in Fig. 6.6. Clearly higher annealing temperatures and higher film thicknesses result in a higher final (100) fraction. For the thinnest film and low annealing temperatures, (100) grains are rather rare and do not increase their volume fraction during grain growth. The final texture information is summarized in Figs. 6.8 and 6.9. Fig. 6.8 shows the inverse pole figures of each film thickness and annealing temperature. A dominant (100) texture fraction is found for the thickest films, while both components, (111) and (100), are visible for the 3 μm thick film after annealing at 104 and 118°C. For lower annealing temperatures or smaller film thicknesses the (111) texture is dominant after annealing.

The final volume fractions of (111) and (100) oriented grains are summarized in Fig. 6.8 for a given annealing temperature. The volume fractions were determined from the area fraction of pixels of this orientation assuming a columnar microstructure, which was confirmed by FIB cross sections for the (100) oriented grains. A maximum misorientation angle of 15° was allowed for assignment of orientations to each texture component. A transition in the final dominant texture was found for all annealing temperatures. This "cross-over" occurred at film thicknesses of 4.5, 3.9 and 3.4 μm for annealing temperatures of 90, 104 and 118°C, respectively.

As the same area was scanned repeatedly for more than 24 hours, the texture evolution during annealing could have been studied as function of temperature. The (100) texture development is summarized quantitatively in Fig. 6.9 for the different annealing temperatures and film thicknesses.

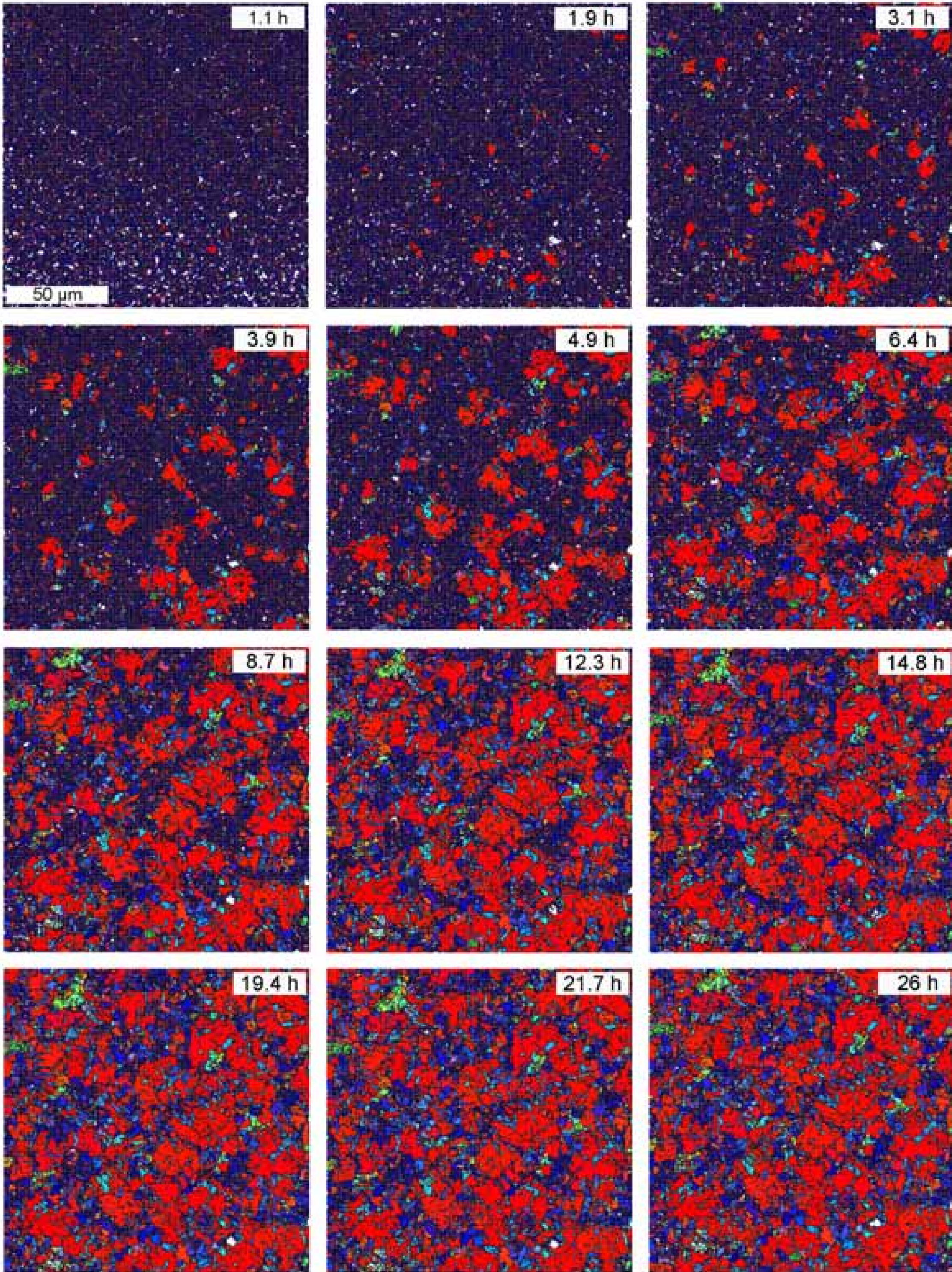

Figure 6.5: EBSD maps for 5 µm thick Cu film at 104°C for different annealing times reveal the evolution of abnormally large (100) oriented grains (marked red) between 1.1 and 26 h.

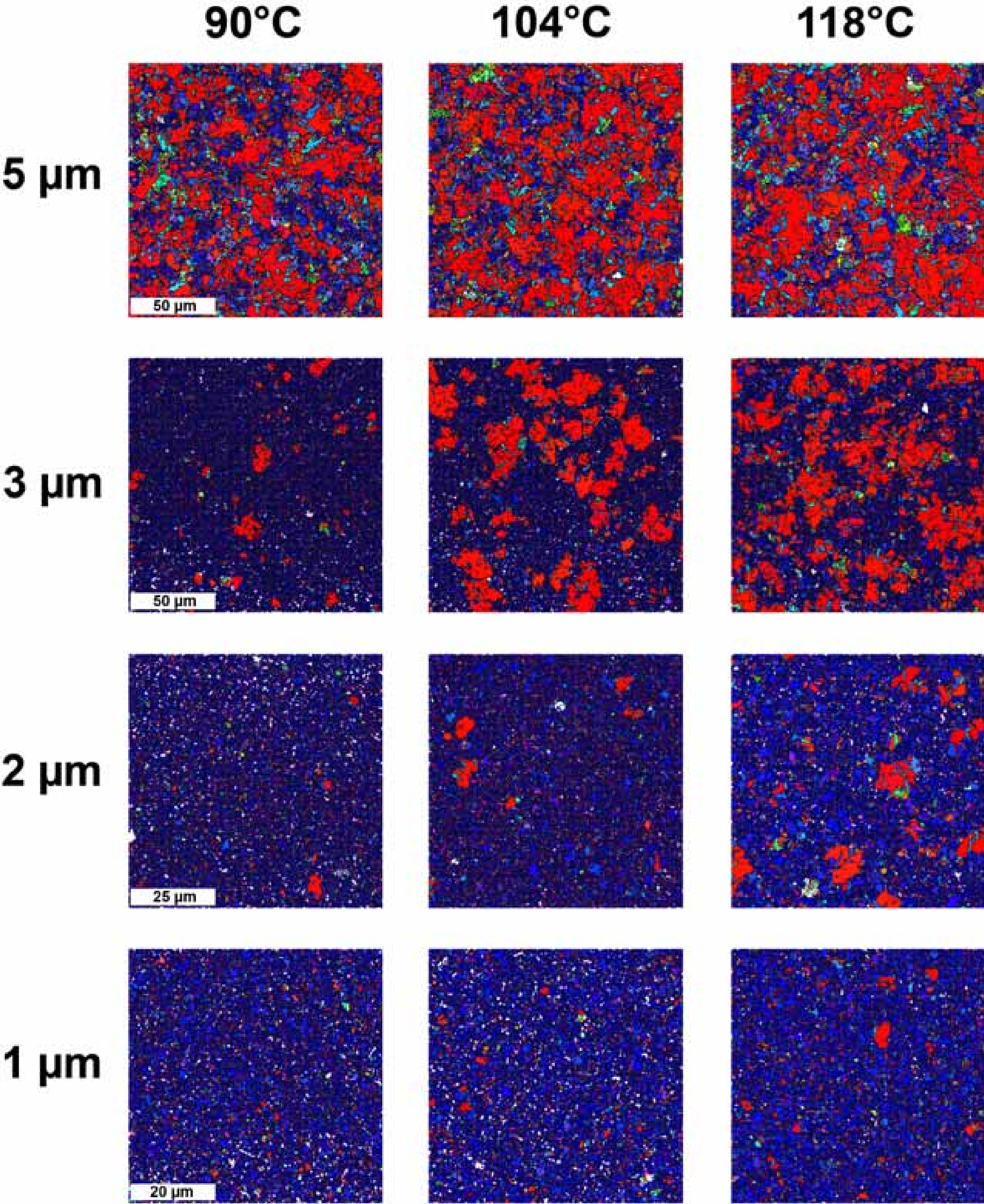

Figure 6.6: Final texture (after annealing for more than 24 h) for 1, 2, 3 and 5 µm thick films after annealing at 90, 104 and 118°C.

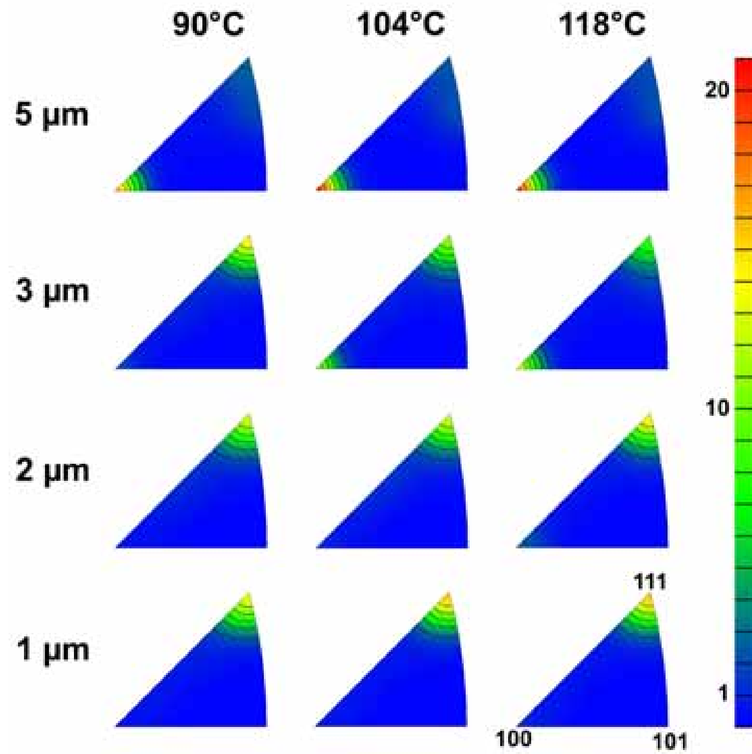

Figure 6.7: Inverse pole figures of 1, 2, 3 and 5 µm thick films after annealing at 90, 104 and 118 °C. Texture populations are measured in units of times random.

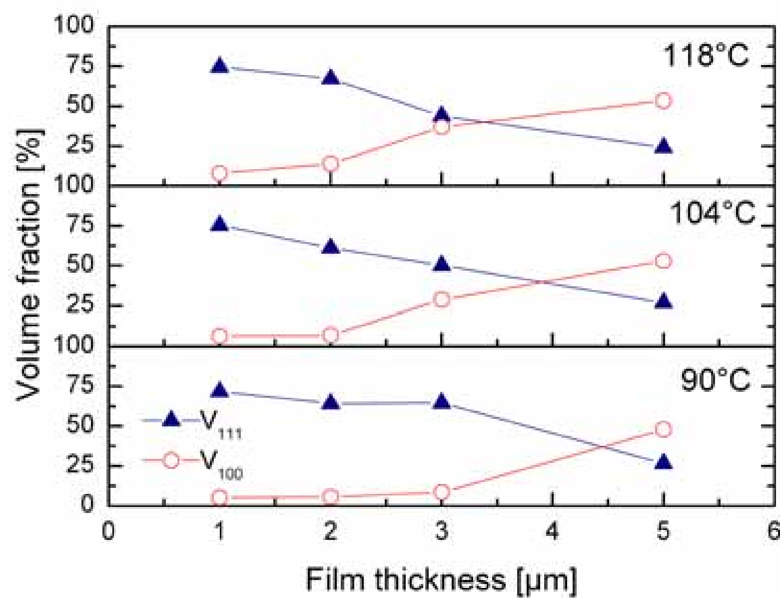

Figure 6.8: Final volume fractions of (111) and (100) oriented grains after annealing for about 24 hours at 90, 104 and 118°C as a function of film thickness. A maximum misorientation angle of 15° was allowed for assignment of orientation to each texture component. The texture "cross-over" occurred at a film thickness of 4.5, 3.9 and 3.4 µm for annealing temperatures of 90, 104 and 118°C, respectively.

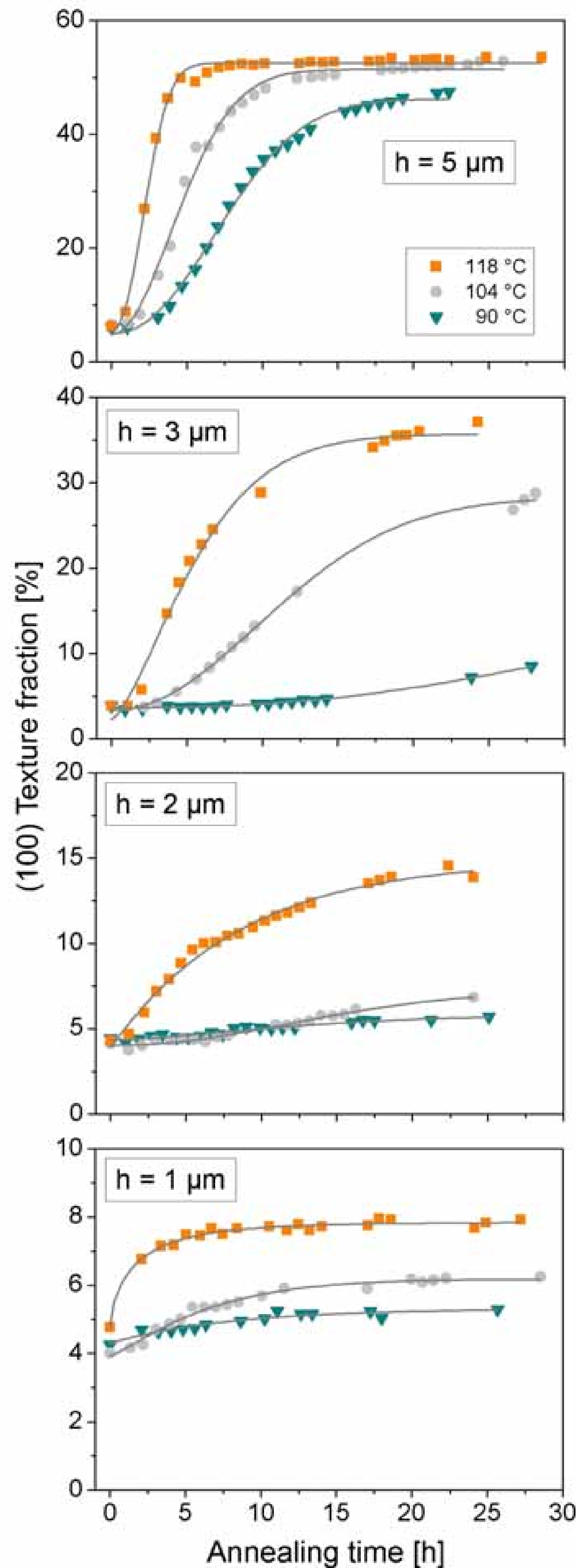

Figure 6.9: (100) texture component (fraction of pixels) for different film thicknesses as a function of annealing time for annealing temperatures of 90, 104 and 118°C. Gray lines present JMAK-fits.

6.3.3 Grain size evolution

One of the advantages of the EBSD method is that grain growth can be followed as a function of time. The mean grain sizes are presented in Fig. 6.10. For this analysis only (100) oriented grains larger than a critical size of 1 µm were used. For grain detection, a critical misorientation of 5° was specified and the twin boundaries were ignored. The border grains were excluded from the grain size statistics. A grain was allotted to a particular texture component if at least 50% of the grain possessed this particular orientation. This criterion is important because most of the (100) grains contain twins (Figs. 6.5 and 6.6).
The initially linear grain size development (for ca. 5 hours) is marked in Fig. 6.10. The curves then bend over and reach asymptotic values. The results of the initial grain growth velocities are summarized in Table 6.2. The values lie between 40 and 662 nm/h. A clear increase of growth velocity was observed for increasing film thickness and temperature.

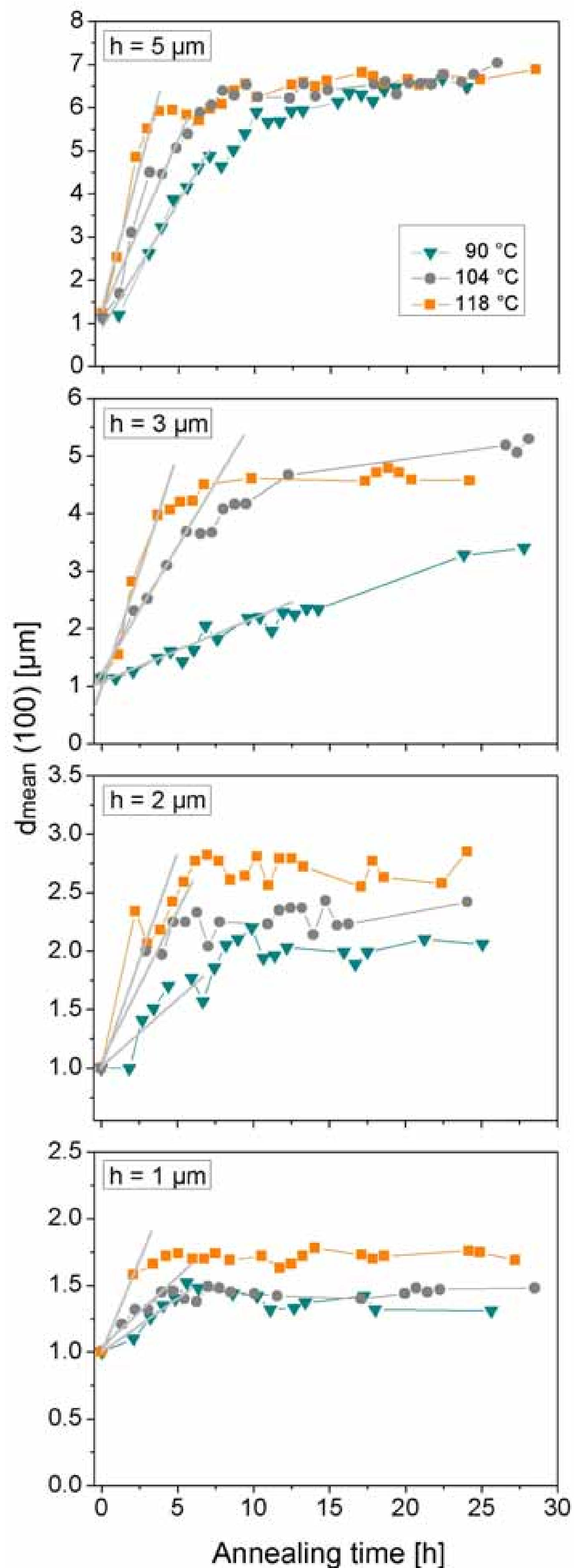

Figure 6.10: Grain size statistics: Mean grain size d_{mean} of (100) oriented grains as a function of annealing time for different annealing temperatures. The straight lines show the initial slope corresponding to v_{mean} in Table 6.2.

These grain growth velocities were used to determine the activation energy of the grain growth process. The Arrhenius plot is presented in Fig. 6.11. The activation energy is determined form the slope of the fitted lines. The values are listed in Tab. 6.3 and lie between 0.44 and 0.83 eV/atom.

Table 6.2: Initial grain growth velocities [nm/h] for the mean grain size (v_{mean}) at annealing temperatures of 90, 104 and 118°C.

v_{mean} [nm/h]	90°C	104°C	118°C
5 µm	241 ± 15	400 ± 45	662 ± 73
3 µm	61 ± 35	222 ± 20	404 ± 54
2 µm	58 ± 15	129 ± 22	184 ± 31
1 µm	40 ± 4	53 ± 4	138 ± 30

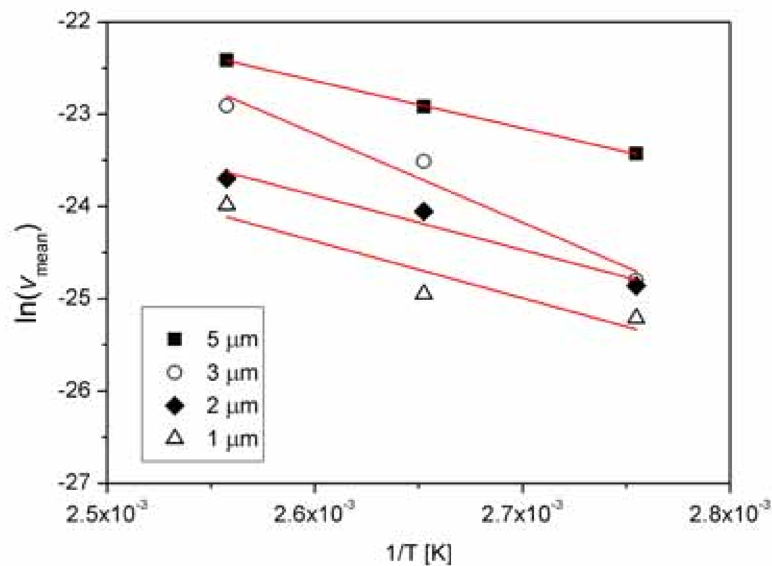

Figure 6.11: Arrhenius plot of ln(v_{mean}) versus 1/T, where v_{mean} is the mean grain growth velocity and T the annealing temperature. The slope of the fitted lines gives the activation energy Q.

Table 6.3: Activation energy determined from Fig. 6.10

Film thickness	5 µm	3 µm	2 µm	1 µm
Activation energy [eV/atom]	0.44 ± 0.1	0.83 ± 0.16	0.51± 0.1	0.53 ± 0.19

6.3.4 XRD Results

An experiment analogous to the *in situ* EBSD experiments was carried out in an XRD chamber. The strain and texture evolution was investigated by XRD measurements[3]. A 3 μm thick Cu film was annealed at 100°C for 25 hours. Subsequent XRD measurements were carried out, determining the crystallographic texture and strain in the (111) and (100) oriented grains during annealing. The procedure of the stress measurement is based on the $\sin^2\psi$-method [Noyan and Cohen 1987]. Therefore both line profile measurements and texture analysis were performed. The intensity of the (111) and (200) peaks as a function of annealing time are presented in Fig. 6.12.

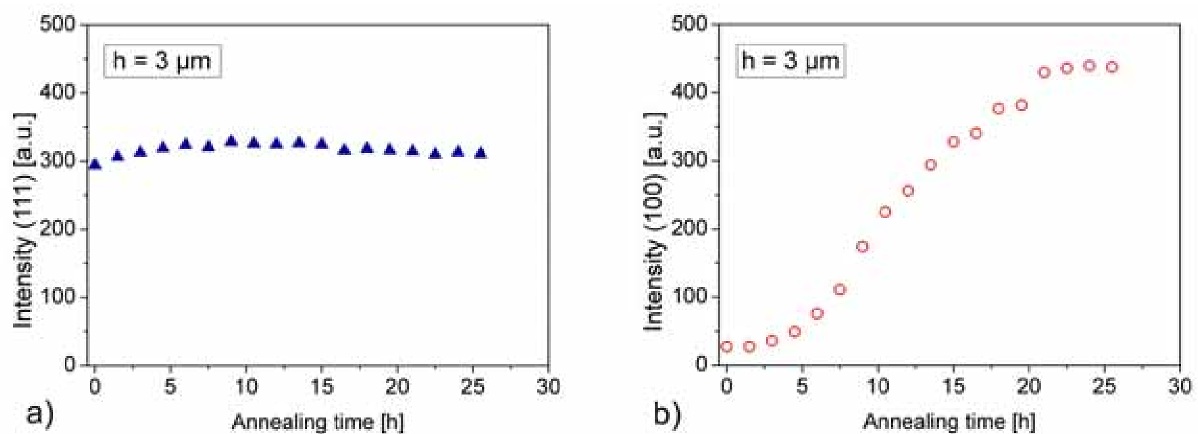

Figure 6.12: Integrated intensity of (a) (111) and (b) (100) oriented texture fractions. The 3 μm thick Cu film was annealed at 100°C for 25 hours. Subsequent XRD measurements were carried out during annealing.

Initially, high intensities were measured for the (111) texture fraction, while those with (100) orientation yielded only very low values. During annealing, the (100) intensity increased remarkably, and simultaneously the (111) intensity remained constant.

Comparing the intensity of the (100) texture fraction measured by XRD to the values obtained from EBSD in the analogous measurement, good agreement is found between them (Fig. 6.13).

---

[3] XRD measurements were carried out in the ZWE of the MPI of Metals Research by Yener Kuru and Udo Welzel.

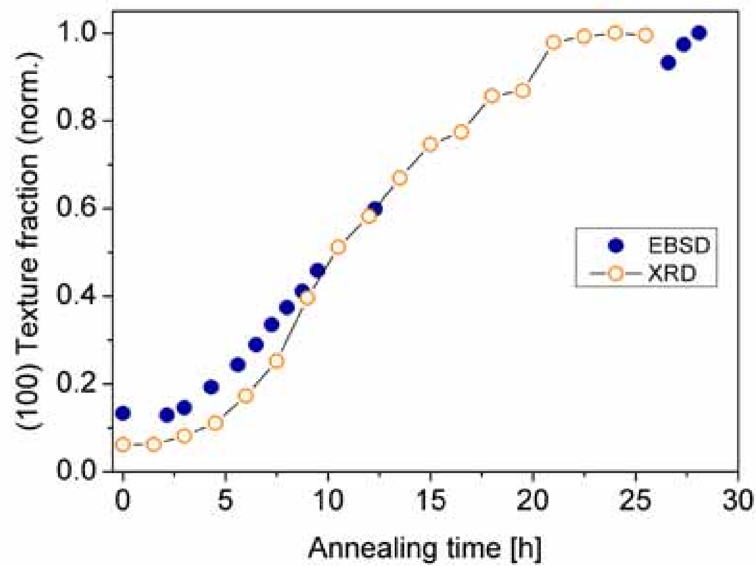

Figure 6.13: Comparison of texture evolution measured by EBSD and XRD.

The evolution of the half-width-at-half-maximum (HWHM) of the (111) and (100) line profiles is shown in Fig. 6.14 for the 3 µm thick Cu film.

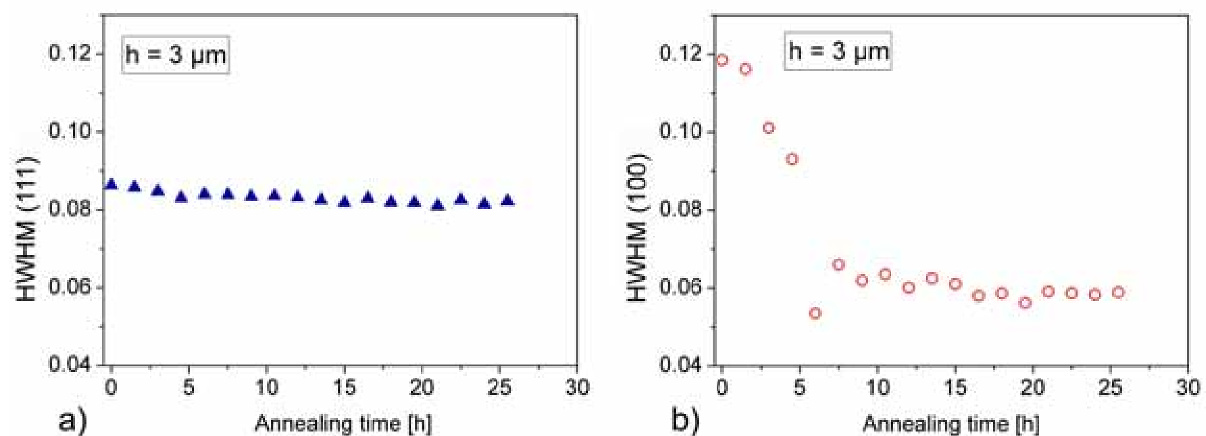

Figure 6.14: Evolution of the peak width (HWHM) of a 3 µm thick Cu film during annealing at 100°C.

For the as-deposited state, the (111) peaks were considerably narrower than the (100) line profiles. During annealing, the (100) peaks became narrower while the HWHM remained nearly unchanged for the (111) texture fraction. After annealing, the peak width of the (100) grains was well below the values of the (111) oriented grains.

Initially, the stresses were small in both grain orientations. While the (100) grains were almost stress-free, the compressive stress in the (111) grains was about 55 MPa. Then, during annealing, a small tensile stress (below 50 MPa) built up in the

(100) grains. On the other hand, there was no big change in stress for the (111) texture fraction – it remained compressive.

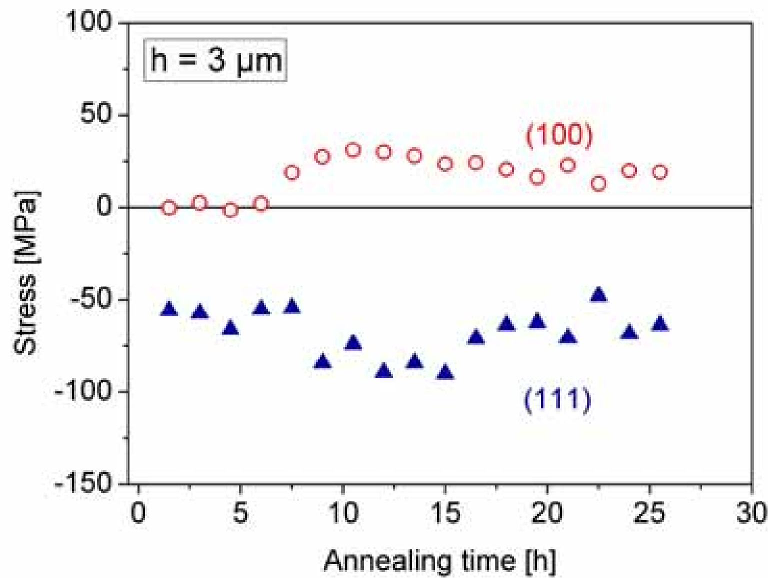

Figure 6.15: Stress behaviour of 3 µm thick Cu film during annealing at 100°C for 25 hours. The measurements were based on the $\sin^2\psi$-method. During annealing, a small tensile stress (below 50 MPa) built up in the (100) grains. No big change in stress for the (111) texture fraction was observed.

6.4 Discussion

Texture transition

We will first concentrate on the texture transition during annealing in the Cu films (Figs. 6.9). As grain growth progressed during the isothermal treatments, (100) oriented grains developed until a specific final texture fraction was reached. For the thicker films, it is obvious that this grain growth process follows a conventional s-shaped curve, which can be modelled by using a modified type of Johnson-Mehl-Avrami-Kolmogorov (JMAK) equation [Srolovitz *et al.* 1985]. This model is used to describe transformations involving nucleation and growth processes (ch. 2.1.2). Although some of the presumptions of this model (such as isotropic growth) are not fulfilled in the case of abnormal grain growth, the parameters obtained from this model can be useful for getting insight into the mechanisms of this phenomenon.

Following, Srolovitz et al., we fit our results to the following equation:

$$X(t) = c \cdot \left(1 - b_f \cdot e^{\left(-at^n\right)}\right) \tag{6.1}$$

where *a* is a constant and *n* is generally referred to as the Avrami exponent. The parameter b_f stands for the certain fraction of the grains which are favourably oriented in the as-deposited structure. In this study, the texture fraction *X(t)* of abnormal grains does not reach 100%; therefore the final texture fraction *c* has to be considered in the model. The fits are shown in Fig. 6.9 by gray lines.

Tabel 6.4: Avrami exponent *n* for different film thicknesses and annealing temperatures.

n	90 °C	104 °C	118 °C
5 µm	2.18	1.96	2.22
3 µm	2.43	2.03	1.45
2 µm	1.48	2.07	1.02
1 µm	0.98	1.2	0.67

In this study, the values for *n* lied between 2.44 and 0.67 (Tab. 6.4). More precisely, the values in the order of 2 are reached by the thicker (3 and 5 µm) films.

The theoretical value of *n* depends on the assumptions made for the nucleation rate: In thin films, when all nuclei are created simultaneously, n = 2 or for continuous nucleation n = 3 [Ling and Anderson 1992]. Experimentally, the value of *n* is found to have a large scatter between the theoretical expected values and values of the order of 1 [Humphreys and Hatherly 1995]. The low values for the Avrami exponent cannot easily be explained by the JMAK theory. Consequently, taking the texture fractions at a given time as a single input is insufficient for describing the complex mechanisms involved in the abnormal grain growth of Cu thin films.

Driving force

Next, we will focus on the abnormal grain growth velocity (Fig. 6.10 and Tab. 6.2) of the (100) oriented grains. Initially a linear increase in grain size with time is

found, which is followed by a bend to asymptotic values. Theoretical work on abnormal grain growth [Rosi 1952, Thompson 1985] characterized the growth of an individual abnormal grain into a matrix of grains as exhibiting a linear increase in radius with time. Such a linear relationship was also found in simulations of abnormal grain growth [Srolovitz *et al.* 1985, Frost *et al.* 1992] and in the initial state of annealing of this work. Analysing the absolute values of the grain growth velocities, further information about the driving force of abnormal grain growth can be assessed. As presented in Tab. 6.2., grain boundaries in the film are moving at a speed v of the order of 40-700 nm/h.

Knowing this grain growth velocity v and the grain boundary mobility, the driving forces acting on the grain boundaries can be determined (Tab. 6.2., eq. 1.3). Vandermeer et al. [Vandermeer *et al.* 1997] measured a mobility of $6.31\cdot10^{-16}$ m^4/Js at 121°C when analysing the recrystallization of cold-deformed Cu. In order to calculate the pre-exponential factor M_0, the activation energy of grain growth is needed.

The activation energies determined form Fig. 6.11 (Tab. 6.3) exhibit a large scatter from 0.44 to 0.83 eV, making a reasonable estimate of grain boundary mobility impossible. As a consequence, we resort to an activation energy value of 0.62 eV determined by Donthu et al. [Donthu *et al.* 2003] for a 1.5 µm thick Cu film by differential scanning calorimetry. The growth mode was abnormal as for the current study.

Using the known activation energy of 0.62 eV/atom and the mobility measured by Vandermeer, the preexponential factor, M_0, can be determined (eq. 1.3) to $5.38\cdot10^{-8}$ m^4/Js. With the help of this factor, M_0, it is possible to extrapolate the mobility, M, to the current annealing temperatures. The results are presented in Tab. 6.5.

Table 6.5: Calculated grain boundary mobility as a function of temperature.

Temperature	90°C	104°C	118°C
Mobility [m^4/Js]	$1.33\cdot10^{-16}$	$2.77\cdot10^{-16}$	$5.49\cdot10^{-16}$

Using these values, the acting driving forces can be calculated as $p = v/M$. The results are summarized in Tab. 6.6 and lie between $5.3 \cdot 10^4$ and $6.1 \cdot 10^5$ J/m^3, for 1 and 5 μm thick films, respectively. Like the grain growth velocities (Tab. 6.2), the driving forces increase with increasing film thickness. This observation is discussed in the next section.

Table 6.6: Calculated driving forces *p* in J/m³ acting on the (100) grain boundaries at annealing temperatures of 90, 104 and 118°C.

Filme thickness	90°C	104°C	118°C
5 μm	$6.1 \cdot 10^5 \pm 0.9 \cdot 10^5$	$4.0 \cdot 10^5 \pm 0.5 \cdot 10^5$	$3.4 \cdot 10^5 \pm 0.4 \cdot 10^5$
3 μm	$1.1 \cdot 10^5 \pm 0.3 \cdot 10^5$	$2.2 \cdot 10^5 \pm 0.2 \cdot 10^5$	$2.1 \cdot 10^5 \pm 0.3 \cdot 10^5$
2 μm	$1.2 \cdot 10^5 \pm 0.3 \cdot 10^5$	$1.3 \cdot 10^5 \pm 0.2 \cdot 10^5$	$9.3 \cdot 10^4 \pm 1.5 \cdot 10^4$
1 μm	$8.5 \cdot 10^4 \pm 0.8 \cdot 10^4$	$5.3 \cdot 10^4 \pm 0.4 \cdot 10^4$	$7.0 \cdot 10^4 \pm 1.5 \cdot 10^4$

Now, estimates for the possible driving forces are made. Knowing the size of the acting driving forces (Tab. 6.6), such an estimate should help to identify the critical one.

1) **Grain boundary energy minimization**:

A first contribution results form the energy that can be gained by eliminating the grain boundary area in the film (eq. 1.5). For calculating an upper limit for this driving force, it is assumed that all grain boundaries in the as-deposited film are high-angle grain boundaries with a grain boundary energy of γ_{gb} = 0.6 J/m² [Inman and Tipler 1963, Viswanathan and Bauer 1973]. The mean values for grain sizes are listed in Tab. 6.1. The resulting driving force lies in between $-3 \cdot 10^5$ and $-6 \cdot 10^5$ J/m³. The negative sign says that this driving force does not prefer the growth of the (100) grains. As they are initially smaller than the mean grain size, they are expected to shrink and disappear. Therefore this kind of driving force cannot explain their preferred growth.

2) **Surface energy minimization:**

Anisotropic surface energies are a second possible source of a driving force for grain growth (eq. 1.7). Their value lies between $-2.6 \cdot 10^5$ and $-5.2 \cdot 10^4$ J/m³ for the 1 μm and 5 μm thick film, respectively. Again this estimate is an upper limit, as the grains in the as-deposited microstructure are not columnar. And again this surface/interface

energy minimization cannot result in the preferred growth of (100) oriented grains, as their surface energy is not minimal.

3) **Strain energy minimization:**

The driving force for strain energy minimization induced by a thermal expansion mismatch between film and substrate is given by eq. 1.12. It is of the order of $8 \cdot 10^3$ and $1.6 \cdot 10^4$ J/m³ for annealing temperatures of 90 and 118°C, respectively. Again this estimate is an upper limit, as it is assumed that there is no temperature increase in the sample during sputter deposition. A dominance of this driving force can result in preferred growth of (100) oriented grains. But when comparing this driving force to the others acting on the grain boundaries, it is obvious that it cannot overcome the driving force due to grain boundary elimination and surface energy minimization. As a consequence, this driving force cannot be the explanation for abnormal grain growth, as it is much too small.

4) **Initial stresses:**

Initial macrostresses are very low for all film thicknesses (below 50 MPa). Although there is a stress difference between the (111) and (100) component (Fig. 6.15), it is not sufficient (order of 10^3 to 10^4 J/m^3) to induce abnormal (100) grain growth.

5) **Defect density:**

During sputter deposition, defects can be produced by ion bombardment and affect grain growth kinetics. Therefore, dislocations in the as-deposited grains are a further possible reason for a driving force. For an area density ρ of dislocations, the stored strain energy is thus given by

$$\Delta W_{dis} = \frac{1}{2} G b^2 \rho \qquad (6.2)$$

where the shear modulus G is $4.21 \cdot 10^{10}$ N/m² and the burgers vector b is 0.256 nm.

Assuming a typical dislocation density of $3 \cdot 10^{14}$ 1/m² (Fig. 6.15), which lies somehow below reported typical dislocation densities of 10^{15} 1/m² in thin films [Shan and Wang 1998, Wasa and Hayakawa 1992 p. 13], a driving force of $4.2 \cdot 10^5$ J/m³ is calculated. Comparing this result to the acting driving forces (Tab. 6.6), it is found that could give an explanation for the observed driving forces and grain growth

velocities. Nevertheless, it is not clear why the reduction of dislocation density prefers the growth of (100) oriented grains. This question is discussed below.

A further hint for the critical importance of defect density is found when analysing the HWHM of the (100) texture fraction, where a steep decrease is observed (Fig. 6.14b). Knowing the initial (100) grain size to be 224 nm (Tab. 6.1), estimates of the contribution of the grain size to peak broadening revealed that the broadening stems mainly entirely from microstrain. As a consequence, from the HWHM, the average dislocation density can be obtained (Fig. 6.16) [Williamson and Smallman 1956, Lucks *et al.* 2004]. First the integral breadth, the HWHM, was calculated, then this integral breadth was corrected according to the instrumental breadth. An isotropic distribution of dislocations was assumed. Note that the dislocation density vanishes after 6 hours since the measured integral breadth of the specimen and the instrumental breadth are practically the same.[4]

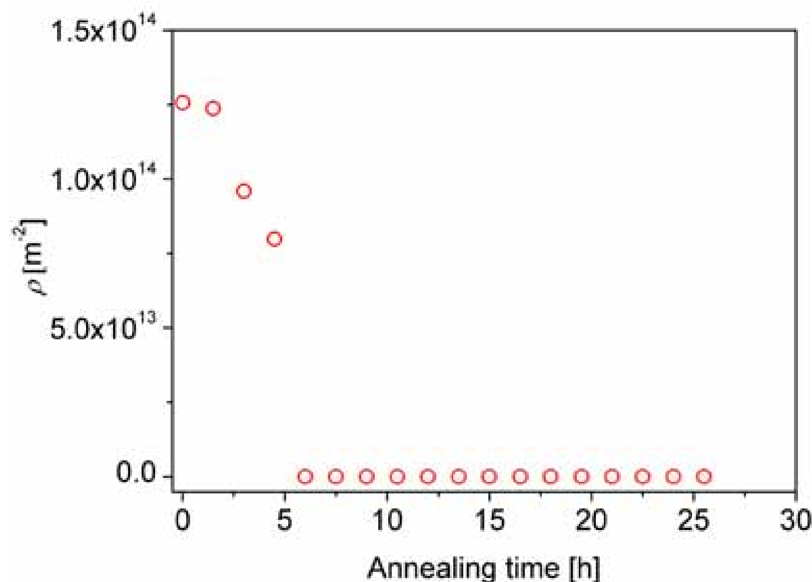

Figure 6.16: Dislocation density in (100) oriented grains as a function of annealing time in a 3 µm thick Cu film. A steep decrease from $1.25 \cdot 10^{14}$ 1/m² is found during annealing.

Why (100)?

But why a high dislocation density should prefer the growth of (100) oriented grains and cause a transition towards a (100) texture? Two models, both with the

[4] Calculation of dislocation density was carried out by Yener Kuru in the ZWE of the MPI of Metals Research.

potential to give an explanation for this behaviour are discussed in the following section.

As the microstructural changes are found to be defect driven, this grain growth can be described best by the term “recrystallization”. In literature, the recrystallization texture for cold rolled Cu sheets is well known to be the cube texture (100)<001>, with the (100) plane parallel to the sheet surface. The 40°<111> orientation relationship between the plane strain rolling texture and the cube texture is claimed to be associated with oriented growth caused by grain boundary mobility anisotropy [Beck 1991, Beck 1952]. Boundaries in the vincinity of a 38° rotation about a <111> misorientation axis are found to have high mobility [Beck *et al.* 1950, Huang and Humphreys 1999, Molodov *et al.* 2003, Taheri *et al.* 2004]. These highly mobile grain boundaries were characterized as near-Σ7 type coincidence site lattice (CSL) boundaries. As the grain growth velocity is determined by both mobility and driving force, an increased grain boundary mobility could be responsible for the preferred growth of specific grains.

In order to check whether these boundaries have significant influence on the observed growth of (100) grains, their boundaries are analysed. The EBSD technique allows to detect the misorientation between grains and to identify special CSL boundaries. The results are presented in Fig. 6.17. Neither Σ7 nor grain boundaries with a misorientation in the range of 37-40°, are found responsible for the preferred growth of (100) oriented grains.

Although these grain boundaries could not be held responsible for the abnomal growth of (100) grain, the mobility is still an important criterion. Analysing the activation energy determined from Fig. 6.11, an interesting observation was made: Literature values for grain growth in Cu thin films lie in between 0.62 [Donthu *et al.* 2003] and 1.1 eV [Detavernier *et al.* 2003b]. Taking a closer look at the literature results, it is obvious that the higher activation energies around 0.9 eV/atom are found when (111) grain growth is observed [Cabral Jr. *et al.* 1999, Brongersma *et al.* 2002a, Schell *et al.* 2005]. This is in good accordance to 0.92 eV/atom which is found for copper grain boundary self diffusion. On the other hand, Vanstreels identified an activiation energie between 0.77 and 0.79 eV for the abnormal (100) grain growth process and Donthu et al. [Donthu *et al.* 2003] found their 1.5 µm thick Cu film to possess an activation energy of 0.62 eV/atom. Unfortunately, no texture information is given in this study, but the FIB images presented allow to identify again

abnormal grain growth as growth mode. The values calculated in this study (0.44 – 0.83) are close to these values and somewhat lower than the values found for normal (111) grain growth.

The activation energy of grain boundary migration is known to depend on the grain boundary character [Taheri *et al.* 2004], indicating different migration mechanism for special boundaries. Therefore an increased mobility is assumed for the grain boundaries of the (100) oriented grains in the observed temperature range. Also, Park et al. [Park *et al.* 2007] came to the same conclusion when finding deformation-induced growth of (100) oriented grains in sputtered Cu lines. They attributed this observation to an increased grain boundary mobility due to the motion of dislocations to the boundary.

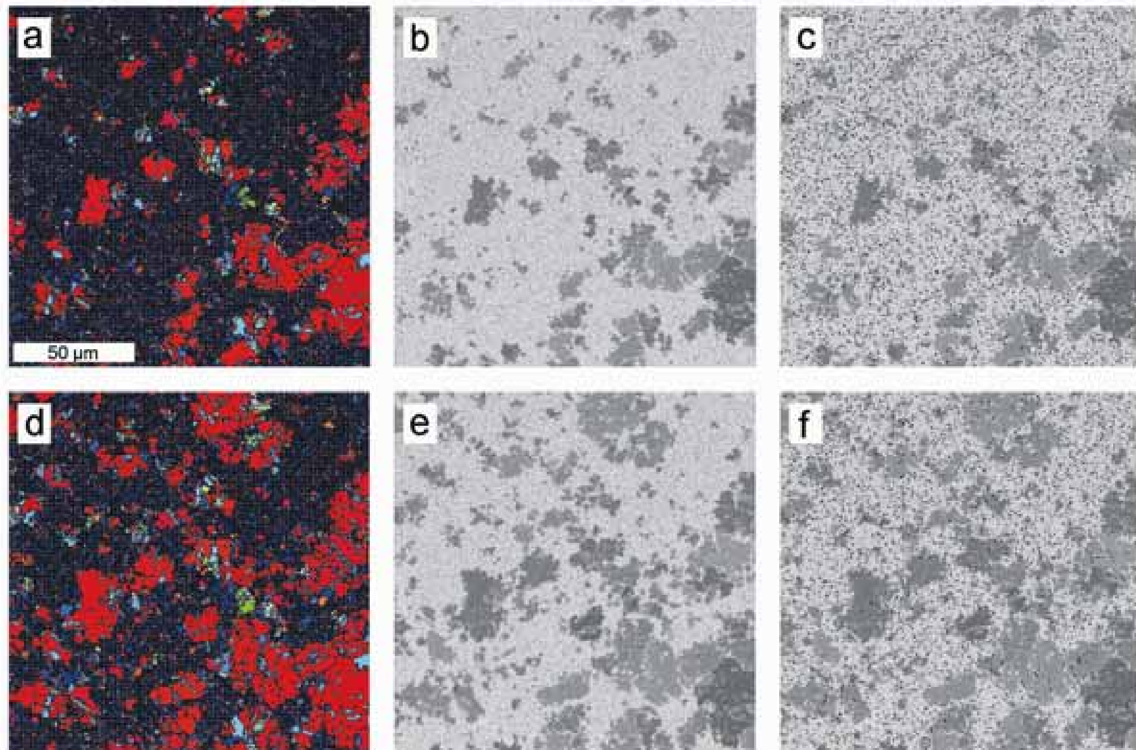

Figure 6.17: EBSD maps of 5 µm thick Cu films annealed at 118°C for 2 h (a-c) and 3 h (d-f). The differently oriented grain are shown in (a) and (d) (for legend see Fig. 3.3). Σ7 grain boundaries are highlighted in magenda in (b) and (e) where the microstructure is shown with the help of the band constrast. All grain boundaries with a misorientation in between 37-40° are presented in (c) and (f) as black lines.

It can be concluded that the properties of the grain boundary planes play definitely an important role for the grain growth velocity and texture development.

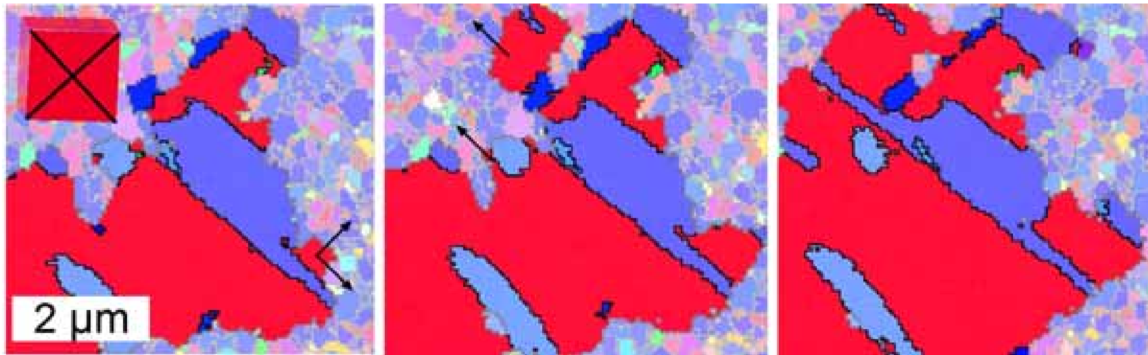

Figure 6.18: EBSD maps of 3 µm thick Cu film at 104°C: Details of abnormal grain growth are shown. The red colour marks the (100) oriented area and the blue colour represents the twins. The matrix is toned down. Insert cube shows the measured orientation of the abnormal (100) grain. The (100) plane lies parallel to the surface. Analysis of the in-plane orientation shows, that the favourite growth front directions are normal to the ‹110› direction (represented by the black arrows).

A closer look on grain growth characteristics gives an indication why the mobility is reduced: the grain boundary plane seems to play an important role. The mostly sufficient way of definition of a grain boundary is in terms of an axis and an angle of rotation. Although most of the investigations on grain boundaries rely only on misorientation, there is a growing body of evidence indicating that the properties of high angle grain boundaries are determined primarily by the orientation of the boundary plane [Randle 2010, Rohrer *et al.* 2004, Saylor *et al.* 2004]. Analysing the shape and growth process of the abnormal (100) grains, it is found that the growth front as well as the final shape is nearly always normal to the ‹110› direction of the grain (Fig. 6.18). The same observation has been made by Greiser [Greiser 1999] for (100) grains in Ag films and Mönig [Mönig 2005] for (100) grains in thin Cu lines.

Interesting agreement is found when comparing these observations to the results of Hyo-Jong et al. [Hyo-Jong *et al.* 2006]. They observed growth of a (111) oriented grain in a 1 µm thick Cu film during room temperature annealing and assumed the growth front interface to be one of the (111) planes with the lowest surface energy. In our case of a (100) oriented grain, the projection of the ‹111› growth direction into the (100) plane leads to two possible growth directions [1-10] and [110], as observed in this study (Fig. 6.18). The faceted grain boundaries are strong evidence for the existence of grain boundary energy anisotropy. This preferred growth directions result in the specific rectangular shape of the abnormal (100) grain, as the [110] and [1-10] enclose an angle of 90°. This shape is disturbed by the twins, giving the grains their specific fragmented structure.

But there is another model which gives a possible explanation for the preferred growth of the (100) oriented grains. Up to now, the models describing recrystallization textures did not take the dislocations into account, although they represent the major driving force. The answer may be given by the strain energy release maximization (SERM) model developed by Lee [Lee 1995, Lee 1996, Choi *et al.* 2000, Lee 2005a, Lee 2005b], originated from the interpretation of the relationships between initial and recrystallization textures. He assumes the recrystallized grains to orient themselves so that their minimum elastic modulus direction is parallel to the maximum absolute stress direction (Fig. 6.19). The direction of the maximum stresses is parallel to the Burgers vector, which is the ‹110› direction in Cu, and the minimum elastic modulus direction is the ‹100› direction. There are six equivalent directions in the ‹110› directions, but as strain is highest in the plane of the film, the ‹110› directions parallel to the surface become the ‹100› directions after recrystallization. For an initial (111) texture, three of the six ‹110› directions lie in the plane of the film, which are able to change to the ‹100› directions (Fig. 6.19b). But angles between the ‹110› directions are 60°, while the angles between the ‹100› directions are 90°. Therefore it is assumed that two of the ‹110› directions in neighbouring grains, that are at right angles, are parallel to the ‹100› direction of nuclei formed in a boundary between these grains. These nuclei have the (100) orientation. Therefore, the (111) deposition texture is expected to change into a (100) recrystallization texture. Also for an inital (100) texture a change towards a recrystallization (100) texture is predicted.

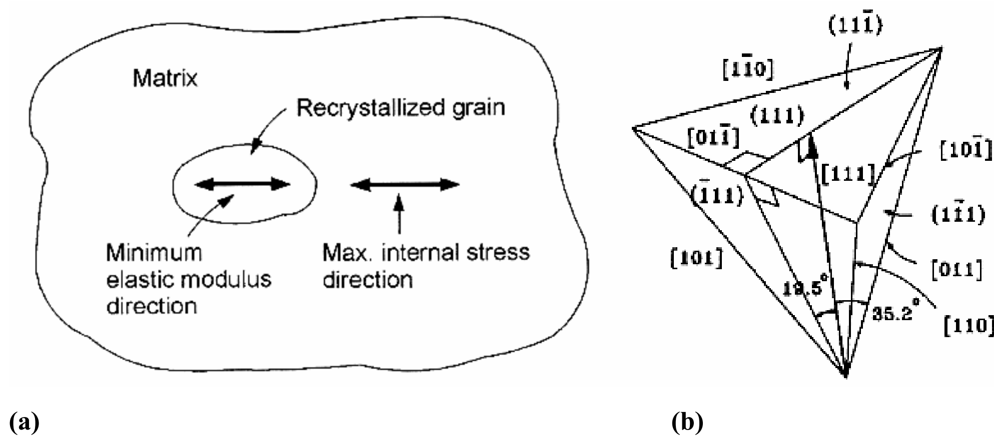

(a) (b)

Figure 6.19: (a) Arrangement of matrix and recrystallized grains. The energy release can be maximized when the maximum stress direction is parallel to the minimum elastic modulus direction of the recrystallized grains [Choi *et al.* 2000]. (b) ‹110› directions in (111) textured materials [Lee 1996].

This model is based on the assumption that the dislocation alignment can be described by a simple arrangement of edge dislocations, which allows to identify the Burgers vector as maximum stress direction. And, it cannot only explain the recrystallization textures in films, but also in axisymmetrically deformed fcc metals, plane strain rolled and compressed fcc metals and cold rolled bcc steels, tantalum, molybdenum and tungsten [Lee 1999a, Lee 2000]. This model has an analogue concept like the texture evolution model of Thompson and Carel (ch. 2). But while Thompson and Carel [Thompson and Carel 1995] takes strains due to the thermal mismatch in between film and substrate into account, Lee [Lee 1995, Choi *et al.* 2000] assumes the defect density to be responsible for the dominant driving force.

Increasing grain growth velocity with increasing film thickness

Our experiments reveal clearly an increasing grain growth velocity v of (100) oriented grains with increasing film thickness (Fig. 6.10, Table 6.2). Finding dislocation density to play an important role for orientation-dependent grain growth, a step back to the basics of grain growth is made, analysing the factors affecting the growth rate, v, of an individual grain.

As shown before, the driving forces are either too small (ΔW_ε) or they do not support the growth of the (100) grains. Due to this comparison, the dislocation density minimizing driving force, ΔW_{dis}, is supposed to be the dominant driving force. Using the calculated mobility (Tab. 6.4) the observed grain growth velocities were fitted. A linear increase of the defect density with film thickness, allows to fit all data points at once (eq. 1.1 and 6.2). The obtained defect density ρ is found to be described by ρ= $(5.2\cdot10^{19} \pm 1.0\cdot10^{19})\cdot h$. This results in defect densities from $5.2\cdot10^{13}$ 1/m² for 1 µm thick film to $2.6\cdot10^{14}$ 1/m² for 5 µm thick films. The grain growth velocity as well as the fitted lines are presented in Fig. 6.20.

This fit shows good agreement for all film thicknesses and annealing temperatures and is possible to explain the general trends. It allows to attribute the increased grain growth velocity with increased temperature to the higher mobility, and the increase for thicker films can be explained by the increasing dislocation density.

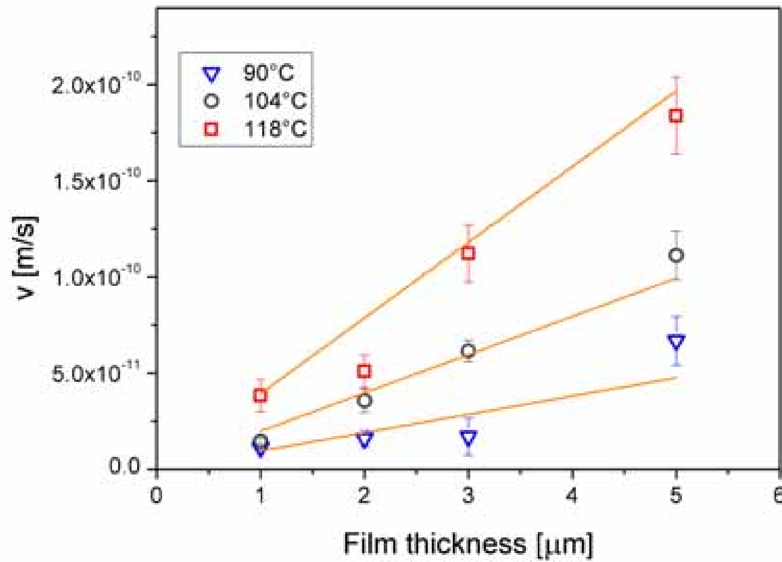

Figure 6.20: Mean grain growth velocities, v_{mean}, and fitted values, represented by orange lines. The growth velocity is calculated as product of mobility and driving force (eq. 1.3). The mobility is calculated as M=5.38·10^{-8} [m^4/Js]·exp(-0.62[eV]/RT) for 90, 104 and 118°C (Tab. 6.5). The dislocation density is found to increase with film thickness (ρ[1/m²]=5.2·10^{19}·h[m]).

When comparing the dislocation density found by the fit for the 3 µm thick film (1.56·10^{14} 1/m²) to our experimental value identified by the XRD measurements (Fig. 6.16) (1.25·10^{14} 1/m²), again excellent agreement is found, proving the fit reasonable.

On the other hand, no explanation can be given for the increase in initial defect density with increasing film thickness. This finding should be the subject of future investigations. But no matter how the dislocation density varies with film thickness, it is clear that the driving force due to a dislocation density in the range of 10^{14} 1/m² has to be considered for predicting texture evolution.

As the defect density minimizing driving force was found to play a dominant role for (100) grain growth, it is added to the expression given by Carel and Thompson (Carel *et al.* 1996):

$$v = \frac{dr}{dt} = M \cdot p = M \cdot \left[\bar{\gamma}_{gb} \left(\frac{1}{\bar{r}} - \frac{1}{r} \right) + \Delta W_s + \Delta W_\varepsilon + \Delta W_{dis} \right] \tag{6.3}$$

where r is the radius of the growing grain and $\bar{r}$ the average grain radius, p is the total driving force, M the average grain-boundary mobility, $\bar{\gamma}_{gb}$ the average grain-boundary energy and ΔW_s, ΔW_ε and ΔW_{dis} are the driving forces for surface/interface energy minimization, strain energy minimization and dislocation density minimization.

Now, not only two orientation dependent driving forces (ΔW_s and ΔW_ε) have to be compared, but also the dislocation density minimizing driving force has to be considered in order to predict a resulting texture. The graphic description of this comparison is presented in Fig. 6.21, representing an new texture map.

The red dashed curve (ΔW_ε) marks the driving force due to strain energy minimization for an annealing temperature of 118°C. As the thermal strain is too small to reach the yield stress of the films, it is constant at $1.6 \cdot 10^4$ J/m³ (eq. 1.17). It is smaller than the other driving forces, consequently the (100) grain growth cannot be driven by this driving force.

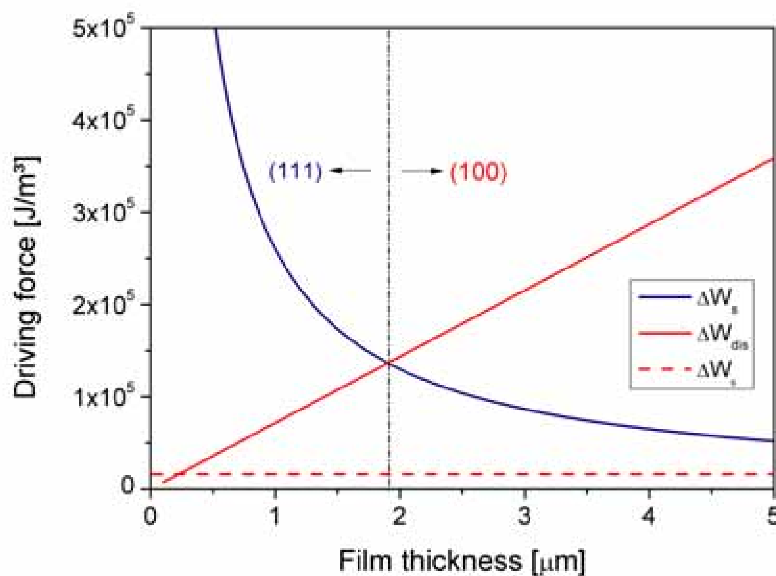

Figure 6.21: Driving force map: Estimated driving forces for strain energy minimization, ΔW_ε, surface/interface energy minimization, ΔW_s, and dislocation energy minimization, ΔW_{dis} for Cu thin films on polyimide. Dislocation energy minimization dominates above a film thickness of 1.9 µm. while surface energy minimization dominates below this value. The driving force for strain energy minimization for an annealing temperature of 118°C cannot overcome the driving force for surface energy minimization.

The blue curve (ΔW_s) represents the driving force due to surface/interface energy minimization and scales inversely with film thickness. It dominates below a film thickness of 1.9 µm. Above this value, the driving force due to dislocation density

minimization dominates. It is represented by a red curve and increases linearly with film thickness. Good accordance is found, when comparing these results to the observed grain growth behaviour. While for the 1 µm thick films, (100) grains did not grow at a higher extend, their preferred growth was observed first for the 2 µm thick film at 118°C. For the 3 and 5 µm thick films, (100) abnormal grain growth was found for all annealing temperatures. Nevertheless, the temperature dependence of texture evolution is not considered in this texture map as the mobility plays an important role. Furthermore, the initial texture has significant influence on the final texture: Even though, the (100) component did not dominate the final texture of the 3 µm thick film after annealing at 104°C (Fig. 6.8), it increased its fraction from initially 5 to final 27%. Considering just the final texture would not represent the acting driving forces correctly.

Summarizing, a texture map represents a useful possibility to estimate general trends in texture evolution. For more accurate predictions, initial textures as well as kinetics of grain growth have to be considered.

Stagnation of grain growth

Now, we direct our attention to the remarkable reduction of grain growth velocity after the initial linear growth (Fig. 6.10). The transition of 3-D to a 2-D growth behaviour cannot explain the total grain growth stagnation. It would only result in a reduction of grain growth velocity but not in stagnation [Novikov 2004].

But what makes the abnormal grains stop or slow down their growth in such a dramatic manner? The most common explanation for this behaviour is the existence of a stagnation force Carel *et al.* 1996. It predicts a stop of grain growth at a grain size of (1-2) times the film thickness [Mullins 1958]– as observed in this work. Therefore, a stagnation force, i.e. due to thermal grooves, is one possibility for the observed stop of abnormal grain growth.

But when relying on the identified driving force, dislocations may play an important role. As (100) grain growth proceeds, the dislocation density decreases (Fig. 6.16) significantly. This can be the reason for the stop of grain growth, although not the entire microstructure is transformed to (100). This can also be the explanation for an interesting difference between the experimental results and many simulations

when analysing the final texture. While in most of the simulations the entire final texture is composed of the energetically favoured grains [Srolovitz *et al.* 1985, Frost *et al.* 1992, Carel *et al.* 1996], this is not true in our results (Figs. 6.5 and 6.6). There is always a matrix fraction of (111) oriented grains left. This is because in these simulations the defect density is not considered as driving force.

Comparison to literature results

An increasing grain growth rate with increasing film thickness was observed for electroplated Cu films by several authors [Walther *et al.* 2000, Jiang *et al.* 1998, Lagrange *et al.* 2000, Pantleon and Somers 2006a, Pantleon and Somers 2007, Stangl *et al.* 2008, Brongersma *et al.* 1999b, Teh *et al.* 2001]. Their explanations are discussed in the following section.

As in some cases the observed change in grain growth velocity is correlated to different initial textures, some authors assume them to be responsible for varying grain growth velocities [Pantleon and Somers 2006a, Pantleon and Somers 2007, Ueno *et al.* 1999, Stangl *et al.* 2008]. The increasing transformation rate with increasing film thickness is attributed to the different as-deposited textures: the thicker the films, the more grains with other orientations than (111) exist, i.e. (100), exhibiting high angle grain boundaries to the surrounding matrix. As high angle grain boundaries are found to have a higher mobility, this may cause a relatively rapid growth of these i.e. (100) grains. The larger the volume fraction of (111) oriented grains, the more likely is the dominance of low-angle grain boundaries and hence the slower is the kinetics of grain growth. Analyzing the results of this study, there is indeed, a decrease in (111) fraction from 60 to 46 % from 1 to 5 µm film thickness. But on the other hand, the (100) texture fraction remains nearly constant at about 6 % for all thicknesses. As only these (100) oriented grains show the abnormal grain growth behaviour that is probably not the explanation for the observed results.

Lagrange and Brongersma [Lagrange *et al.* 2000, Brongersma *et al.* 1999a] assumed a transition from a 3-D to a 2-D grain growth to explain the decrease in grain growth rate for thinner films. When the film thickness approaches the grain size of the new grains, they are forced to proceed in two dimensions, thus slowing transformation. They observed an increase in the transformation velocity for thicker

films, varying the film thickness from 0.5 to 3 μm [Lagrange *et al.* 2000]. Analysing the current results in the light of this model, it was found that the abnormal (100) grains grew in a columnar way for all film thicknesses. Hence, that cannot be the explanation for the observed increase in the initial rate of grain growth.

Several authors assume the reduction of grain boundary energies to be the responsible driving force for microstructural changes in Cu thin films [Militzer *et al.* 2004, Freundlich *et al.* 2002, Harper *et al.* 1999, Walther *et al.* 2000]. As shown before, this driving force cannot be the reason for abnormal (100) grain growth, as they are initially smaller than the (111) oriented grains. The assumption that a particle pinning mechanism hinders normal grain growth was adopted by Harper et al. [Harper *et al.* 1999] in order to explain abnormal grain growth in 1 μm thick, electroplated Cu films. Then, as these particles coarse, their average spacing increases and some grain boundaries may break free – resulting in abnormal grain growth. But, no evidence for particle pinning of grain boundaries was given and in our case, this model can not explain the preference of grain boundaries of (100) oriented grains to break free and the increased grain growth velocity for the increasing film thickness.

Changes in defect density were not listed as reason for the increase in grain growth velocity with film thickness. Nevertheless, several other authors assume the defect density, incorporated in as-deposited grains, to be the reason for microstructural changes in Cu thin films [Detavernier *et al.* 2003a, Detavernier *et al.* 2003b, Patten *et al.* 1971, Nitta *et al.* 1992, Choi *et al.* 2000, Yang and Lee 1999, Jiang *et al.* 1998, Lee *et al.* 2004, Stangl *et al.* 2008, Schell *et al.* 2005]. All of them investigated grain growth during room temperature storage and the same conclusion was found for sputtered and electroplated films. Although some of them observed (100) grain growth, no explanation for the preference of this grain population by defect density minimization was given. Furthermore, some of the studies did not only propose dislocation densities as dominant driving force, but they also highlighted the influence of deposition parameters on dislocation densities and, as a result, on grain growth kinetics.

In 1971, Patten et al. [Patten *et al.* 1971] observed a texture transition from (111) to (100) for very thick (1 mm) Cu films on a Cu substrate during room temperature annealing. However, the driving force for this texture transition cannot be thermal stresses, as the substrate is Cu as well. Therefore the authors postulated

internal stresses due to defects like dislocations which are produced during fabrication as a possible driving force.

Room-temperature grain growth in sputter-deposited Cu films (700 to 1300 nm thick) was investigated by Detavernier et al. [Detavernier *et al.* 2003a]. The observed grain growth was shown to be dependent on the deposition parameters (substrate temperature and sputter gas pressure). Room temperature grain growth was only observed for a low deposition temperature and low Ar pressure, indicating enhanced bombardment by energetic particles. Therefore, the authors ascribe the minimization of defect density to be the main driving force for the microstructural changes.

Lee et al. [Lee *et al.* 2004] analysed the microstructure evolution of 1 µm thick films electroplated at different plating rates (using different plating current densities) during room-temperature storage. They found faster grain growth for an increasing plating rate. TEM observations led to the hypothesis that higher intrinsic stresses introduced by a high defect density from fast deposition rates act as the dominant driving force. Stangl et al. [Stangl *et al.* 2008] adopt this theory when observing an increasing transformation rate for an increasing current density during deposition.

It was shown that the dislocation density plays an important role for microstructural evolution and abnormal grain growth in Cu thin films – not only at room temperature but also at elevated temperatures. Furthermore, it may give the explanation for some unsolved questions.

Greiser et al. [Greiser *et al.* 2001] observed the abnormal growth of (100) oriented grains in 2.0 to 2.4 µm thick Ag films during annealing at temperatures between 250 to 800°C. As their growth had been found in free-standing and stress-free films, strain energy minimization as described by the Thompson model could not be the driving force. On the other hand, abnormal growth had only been found for deposition temperatures below 100°C, where the films did not have the possibility to reduce their defect density. Therefore, the reduction of dislocation density is a possible explanation for the observed results.

6.5 Summary

In this chapter, extensive EBSD maps of thin films with different thicknesses after various heat treatments were presented. They allow a quantification of the texture transformation from (111) to (100), including grain growth kinetics. The following conclusions can be drawn:

1) Only small changes in the initial texture are found for the different film thicknesses. While the fraction of (100) oriented grains remains nearly constant at 6% a slight decrease in the dominant (111) fraction is revealed for increasing film thickness.
2) Abnormal growth of (100) oriented grains was observed during annealing between 90 and 118°C. While abnormal (100) grains were rather rare in the thinnest films, they were even able to become the dominant texture component for the 5 µm thick films.
3) An increased grain growth velocity of the (100) grains was found for increasing film thickness and temperature.
4) Comparison of these growth velocities to possible driving forces indicated that the reduction of dislocation density plays an important role.
5) Analyzing the activation energy of grain growth revealed an increased grain boundary mobility for the (100) grains. This presents a possible explanation of their preferred growth. Additionally, also the model developed by Lee explains why (100) oriented grains are favoured. It predicts that the orientation of the growing grain is determined so that the maximum stress direction is aligned with the minimum Young's modulus direction.
6) A new texture map, considering the minimization of dislocation density as driving force, allows to predict general trends in texture evolution. For more accurate predictions, initial textures as well as kinetics of grain growth have to be considered.
7) The stagnation of grain growth after initial linear growth can either be attributed to the decreased dislocation density or to a stagnation force.

Chapter 7 Summary and Conclusions

The goal of this thesis was to improve the basic understanding of the mechanisms causing grain growth and texture formation in Cu thin films. Measurements of the grain shape and orientation were the first steps towards this objective. In order to carry out tensile and/or annealing experiments, an EBSD-based *in situ* testing appliance was constructed. This system allows the simultaneous observation of grain growth and texture evolution, giving new insight into growth kinetics and details of grain growth.

In a first step, Cu thin films of thicknesses in between 0.5 and 10 µm were deposited on polymer substrates and annealed at 330°C for 30 min. Their resulting texture and microstructure were investigated by EBSD. A texture transition from (111) to (100) was observed at film thicknesses between 3 and 5 µm.

The experimental findings were explained by the texture evolution model of Thompson and Carel [Thompson and Carel 1996a, Thompson and Carel 1996c], which predicts textures of annealed thin films. In this model, the orientation

dependent driving forces, i. e. surface energy minimization and strain energy minimization, are compared. The higher driving force defines the resulting texture. A texture map was calculated for Cu films on the polyimide substrate which predicts a texture transition at a similar film thickness as in the experiments. A significant observation which cannot be explained by a purely energetic argument is the broad texture transition. The reason for this behaviour must lie in the kinetics of texture evolution which will depend on the details of the microstructure. In order to get more information about the critical role of strain energy, uniaxial tensile tests were carried out. Such an experiment has a big advantage over the tests relying on thermal strains: temperature and stress can be uncoupled, and the stress value can be chosen arbitrarily. A texture map, analogous to the biaxial stress state, was calculated. In this map, the driving forces for a 3 µm thick Cu thin film on a polyimide substrate uniaxial stress were compared. The comparison revealed a dominant strain energy minimization above an elastic strain of 0.12%. Therefore (100) grains were expected to grow when applying a strain above this specific limit.

In contrast to these theoretical predictions, various tensile tests revealed no influence of strain on grain growth behaviour. Neither at room temperature nor at elevated temperatures, further (100) grain growth was observed. Therefore, purely energetic considerations cannot explain these results. In order to get more additional insight into grain growth, more *in situ* tests were needed.

In a next step, the abnormal growth of individual (100) oriented grains was recorded for more than 24 hours at temperatures between 90 and 118°C. Annealing was carried out inside a Leo 1530-VP SEM equipped with a heating facility. For the first time, EBSD *in situ* measurements lasting more than 24 hours were carried out for different temperatures and film thicknesses.

Only small changes in the initial texture were found for the different film thicknesses. While the volume fraction of (100) oriented grains remained nearly constant at 6% a slight decrease in (111) fraction was observed for increasing film thickness.

Detailed analysis of grain growth and estimates of the possibly acting driving forces indicated that the reduction of dislocation density played an important role for abnormal grain growth. A further hint for the critical importance of defect density was given by the HWHM of the (100) texture fraction, where a steep decrease was observed.

Nevertheless, it was not clear why this driving force favours the growth of (100) oriented grains. A possible answer could be given by the strain energy release maximization (SERM) model developed by Lee [Lee 1995, Lee 1996]. It predicts that the orientation of the growing grain is determined so that the maximum stress direction is aligned with the minimum Young's modulus direction, therefore giving the explanation for the preferred (100) grain growth. In addition, when analysing the activation energy for grain growth, they are found to possess a higher grain boundary mobility, supporting the preferred growth of (100) oriented grains and giving them their typical fragmented and facetted shape.

Fitting the observed grain growth velocities, an increasing dislocation density was found for increasing film thickness. No explanation can be given for the increase in initial defect density with increasing film thickness. This finding should be the subject of future investigations.

Nevertheless, considering typical dislocation densities in thin films, the driving force due to dislocation density minimization has to be considered when trying to predict texture evolution. A new texture map which includes this driving force is in good accordance to the observed results.

The knowledge that the minimization of dislocation density favours the growth of (100) oriented grains, includes the possibility to taylor the films texture through changes in the deposition parameters, presenting a powerful tool to influence the mechanical properties of thin films.

Chapter 8 Appendix

8.1 *Calculation of the strain energy density*

8.1.1 Biaxial stress state

During thermal treatment different thermal expansion coefficients of film and substrate result in a biaxial stress state in thin films. This biaxial stress state is described by the stress tensor σ_{ij} and the strain tensor ε_{kl}

$$\sigma_{ij} = \begin{pmatrix} \sigma_{11} & 0 & 0 \\ 0 & \sigma_{11} & 0 \\ 0 & 0 & 0 \end{pmatrix} \qquad \varepsilon_{kl} = \begin{pmatrix} \varepsilon_{11} & 0 & 0 \\ 0 & \varepsilon_{11} & 0 \\ 0 & 0 & \varepsilon_{33} \end{pmatrix} \qquad \text{(A1)}$$

Hooke's law links the stress tensor σ_{ij} to the strain tensor ε_{kl}

$$\sigma_{ij} = C_{ijkl}\varepsilon_{kl}\ . \qquad \text{(A2)}$$

The 4th order stiffness tensor C_{ijkl} containing 81 elastic coefficients links the stress and strain tensor. It is often useful to express the anisotropic form of Hooke's law in matrix notation, also called Voigt notation. For this simplification, the symmetry of the stress and strain tensors are considered and they are expressed as six-dimensional vectors in an orthonormal coordinate system.

$$\begin{pmatrix}\sigma_{11}\\ \sigma_{22}\\ \sigma_{33}\\ \sigma_{23}\\ \sigma_{13}\\ \sigma_{12}\end{pmatrix} \equiv \begin{pmatrix}\sigma_{1}\\ \sigma_{2}\\ \sigma_{3}\\ \sigma_{4}\\ \sigma_{5}\\ \sigma_{6}\end{pmatrix} \quad \text{and} \quad \begin{pmatrix}\varepsilon_{11}\\ \varepsilon_{22}\\ \varepsilon_{33}\\ 2\varepsilon_{23}\\ 2\varepsilon_{13}\\ 2\varepsilon_{12}\end{pmatrix} \equiv \begin{pmatrix}\varepsilon_{1}\\ \varepsilon_{2}\\ \varepsilon_{3}\\ \varepsilon_{4}\\ \varepsilon_{5}\\ \varepsilon_{6}\end{pmatrix} \qquad \text{(A3)}$$

Therefore the stiffness tensor is reduced to a 6×6 matrix. This stiffness matrix includes the same information about the elastic properties of the crystal as the stiffness tensor, but it is not possible to transform it like a tensor. To transform it to other axes it is necessary to go back to the tensor notation.

As stress tensor and strain tensor are symmetric by definition, this holds also for the stiffness tensor C_{ijkl} and the stiffness matrix C_{ij}. As a consequence the number of independent components of the tensor/matrix reduces to 21. The presence of symmetry in the crystal reduces still further the number of independent c_{ij} – in a cubic system to 3. Hooke's law for a cubic system is then

$$\begin{pmatrix}\sigma_{1}\\ \sigma_{2}\\ \sigma_{3}\\ \sigma_{4}\\ \sigma_{5}\\ \sigma_{6}\end{pmatrix} = \begin{pmatrix} C_{11} & C_{12} & C_{12} & 0 & 0 & 0\\ C_{12} & C_{11} & C_{12} & 0 & 0 & 0\\ C_{12} & C_{12} & C_{11} & 0 & 0 & 0\\ 0 & 0 & 0 & C_{44} & 0 & 0\\ 0 & 0 & 0 & 0 & C_{44} & 0\\ 0 & 0 & 0 & 0 & 0 & C_{44}\end{pmatrix} \cdot \begin{pmatrix}\varepsilon_{1}\\ \varepsilon_{2}\\ \varepsilon_{3}\\ \varepsilon_{4}\\ \varepsilon_{5}\\ \varepsilon_{6}\end{pmatrix}. \qquad \text{(A4)}$$

For the biaxial stress state this looks like

$$\begin{pmatrix}\sigma_{1}\\ \sigma_{1}\\ 0\\ 0\\ 0\\ 0\end{pmatrix} = \begin{pmatrix} C_{11} & C_{12} & C_{12} & 0 & 0 & 0\\ C_{12} & C_{11} & C_{12} & 0 & 0 & 0\\ C_{12} & C_{12} & C_{11} & 0 & 0 & 0\\ 0 & 0 & 0 & C_{44} & 0 & 0\\ 0 & 0 & 0 & 0 & C_{44} & 0\\ 0 & 0 & 0 & 0 & 0 & C_{44}\end{pmatrix} \cdot \begin{pmatrix}\varepsilon_{1}\\ \varepsilon_{1}\\ \varepsilon_{3}\\ 0\\ 0\\ 0\end{pmatrix} = \begin{pmatrix} C_{11}\varepsilon_1 + C_{12}\varepsilon_1 + C_{12}\varepsilon_3\\ C_{12}\varepsilon_1 + C_{11}\varepsilon_1 + C_{12}\varepsilon_3\\ C_{12}\varepsilon_1 + C_{12}\varepsilon_1 + C_{11}\varepsilon_3\\ 0\\ 0\\ 0\end{pmatrix} \qquad \text{(A5)}$$

As $\sigma_3 = 0$, the strain normal to the films surface ε_3 is linked to the strain in the film plane ε_1 as

$$\varepsilon_3 = -\frac{2C_{12}}{C_{11}}\varepsilon_1 \tag{A6}$$

Hence, a relation between the strain and the stress is found

$$\sigma_1 = \left(C_{11} + C_{12} - \frac{2{C_{12}}^2}{C_{11}} \right) \cdot \varepsilon_1 \equiv M_{100} \cdot \varepsilon_1 \tag{A7}$$

The constant which links the strain ε_1 to the stress σ_1 is called biaxial modulus M. As the stress tensor refers to a (100) oriented system, the calculated modulus is the biaxial modulus of a (100) oriented grain.
Transforming the stiffness tensor, the biaxial moduli of different orientations can be calculated [Zhang *et al.* 2002b].

For the biaxial stress state, the strain energy density is calculated with eq. A1 to

$$W_\varepsilon = \frac{1}{2} \begin{pmatrix} \varepsilon_1 \\ \varepsilon_1 \\ \varepsilon_3 \\ 0 \\ 0 \\ 0 \end{pmatrix} \cdot \begin{pmatrix} C_{11} & C_{12} & C_{12} & 0 & 0 & 0 \\ C_{12} & C_{11} & C_{12} & 0 & 0 & 0 \\ C_{12} & C_{12} & C_{11} & 0 & 0 & 0 \\ 0 & 0 & 0 & C_{44} & 0 & 0 \\ 0 & 0 & 0 & 0 & C_{44} & 0 \\ 0 & 0 & 0 & 0 & 0 & C_{44} \end{pmatrix} \cdot \begin{pmatrix} \varepsilon_1 \\ \varepsilon_1 \\ \varepsilon_3 \\ 0 \\ 0 \\ 0 \end{pmatrix} \tag{A8}$$

and using eq. 1.7, the result can be summarized. The strain energy density is the product of the biaxial modulus and the square of the applied strain.

$$W_\varepsilon = \frac{1}{2} \begin{pmatrix} \varepsilon_1 \\ \varepsilon_1 \\ \varepsilon_3 \\ 0 \\ 0 \\ 0 \end{pmatrix} \cdot \begin{pmatrix} \left(C_{11} + C_{12} - \frac{2{C_{12}}^2}{C_{11}} \right) \cdot \varepsilon_1 \\ \left(C_{11} + C_{12} - \frac{2{C_{12}}^2}{C_{11}} \right) \cdot \varepsilon_1 \\ 0 \\ 0 \\ 0 \\ 0 \end{pmatrix} = \left(C_{11} + C_{12} - \frac{2C_{12}}{C_{11}} \right) {\varepsilon_1}^2 = M_{100} {\varepsilon_1}^2 \tag{A9}$$

The strain energy density for different crystallographic orientations can be calculated through inserting different biaxial moduli.

8.1.2 Uniaxial stress state

The uniaxial stress state is presented by the stress and strain matrix σ_i and ε_j

$$\sigma_i = \begin{pmatrix} \sigma_1 \\ 0 \\ 0 \\ 0 \\ 0 \\ 0 \end{pmatrix} \quad \text{and} \quad \varepsilon_j = \begin{pmatrix} \varepsilon_1 \\ \varepsilon_2 \\ \varepsilon_3 \\ 0 \\ 0 \\ 0 \end{pmatrix} \tag{A10}$$

where $\varepsilon_2 = \varepsilon_3$.
Using these matrices for the calculation of the strain energy density, the following relationship is found.

$$W_\varepsilon = \frac{1}{2} \begin{pmatrix} \varepsilon_1 \\ \varepsilon_2 \\ \varepsilon_2 \\ 0 \\ 0 \\ 0 \end{pmatrix} \cdot \begin{pmatrix} C_{11} & C_{12} & C_{12} & 0 & 0 & 0 \\ C_{12} & C_{11} & C_{12} & 0 & 0 & 0 \\ C_{12} & C_{12} & C_{11} & 0 & 0 & 0 \\ 0 & 0 & 0 & C_{44} & 0 & 0 \\ 0 & 0 & 0 & 0 & C_{44} & 0 \\ 0 & 0 & 0 & 0 & 0 & C_{44} \end{pmatrix} \cdot \begin{pmatrix} \varepsilon_1 \\ \varepsilon_2 \\ \varepsilon_2 \\ 0 \\ 0 \\ 0 \end{pmatrix} \tag{A11}$$

as $\sigma_2 = \sigma_3 = 0$ this equation simplifies to

$$W_\varepsilon = \frac{1}{2}\left(C_{11} - \frac{2C_{12}^2}{\left(C_{11} + C_{12}\right)} \right) \varepsilon_1{}^2 \equiv \frac{1}{2} E_{100} \varepsilon_1{}^2 \equiv U \tag{A12}$$

The factor which links the strain energy density to the elastic strain is the uniaxial Young's modulus. Again a transformation of the stiffness tensor is necessary to calculate Young's Modulus for an orientation different to (100).

Chapter 9 Deutsche Zusammenfassung

Einleitung

Der technologische Fortschritt der letzen Jahrzehnte wurde im Wesentlichen durch die Mikroelektronik ermöglicht. Sie findet ihre Anwendung nicht nur in Hochleistungscomputern und modernen Fertigungsmaschinen sondern auch in unzähligen Gegenständen des Alltags (Handys, Homecomputern, Digicams, Spielkonsolen,…). Dabei spielen dünne Metallschichten eine entscheidende Rolle. Denn neben den elektronischen und magnetischen Eigenschaften sind auch deren mechanische Eigenschaften entscheidend um Funktionalität und eine ausreichende Lebensdauer zu gewährleisten.

Die mechanischen Eigenschaften wiederum sind abhängig von der Textur der Schicht und damit von der Orientierung der einzelnen Körner. Und obwohl es zahlreiche Untersuchungen zu diesem Thema gab, sind die Mechanismen und

zugrunde liegenden Triebkräfte des Kornwachstums und Texturentwicklung nicht vollständig aufgeklärt.

Ziel dieser Arbeit ist es nun, hier Antworten zu finden. Aus der Beobachtung der Texturen und deren Entwicklung in Cu-Schichten sollen tiefere Einblicke in die zugrunde liegenden Mechanismen gewonnen werden.

Experimentelles

Um das Ziel dieser Arbeit erreichen zu können, musste eine neue *in situ* Apparatur entwickelt werden. Mit ihrer Hilfe war es möglich, uniaxiale Zugversuche und/oder Glühexperimente in einem Rasterelektronenmikroskop durchzuführen. Zusätzlich bietet die Apparatur durch eine Verkippung der Probe um 70° die Möglichkeit, während der Zug- bzw. Glühversuche gleichzeitig EBSD Messungen durchzuführen.

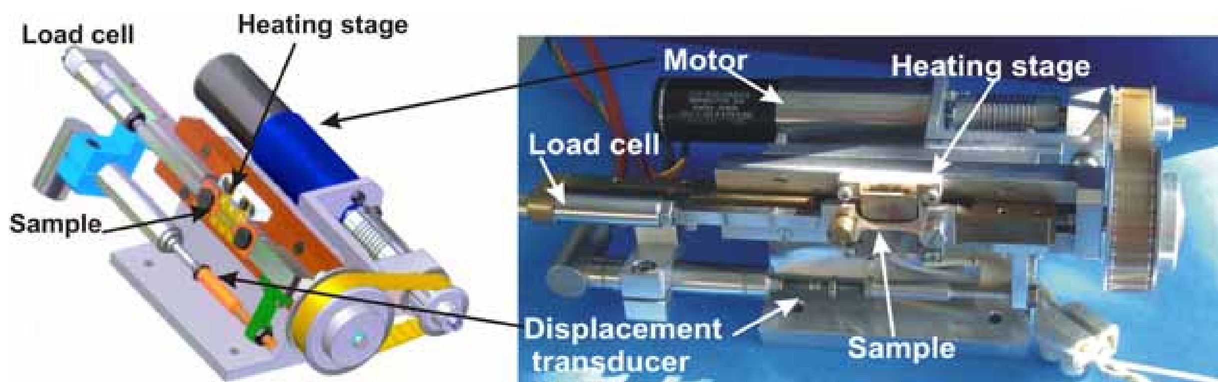

Abbildung 9.1: *In situ* Apparatur: Zugversuche und/oder Glühexperimente sind damit im Rasterelektronenmikroskop durchführbar. Durch die Verkippung der Probenhalterung sind gleichzeitig EBSD-Messungen möglich.

Die EBSD Technik wurde im letzten Jahrzehnt zu einer der meist genutzten Methoden der Orientierungsbestimmung von Materialien. Diese Entwicklung wurde durch immer schnellere Aufnahmeraten ermöglicht, die es erlauben auch Flächen von mehreren μm^2 mit ausreichender Schrittweite in vernünftigen Zeiten (<1h) abzuscannen. Der große Vorteil der EBSD-Technik liegt in der simultanen Bestimmung der Textur und Mikrostruktur, und sie stellt damit eine ideale Methode zur Beobachtung von Texturentwicklungen dar.

Alle Cu-Schichten wurden mittels Magnetron-Sputterns im Ultrahochvakuum hergestellt. Die Schichtdicken lagen im Bereich von 500 nm bis 10 µm. Die

Abscheidung erfolgte bei Raumtemperatur und als Substrat wurden hundeknochenförmige 125 µm dicke Polyimidfolien (Kapton HN, DuPont) verwendet. Die Bestimmung der finalen Glühtextur erfolgte an Proben, die unmittelbar nach der Herstellung für 30 min bei 330°C ausgelagert worden waren. Die *in situ* Kornwachstumsversuche wurden an nicht ausgelagerten, („as-deposited") Schichten durchgeführt.

Ergebnisse und Diskussion

Einfluß der Schichtdicke auf die Textur

Zunächst wurde die Textur von 500 nm bis 10 µm dicken Cu-Schichten bestimmt, die unmittelbar nach der Herstellung für 30 min bei 330°C ausgelagert worden waren. Dabei konnte ein Wechsel von einer dominierenden (111)- zu einer (100)-Textur mit zunehmender Schichtdicke festgestellt werden. Der Übergang zwischen den beiden Texturen erfolgte zwischen 3 und 5 µm Schichtdicke (Abb. 9.2a).

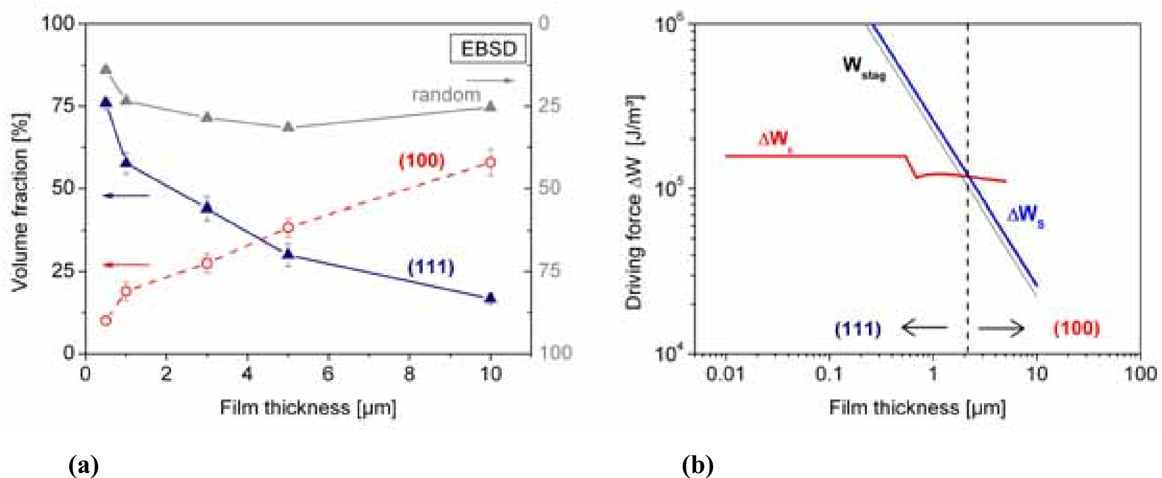

(a) (b)

Abbildung 9.2: (a) Volumenanteile der (111), (100) und random Texturkomponente als Funktion der Schichtdicke. Ein Wechsel von einer dominierenden (111) zu einer (100) Textur kann zwischen 3 und 5 µm beobachtet werden. (b) „Texture-map" für das System Cu-Kapton. Für Schichtdicken oberhalb des Schnittpunktes (strichlierte Linie) wird eine (100) Textur vorhergesagt, während für kleiner Schichtdicken eine (111) Textur zu erwarten ist.

Zur Erklärung dieses Verhaltens wurde das Texturentwicklungsmodell von Thompson [Thompson and Carel 1995, Thompson and Carel 1996b] herangezogen und eine „Texture-map" für das System Cu-Kapton erstellt. Durch einen Vergleich der orientierungsspezifischen Triebkräfte zur Oberflächen- und Grenzflächenenergieminimierung und zur Verzerrungsenergieminimierung konnte

die dominierende Triebkraft bestimmt werden (Abb. 9.2b). Da diese Triebkräfte das Wachstum unterschiedlicher Orientierungen bevorzugen, kann das Auftreten verschiedener Texturen erklärt werden. In dünnen Schichten dominiert die Triebkraft zur Minimierung der Oberflächen- und Grenzflächenenergie, was zur Ausbildung einer (111)-Textur führt. Bei dickeren Schichten kann die Gesamtenergie des Systems durch die Verzerrungsenergieminimierung erreicht werden, was zum bevorzugten Wachstum der (100) orientierten Körner führen sollte. Durch einen Vergleich der Ergebnisse der „Textur-map“ mit den experimentellen Ergebnissen konnte der beobachtete Texturwechsel zufrieden stellend erklärt werden.

Jedoch waren nicht alle Resultate durch das Modell von Thompson erklärbar: So konnte der langsame Wechsel von einer dominierenden (111)- zu einer (100)-Textur damit nicht aufgeklärt werden.

Vergleich EBSD - XRD

Da in der Vergangenheit fast alle Texturmessungen und Orientierungsbestimmungen röntgenographisch erfolgten, war ein weiterer wichtiger Punkt dieser Arbeit der Vergleich der EBSD-Ergebnisse zu röntgenographischen Resultaten. Dazu wurden die gleichen Proben mit EBSD und zwei gebräuchlichen röntgenographischen Methoden untersucht: $\theta/2\theta$– und Polfigurenmessungen wurden den EBSD Ergebnissen gegenübergestellt.

In diesem Zusammenhang wurden auch die Stärken und Schwächen der verschiedenen Methoden offensichtlich. Während sich die röntgenographischen Methoden durch ihren geringen Zeitaufwand und die relativ hohe Eindringtiefe auszeichneten, war es schwierig damit Aussagen über eine eventuell auftretende „random“-Texturkomponente zu treffen. Wurde das berücksichtigt, fand man exzellente Übereinstimmung zwischen den Polfigurmessungen und den Ergebnissen der EBSD-Messungen (Abb. 9.3). Andererseits lieferte die Texturbestimmung mit Hilfe von $\theta/2\theta$ – Messungen nur eine grobe Abschätzung der auftretenden Texturkomponenten. Das lag zum einem an der Tatsache, dass nur Ebenen parallel zur Oberfläche untersucht werden könnten und zum anderen daran, dass nicht alle Reflexe durch die vorgegebene Geometrie erreichbar waren.

Beide Methoden hatten gegenüber EBSD den entscheidenden Nachteil, dass sie keine Ortsinformationen liefern. Bei der EBSD-Methode wird ein Probenbereich

abgerastert und die erhaltenen Orientierungsinformationen können graphisch für jeden Meßpunkt dargestellt werden. Solche Abbildungen können sowohl die Mikrotextur als auch die Mikrostruktur darstellen, und erlauben es somit das Wachstum spezieller Körner detailliert zu beobachten. Andererseits ist eine EBSD-Messung jedoch meist sehr zeitaufwändig und die Informationstiefe beträgt nur einige zehn Nanometern. Zur Verfolgung von Kornwachstum entpuppte sie sich jedoch als außerordentlich leistungsfähige Methode.

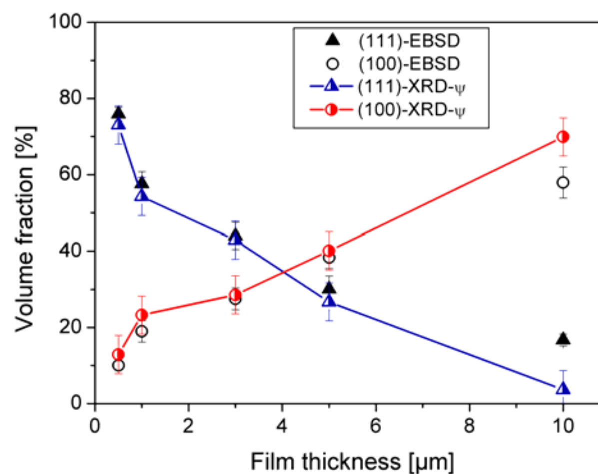

Abbildung 9.3: Vergleich der Texturergebnisse ermittelt durch EBSD und XRD-Polfigurmessungen.

Zugversuche

Da Schichtsysteme immer dann einer zweiachsigen Dehnung unterliegen, wenn eine Temperaturänderung vorgenommen wird, wurde bisher nur dieser Belastungsfall in den Texturmodellen berücksichtigt. Um die Rolle der Verzerrungsenergie aber genauer untersuchen zu können, wurden nun einachsige Zugversuche an den Cu-Schichten durchgeführt. Diese Zugversuche haben den großen Vorteil, dass Dehnung und Temperatur nicht aneinander gekoppelt sind und man damit größere Freiheiten bei der Einstellung der Dehnung hat. Ermöglicht wurden diese Versuche durch die neue *in situ* Apparatur, die Zugversuche bei Raumtemperatur, aber auch bei bis zu 143 °C zuließ.

Zunächst wurde eine „Texture-map“ für eine 3 µm dicke Cu-Schicht auf Kapton unter einachsiger Belastung erstellt. Durch den Vergleich der Triebkräfte konnte vorhergesagt werden, dass oberhalb einer elastischen Dehnung von 0.12% die Verzerrungsenergieminimierung überwiegt und damit das bevorzugte (100)-

Wachstum zu erwarten wäre. Um diese theoretischen Vorhersagen nun experimentell zu überprüfen, wurden *in situ* Zugversuche im Rasterelektronenmikroskop durchgeführt. Besonderes Augenmerk wurde dabei immer Korngrenzen zwischen (111)- und (100)-orientierten Körnern geschenkt. Allerdings konnte zusätzliches (100)-Wachstum weder für ausgelagerte noch für as-deposited Schichten, auch nicht bei höheren Dehnungen, festgestellt werden. Dieses Ergebnis ließ sich nicht durch den Vergleich der Triebkräfte erklären und betonte die Notwendigkeit weitergehender Untersuchungen der Kinetik des Kornwachstums.

Einfluss der Temperatur und der Schichtdicke auf das (100) Kornwachstum

Um tiefere Einblicke in die Texturentwicklung dünner Cu-Schichten zu bekommen, wurden systematisch eine Reihe von *in situ* EBSD Experimenten durchgeführt, bei denen sowohl die Schichtdicke als auch die Auslagerungstemperatur variiert wurden. Zusätzlich wurden die Ausgangstextur und -korngröße der unterschiedlichen Schichtdicken bestimmt.

Aus den *in situ* Messungen konnten folgende Trends identifiziert werden: sowohl der finale (100) Texturanteil als auch die Wachstumsgeschwindigkeit der (100) orientierten Körner nahmen mit der Schichtdicke und der Auslagerungstemperatur zu (Tab. 9.1 und Abb. 9.4).

Tab. 9.1: Kornwachstumsgeschwindigkeit [nm/h] (v_{mean}) der abnormalen (100) orientierten Körner für unterschiedliche Auslagerungstemperaturen (90, 104 und 118°C) und Schichtdicken (1-5 µm).

v_{mean} [nm/h]	90°C	104°C	118°C
5 µm	241 ± 15	400 ± 45	662 ± 73
3 µm	61 ± 35	222 ± 20	404 ± 54
2 µm	58 ± 15	129 ± 22	184 ± 31
1 µm	40 ± 4	53 ± 4	138 ± 30

Durch eine Analyse der Wachstumsgeschwindigkeiten, die Abschätzung der Mobilität und die Bestimmung der wirkenden Triebkraft konnte Überraschendes enthüllt werden: das bevorzugte Wachstum der (100) orientierten Körner konnte nicht durch die Verzerrungsenergieminimierung, verursacht durch die Fehlpassung zwischen Schicht und Substrat, erklärt werden. Aus diesem Grund war es notwendig

auch andere Triebkräfte in Betracht zu ziehen. Ein klarer Hinweis konnte aus der Abschätzung der wirkenden Triebkraft und Röntgenmessungen gewonnen werden, bei denen ein starker Abfall der Versetzungsdichte beobachtet werden konnte.

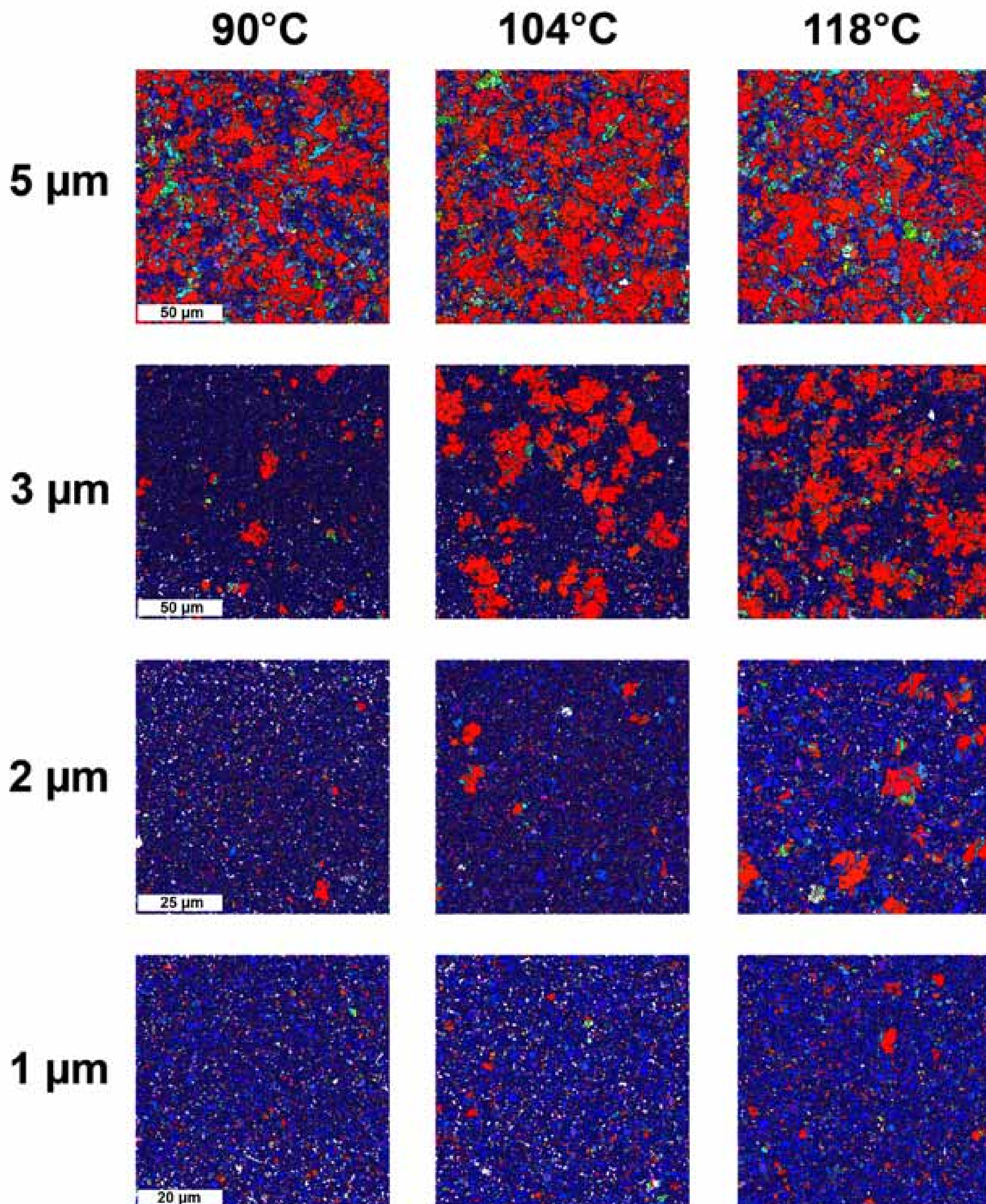

Abbildung 9.4: Endtextur für 1, 2, 3 und 5 µm dicke Cu Schichten nach einer Auslagerung bei 90, 104 and 118°C. Für zunehmende Temperatur und Schichtdicke wird eine Zunahme der (100) Texturkomponente (rot) beobachtet.

Aus diesen Ergebnissen konnte abgeleitet werden, dass der Abbau der Versetzungsdichte eine wichtige Rolle als Triebkraft für das (100)-Wachstum spielt. Eine neue „Texture-map“, die diese Triebkraft enthält, konnte die experimentell beobachteten Ergebnissen zufrieden stellend erklären. Allerdings wurde dadurch auch nochmals verdeutlicht, dass die Ausgangstextur und Kinetik die Endtextur entscheidend beeinflussen können.

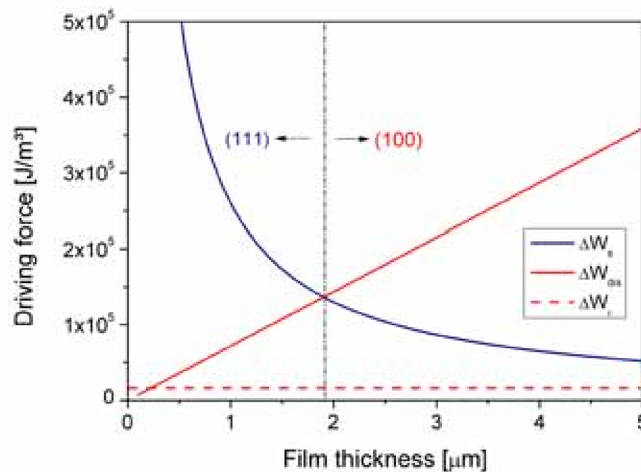

Abbildung 9.5: “Texture map”: Darstellung der Triebkrafte zur Verzerrungsenergieminimierung, ΔW_{ε}, Oberflächenenergieminimierung, ΔW_s, und Versetzungsdichteminimierung, ΔW_{dis}, für Cu-Schichten auf Polyimid. Die Triebkraft zur Minimierung der Versetzungdichte dominiert oberhalb einer Schichtdicke von 1.9 µm, darunter bestimmt die Oberflächenenergieminierung die Texturentwicklung.

Die Bestimmung der Triebkraft lieferte zunächst keine Erklärung für die Bevorzugung des Wachstums von (100) orientierten Körnern.

Analysen der Aktivierungsenergie des abnormalen Wachstums der (100) Körner und Vergleiche mit Literaturergebnissen zeigen, dass diese niedriger liegen als für das normale Kornwachstum. Dadurch kann auf eine erhöhte Mobilität der Korngrenzen der abnormalen (100) Körner geschlossen werden. Die erhöhte Mobilität wiederum erlaubt es den (100)-Körnern unter dem Einfluss einer bestimmten Triebkraft schneller zu wachsen. Auch das strain-energy-release-maximization SERM-Modell von Lee [Lee 1999a] sagt das bevorzugte Wachstum von (100) Körnern unter dem Einfluss von Versetzungen voraus: Lee postulierte, dass sich die rekristallisierten Körner so ausrichten, dass sich deren Richtung mit dem kleinsten E-Modul parallel zur Richtung der höchsten Spannung im verformten Material anordnet. Für (111) und (100) orientierte Schichten wird eine (100)

Rekristallisationstextur vorhergesagt, was sich ebenfalls mit den beobachteten Resultaten deckt.

Zusammenfassung

Durch den Einsatz von EBSD-Messungen konnten auftretende Texturen und deren Entwicklung in Kupferschichten untersucht werden. Dabei wurde festgestellt, dass die Triebkräfte zur Oberflächen- und Grenzflächenenergieminimierung und der Verzerrungsenergieminimierung nicht alle auftretenden Texturentwicklungen zufrieden stellend erklären können. *In situ* Untersuchungen konnten zeigen, dass darüber hinaus die Reduktion der Versetzungsdichte großen Einfluss auf das Kornwachstum und damit die Texturentwicklung in dünnen Cu-Schichten hat. Durch die Berücksichtigung dieser Triebkraft konnte die beobachtete Texturentwicklung erklärt werden. Die Bevorzugung der (100) Texturkomponente ließ sich durch das SERM-Modell von Lee oder eine erhöhte Mobilität der Korngrenzen der (100) Körner beschreiben. Die Offenlegung der Bedeutung der Versetzungsdichte kann dazu beitragen Texturentwicklungen genauer abzuschätzen und vorherzusagen.

Chapter 10 References

Avrami, M. (1939). "Kinetics of phase change. I: General theory." J Chem Phys **7**: 1103-1112.

Beck, P. A. (1952). "Annealing textures in rolled face-centered cubic metals." Trans Am Inst Min Engrs **194**: 83-90.

Beck, P. A. (1991). "Origin of the cube texture in face-centered cubic metals." Trans Am Inst Min Engrs **191**: 474-476.

Beck, P. A., P. R. Sperry and H. Hu (1950). "The orientation dependence of the rate of grain boundary migration." J Appl Phys **21**: 420-425.

Brongersma, H. S., E. Kerr, I. Vervoort and K. Maex (2002a). Grain structure evolution during annealing of electroplated copper. Stress -Induced Phenomena in Metallization: Sixth Int'l. Workshop, 229-234.

Brongersma, H. S., E. Kerr, I. Vervoort, A. Saerens and K. Maex (2002b). "Grain growth, stress, and impurities in electroplated copper." J Mater Res **17**(3): 582-589.

Brongersma, H. S., I. Vervoort, M. Judelewicz, H. Bender, T. Conard, W. Vandervorst, G. Beyer, E. Richard, R. Palmans, S. Lagrange and K. Maex (1999a). Non-correlated behavior of sheet resistance and stress during self-annealing of electroplated copper. Interconnect Technology, IEEE International Conference. San Francisco, CA, USA: 290-292.

Brongersma, S. H., E. Richard, I. Vervoort, H. Bender, W. Vandervorst, S. Lagrange, G. Beyer and K. Maex (1999b). "Two-step room temperature grain growth in electroplated copper." J Appl Phys **86**(7): 3642-3645.

Cabral Jr., C., P. C. Andricacos, L. Gignac, I. C. Noyan, K. P. Rodbell, T. M. Shaw, R. Rosenberg, J. M. E. Harper, P. W. DeHaven, P. S. Locke, S. Malhotra, C. Uzoh and S. J. Klepeis (1999). Room temperature evolution of microstructure and resistivity in electroplated copper films. Proc Adv Metall Conf, Materials Research Society, **14**, 81-87.

Carel, R., C. V. Thompson and H. J. Frost (1996). "Computer simulation of strain energy effects vs. surface and interface energy effects on grain growth in thin films." Acta Mater **44**(6): 2479-2494.

Chan, K. Y., T. Y. Tou and B. S. Teo (2006). "Thickness dependence of the structural and electrical properties of copper films deposited by dc magnetron sputtering technique." Microelectron J **37**: 608-612.

Choi, J. H., S. Y. Kang and D. N. Lee (2000). "Relationship between deposition and recrystallization textures of copper and chromium electrodeposits." J Mater Sci **35**: 4055-4066.

Dahlgren, S. D. (1974). "Columnar grains and twins in high-purity sputter-deposited copper." J Vac Sci Technol **11**(4): 832-836.

Dehm, G., T. J. Balk, H. Edongue and E. Arzt (2003). "Small-scale plasticity in thin Cu and Al films." Microelectron Eng **70**: 412-424.

Detavernier, C., D. Deduytsche, R. L. Van Meirhaeghe, J. De Baerdemaeker and C. Dauwe (2003a). "Room-temperature grain growth in sputter-deposited Cu films." Appl Phys Lett **82**(12): 1863-1865.

Detavernier, C., S. Rossnagel, C. Noyan, S. Guha, C. Cabral Jr. and C. Lavoie (2003b). "Thermodynamics and kinetics of room-temperature microstructural evolution in copper films." J Appl Phys **94**(5): 2874-2881.

Donthu, S. K., M. M. Vora, S. K. Lahiri, C. V. Thompson and S. Yi (2003). "Activation energy determination for recrystallization in electroplated-copper films using differential scanning calorimetry." J Electron Mater **32**: 531-534.

Dupont (2006). DuPont Kapton HN. Available from: www2.dupont.com/Kapton/en_US/assets/downloads/pdf/HN_datasheet.pdf.

Dupont (2008). Kapton - polyimide film. Available from: www.dupont.com\kapton\general\sumofprop.html.

Field, D. P., M. M. Nowell and O. V. Kononenko (2003). "Observation of grain growth in Cu films by in-situ EBSD analysis." Materials, Technology and Reliability for Advanced Interconnects and Low-k Dielectrics - Symposium 2003 (Mater. Res. Soc. Vol.766). Mater. Res. Soc. 2003 **766**: 373-378.

Field, D. P., N. J. Park, P. R. Besser and J. E. J. Sanchez (2005a). "Structure evolution in plated Cu films." Mat Res Soc Symp Proc **863**: 521-526.

Field, D. P., J. E. Sanchez, P. No-Jin and P. R. Besser (2005b). "Texture evolution in thin Cu films and lines." Mater Sci Forum **495-497**: 1323-31.

Flinn, P. A. (1991). "Measurement and interpretation of stress in copper films as a function of thermal history." J Mater Res **6**(7): 1498-1501.

Freund, L. B. (1990). "The driving force for glide of a threading dislocation in a strained epitaxial layer on a substrate." J Mech Phys Solids **38**(5): 657-679.

Freundlich, P., M. Militzer and D. Bizzotto (2002). "Room temperature microstructue evolution in electroplated copper films." Electrochemical Society Proceedings **22**: 76-83.

Frost, H. J., C. V. Thompson and D. T. Walton (1992). "Simulation of thin film grain structures. II. Abnormal grain growth." Acta Metall Mater **40**(4): 779-793.

Gangulee, A. (1972). "The structure of electroplated and vapor-deposited copper films." J Appl Phys **43**(3): 867-873.

Gignac, L. M., K. P. Rodbell, C. Cabral Jr., P. C. Andricacos, P. M. Rice, R. B. Beyers, P. S. Locke and S. J. Klepeis (1999). Characteriation of plated Cu thin film microstructures. Mat Res Soc Symp Proc **562**, 209-214.

Greiser, J. (1999). Anwendung der orientierungsabbildenden Mikroskopie auf die Mikrostrukturenwicklung in dünnen Schichten. Max Planck institute for metal research. Stuttgart, Universität Stuttgart. **Dissertation**.

Greiser, J., P. Müllner and E. Arzt (2001). "Abnormal grain growth of "giant" grains in silver thin films." Acta Mater **49**: 1041-1050.

Gupta, D. (1994). "Comparative Cu diffusion studies in advanced metallizations of Cu and Al-Cu based thin films." Mat Res Soc Symp Proc **337**: 209-215.

Harper, J. M. E., C. Cabral Jr., P. C. Andricacos, L. Gignac, I. C. Noyan, K. P. Rodbell and C. K. Hu (1999). "Mechanism for microstructure evolution in electroplated copper thin films near room temperature." J Appl Phys **86**(5): 2516-2525.

Harper, J. M. E., J. Gupta, D. A. Smith, J. W. Chang and K. L. Holloway (1994). "Crystallographic texture change during abnormal grain growth in Cu-Co thin films." Appl Phys Lett **65**(2): 177-179.

Harris, G. B. (1952). "Quantitative measurements of preferred orientation in rolled uranium bars." Philos Mag **43**: 113-123.

Hau-Riege, S. P. and C. V. Thompson (2000). "In-situ transmission electron microscope studies of the kinetics of abnormal grain growth in eletroplated copper films." Appl Phys Lett **76**(3): 309-311.

Hillert, M. (1965). "On the theory of normal and abnormal grain growth." Acta Metall **13**: 227-238.

Hillert, M. (1996). "Analytical Treatments of Normal Grain Growth." Mater Sci Forum **204-206**: 3-18.

Hommel, M. and O. Kraft (2001). "Deformation behavior of thin copper films on deformable substrates." Acta Mater **49**(19): 3935-3947.

Hong, B., C.-H. Jiang and X.-J. Wang (2006). "Texture of electroplated Cu film under biaxial stress." Mater Trans **47**(9): 2299-2301.

Hong, B., C.-H. Jiang and X.-J. Wang (2007). "XRD characterization of texture and internal stress in electrodeposited copper films on Al substrates." Powder Diffraction **22**(4): 324-327.

Huang, Y. and F. J. Humphreys (1999). "Measurements of grain boundary mobility during recrystallization o f a single-phase aluminium alloy." Acta Mater **47**(7): 2259-2268.

Humphreys, F. and M. Hatherly (1995). Recrystallization and related annealing phenomena. Oxford, Pergamon.

Hyo-Jong, L., H. Heung Nam, K. Do Hyun, L. Ui-hyoung, O. Kyu Hwan and C. Pil-Ryung (2006). "In situ observation of the grain growth of the copper electrodeposits for ultralarge scale integration." Appl Phys Lett **89**(16): 161924-1-3.

Inman, M. C. and H. R. Tipler (1963). "Interfacial energy and composition in metals and alloys." Metal Rev **8**(30): 105-166.

Jakkaraju, R. and A. L. Greer (2002). "Texture and hillocking in sputter-deposited copper thin films." J Mater Sci **13**: 285-294.

Jiang, Q. T., R. Mikkola, B. Carpenter and M. E. Thomas (1998). Room temperature film property changes in electro-deposited Cu thin films. Adv metall conf 1998, Colorado Springs, Materials Research Society, 177-181.

Johnson, W. A. and R. F. Mehl (1939). "Reaction kinetics in processes of nucleation and growth." Trans Am Inst Min Metall Pet Eng **135**: 416-442.

Knorr, D. B. and D. P. Tracy (1995). "A review of microstructure in vapor deposited copper thin films." Mater Chem Phys **41**: 206-216.

Knuyt, G., C. Quaeyhaegens, J. D'Haen and L. M. Stals (1995). "A quantitative model for the evolution from random orientation to a unique texture in PVD thin film growth." Thin Solid Films **258**: 159-169.

Koike, J., M. Wada, M. Sanada and K. Maruyama (2002). "Effects of crystallographic texture on stress-migration resistance in copper thin films." Appl Phys Lett **81**(6): 1017-1019.

Kolmogorov, A. N. (1937). "Statistical theory of crystallization of metals." Izv. Akad. Nauk SSSR Ser. Mat. **1**: 355-359.

Kuschke, W.-M., A. Kretschmann, R.-M. Keller, R. P. Vinci, C. Kaufmann and E. Arzt (1998). "Textures of thin copper films." J Mater Res **13**(10): 2962-2968.

Kwon, K.-W., C. Ryu and R. Sinclair (1997). "Evidence of heteroepitaxial growth of copper on beta-tantalum." Appl Phys Lett **71**: 3069-3071.

Lagrange, S., S. H. Brongersma, M. Judelewicz, A. Saerens, I. Vervoort, E. Richard, R. Palmans and K. Maex (2000). "Self-annealing characterization of electroplated copper films." Microelectron Eng **50**: 449-457.

Lee, D. N. (1989). "A model for development of orientation of vapour deposits." J Mater Sci **24**: 4375-4378.

Lee, D. N. (1995). "The evolution of recrystallization textures from deformation textures." Scripta Metall Mater **32**(10): 1689-1694.

Lee, D. N. (1996). "Maximum energy release theory for recrystallization textures." Metals and Materials **2**(3): 121-131.

Lee, D. N. (1999a). "Strain energy release maximation model for recrystallization textures." Metals and Materials **5**(5): 401-417.

Lee, D. N. (1999b). "Textures and structures of vapor deposits." J Mater Sci **34**: 2575-2582.

Lee, D. N. (2000). "Strain energy release maximization model for evolution of recrystallization textures." Intern J Mech Sci **42**: 1645-1678.

Lee, D. N. (2002). "Texture development in thin films." Mater Sci Forum **408-412**: 75-94.

Lee, D. N. (2005a). "Annealing textures of thin films and Copper interconnects." Mater Sci Forum **475-479**: 1-8.

Lee, D. N. (2005b). "Current understanding of annealing texture evolution in thin films and interconnects." Z Metallkd **96**: 259-268.

Lee, H., S. D. Lopatin and S. S. Wong (2000). Correlation of stress and texture evolution during self- and thermal annealing of electroplated Cu films. International Interconnect Technology 2000, 114-116.

Lee, H., W. D. Nix and S. S. Wong (2004). "Studies of the driving force for room-temperature microstructure evolution in electroplated copper films." J Vac Sci Technol **B 22**(5): 2369-2374.

Lee, S. H. and N. J. Park (2007). "Texture Evolution in the Sputtered and Electro-deposited Cu Thin Films Using EBSD Method." Solid State Phenomena **124-126**: 215-218.

Ling, S. and M. Anderson (1992). "Monte Carlo Simulation of Grain Growth and Recrystallization in polycrystalline materials." JOM **44**: 30-36.

Lingk, C. and M. E. Gross (1998). "Recrystallization kinetics of electroplated Cu in damascene trenches at room temperature." J Appl Phys **84**(10): 5547-5553.

Lingk, C., M. E. Gross and W. L. Brown (2000). "Texture development of blanket electroplated copper films." J Appl Phys **87**(5): 2232-2236.

Lucks, I., P. Lamparter and E. J. Mittemeijer (2004). "An evaluation of methods of diffraction-line broadening analysis applied to ball-milled molybdenum." J Appl Cryst **37**: 300-311.

Militzer, M., P. Freundlich and D. Bizzotto (2004). "Abnormal grain growth in electrochemically deposited Cu films." Mater Sci Forum **467-470**: 1339-1344.

Mirpuri, K., H. Wendrock, S. Menzel, K. Wetzig and J. Szpunar (2006). "Texture evolution in copper film at high temperature studied in situ by electron back-scatter diffraction." Thin Solid Films **496**: 703-717.

Molodov, D. A., L. S. Shvindlerman and G. Gottstein (2003). "Impact of grain boundary character on grain boundary kinetics." Z Metallkd **94**(10): 1117-1126.

Mönig, R. (2005). Thermal fatigue of Cu thin films. Max Planck institute for metal research. Stuttgart, University of Stuttgart. **Dissertation**.

Moriyama, M., K. Matsunaga, T. Morita, S. Tsukimoto and M. Murakami (2004). "The effect of strain distribution on abnormal grain growth in Cu thin films." Mater Trans **45**(10): 3033 - 3038.

Moriyama, M., K. Matsunaga and M. Murakami (2003). "The effect of strain on abnormal grain growth in Cu thin films." J Electron Mater **32**(4): 261-267.

Mullins, W. W. (1958). "The effect of thermal grooving on grain boundary motion." Acta Metall **6**: 414-427.

Murakami, M., M. Moriyama, S. Tsukimoto and K. Ito (2005). "Grain Growth Mechanism of Cu Thin Films." Mater Trans **46**(7): 1737-1740.

Nitta, T., T. Ohmi, M. Otsuki, T. Takewaki and T. Shibata (1992). "Electrical properties of giant-grain copper thin films formed by a low kinetic energy particle process." J Electrochem Soc **139**(3): 922-927.

Nix, W. D. (1989). "Mechanical properties of thin films." Metal Trans A **20 A**: 2217-2245.

Novikov, V. (2004). "Grain growth in films with initial 3D microstructure." Mater Sci Forum **467-470**: 1087-1092.

Novikov, V. I. (1997). Grain growth and control of microstructure and texture in polycrystalline materials. Boca Raton, Florida, CRC Press.

Noyan, I. C. and L. B. Cohen (1987). Residual stress: Measurement by diffraction and interpretation. New York, Springer-Verlag.

Ohmi, T., T. Saito, M. Otsuki, T. Shibata and T. Nitta (1991). "Formation of copper thin films by a low kinetic energy paricle process." J Electrochem Soc **138**(4): 1089-1097.

Okolo, B., P. Lamparter, U. Welzel, T. Wagner and E. J. Mittemeijer (2005). "The effect of deposition parameters and substrate surface condition on texture, morphology and stress in magnetron-sputter-deposited Cu thin films." Thin Solid Films **474**: 50-63.

Oxford (2007). Nordlys EBSD Detector. available from: www.oxford-instruments.com/products/microalaysis/ebsd/detectors.

Pantleon, K. and M. A. J. Somers (2006a). "In situ investigation of the microstructure evolution in nanocrystalline copper electrodeposits at room temperature." J Appl Phys **100**: 114319-1 - 114319-7.

Pantleon, K. and M. A. J. Somers (2006b). "X-ray diffraction investigation of self-annealing in nanocrystalline copper electrodeposits." Scripta Mater **55**: 283-286.

Pantleon, K. and M. A. J. Somers (2007). "Evolution of the microstructure in electrochamically deposited copper films at room temperature." Mater Sci Forum **558-559**: 1261-1264.

Park, N. J. and D. P. Field (2006). "Predicting thickness dependent twin boundary formation in sputtered Cu films." Scripta Mater **54**: 999-1003.

Park, N. J., D. P. Field, M. M. Nowell and P. R. Besser (2005). "Effect of film thickness on the evolution of annealing texture in sputtered copper films." J Electron Mater **34**(12): 1500-1508.

Park, Y.-B., R. Mönig and C. A. Volkert (2007). "Frequency effect on thermal fatigue damage in Cu interconnects." Thin Solid Films **515**: 3252-3258.

Patten, J. W., E. D. McClanahan and J. W. Johnston (1971). "Room-Temperature Recrystallization in Thick Bias-Sputtered Copper Deposits." J Appl Phys **42**(11): 4371-4377.

Perez-Prado, M. T. and J. J. Vlassak (2002). "Microstructural evolution in electroplated Cu thin films." Scripta Mater **47**: 817-823.

Randle, V. (2010). "Grain boundary engineering: an overview after 25 years." Mat Sci and Techn **26**(3): 253-261.

Ritzdorf, T., L. Chen, D. Fulton and C. Dundas (1999). Comparative investigation of plating conditions on self-annealing of electrochemically deposited copper films. Interconnect Technology, IEEE International Conference, San Francisco, CA, USA, 287-289.

Ritzdorf, T., L. Graham, S. Jin, C. Mu and D. Fraser (1998). Self-annealing of electrochemically deposited Copper films in advanced interconnect application. International Interconnect Technology Conference 1998, San Francisco, CA, 166-168.

Rohrer, G. S., D. M. Saylor, B. El Dasher, B. L. Adams, A. D. Rollett and P. Wynblatt (2004). "The distribution of internal interfaces in polycrystals." Z Metallkd **95**(4): 197-213.

Rosi, F. D., Alexander, B.H., Dube, C.A. (1952). "Kinetics and orientation relationships of secondary recrystallization in silver." Trans Am Inst Min Metall Pet Eng **194**: 189.

Saylor, D. M., B. El Dasher, B. L. Adams and G. S. Rohrer (2004). "Measuring the five-parameter grain-boundary distribution form observation of planar sections." Metal Mater Trans A **35A**: 1981-1989.

Schell, N., K. Pagh Andreasen, J. Bottiger and J. Chevallier (2005). "On the dependence on bias voltage of the structural evolution of magnetron-sputtered nanocrystalline Cu films during thermal annealing." Thin Solid Films **476**: 280-287.

Schwaiger, R. and O. Kraft (2003). "Size effects in the fatigue behavior of thin Ag films." Acta Mater **51**: 195-206.

Sekiguchi, A., J. Koike and K. Maruyama (2003). "Microstructural influences on stress migration in electroplated Cu metallization." Appl Phys Lett **83**(10): 1962-1964.

Shan, F. L. and Y. M. Wang (1998). "X-ray profiles analysis on dislocations and hardness of Copper films." Vacuum **5**(3): 381-383.

Skiver, H. L. and N. M. Rosengaard (1992). "Surface energy and work function of elemental metals." Phys Rev B **46**(11): 7157-7168.

Somekh, R. E. (1984a). "Calculation of thermalization during the sputter deposition process." Vacuum **34**(10/11): 987-990.

Somekh, R. E. (1984b). "The thermalization of energetic atoms during the sputtering process." J Vac Sci Technol **A 2**: 1285-1291.

Sonnweber-Ribic, P., G. Dehm, P. Gruber and E. Arzt (2006a). "Strain energy effects on texture evolution in thin films: biaxial vs. uniaxial stress state." AIP Conference Proceedings(816): 192-197.

Sonnweber-Ribic, P., P. Gruber, G. Dehm and E. Arzt (2006b). "Texture transition in Cu thin films: Electron backscatter diffraction vs. X-ray diffraction." Acta Mater **54**(15): 3863-3870.

Srolovitz, D. J., G. S. Grest and M. P. Anderson (1985). "Computer simulation of grain growth. V. Abnormal grain growth." Acta Metall **33**(12): 2233-2247.

Stangl, M., M. Liptak, A. Fletcher, J. Acker, J. Thomas, H. Wendrock, S. Oswald and K. Wetzig (2008). "Influence of initial microstructure and impurities on Cu room-temperature recrystallization (self-annealing)." Microelectron Eng **85**: 534-541.

Surholt, T., Y. M. Mishin and C. Herzig (1994). "Grain-boundary diffusion and segregation of gold in copper: Investigation in the type-B and type-C kinetic regimes." Phys Rev B **50**(6): 3577-3587.

Taheri, M. L., A. D. Rollett and H. Weiland (2004). "In-situ investigation of grain boundary mobility and character in Aluminium alloys in the presence of a stored energy driving force." Mat Res Soc Symp Proc **819**: 6.5.1-6.5.6.

Takayama, S. and M. Oikawa (2005). "The effect of thickness and underlayer on both grain growth and internal stresses in Cu thin films." Mater Sci Forum **502**: 417-422.

Teh, W. H., L. T. Koh, S. M. Chen, J. Xie, C. Y. Li and P. D. Foo (2001). "Study of microstructure and resistivity evolution for electroplated copper films at near-room temperature." Microelectron J **32**: 579-585.

Thompson, C. V. (1985). "Secondary grain growth in thin films of semiconductors: theoretical aspects." J Appl Phys **58**(2): 763-772.

Thompson, C. V. and R. Carel (1995). "Texture development in polycrystalline thin films." Materials Science and Engineering **B 32**: 211-219.

Thompson, C. V. and R. Carel (1996a). "Grain growth and texture evolution in thin films." Mater Sci Forum **204-206**: 83-98.

Thompson, C. V. and R. Carel (1996b). Grain growth and texture evolution in thin films. Grain Growth In Polycrystalline Materials Ii, Pts 1 And 2. **204-:** 83-98.

Thompson, C. V. and R. Carel (1996c). "Stress and grain growth in thin films." J Mech Phys Solids **44**(5): 657-673.

Tracy, D. P. and D. B. Knorr (1993). "Texture and microstructure of thin copper films." J Electron Mater **22**(6): 611-616.

Tracy, D. P., D. B. Knorr and K. P. Rodbell (1994). "Texture in multilayer metallization structures." J Appl Phys **76**(5): 2671-2680.

Ueno, K., T. Ritzdorf and S. Grace (1999). "Seed layer dependence of room-temperature recrystallization in electroplated copper films." J Appl Phys **86**(9): 4930-4935.

Vandermeer, R. A., D. J. Jensen and E. Woldt (1997). "Grain boundary mobility during recrystallization of copper." Metal Mater Trans A **28A**(3): 749-754.

Vanstreels, K., H. S. Brongersma, Z. Tokei, L. Carbonell, W. De Ceuninck, J. D'Haen and M. D'Olieslaeger (2008). "Increasing the mean grain size in copper films and features." J Mater Res **23**(3): 642-662.

Vanstreels, K., S. H. Brongersma, S. Demuynck, L. Carbonell, J. D'Haen, W. De Ceuninck, M. D'Olieslaeger and K. Maex (2006). Super secondary grain growth initiation in electroplated Cu. Adv metall conf 2005, Colorado Springs, Materials Research Society, 615-621.

Vinci, R. P., E. M. Zielinski and J. C. Bravman (1995a). "Effect of copper film thickness on stress and strain in grains of different orientation." Mat Res Soc Symp Proc **356**: 459-464.

Vinci, R. P., E. M. Zielinski and J. C. Bravman (1995b). "Thermal strain and stress in copper thin films." Thin Solid Films **262**(1-2): 142-153.

Viswanathan, R. and C. L. Bauer (1973). "Kinetics of grain boundary migration in copper bicrystals with [001] rotation axes." Acta Metall **21**: 1099 - 1109.

Von Blanckenhagen, B. (2002). Versetzungen in dünnen Metallschichten. Max Planck institute for metal research. Stuttgart, University of Stuttgart. **Dissertation**.

Vook, R. W. and F. Witt (1965a). "Structure and annealing behavior of metal films deposited on substates near 80 K: I. Copper films on glass." J Vac Sci Technol **2**: 49-57.

Vook, R. W. and F. Witt (1965b). "Thermally induced strains in evaporated films." J Appl Phys **36**(7): 2169-2171.

Walther, D., M. E. Gross, K. Evans-Lutterodt, W. L. Brown, M. Oh, S. Merchant and P. Naresh (2000). "Room temperature recrystallization of electroplated copper thin films: methods and mechanisms." Mat Res Soc Symp Proc **612**: D10.1.1-D10.1.10.

Wasa, K. and S. Hayakawa (1992). Handbook of sputter deposition technololy, Noyes Publications.

Weihnacht, V. and W. Brückner (2002). "Abnormal grain growth in (111) textured Cu thin films." Thin Solid Films **418**: 136-144.

Welzel, U. and M. Leoni (2002). "Use of polycapillary X-ray lenses in the X-ray diffraction measurement of texture." J Appl Cryst **35**: 196-206.

Wikström, A. and M. Nygards (2002). "Anisotropy and texture in thin copper films - an elasto-plastic analysis." Acta Mater **50**: 857-870.

Williamson, G. K. and R. E. Smallman (1956). "III: Dislocation densities in some annealed and cold worked metals from measurements on the X-ray debye-scherrer spectrum." Philos Mag **1**(1): 34-46.

Yang, J. and D. N. Lee (1999). "The deposition and recrystallization textures of copper electrodeposits obtained form a copper cyanide bath." Metals and Materials **5**(5): 465-470.

Yin, K. B., Y. D. Xia, C. Y. Chan, W. Q. Zhang, Q. J. Wang, X. N. Zhao, A. D. Li, Z. G. Liu, M. W. Bayes and K. W. Yee (2008). "The kinetics and mechanism of room-temperature microstructural evolution in electroplated copper foils." Scripta Mater **58**: 65-68.

Zhang, J. M., K. W. Xu and V. Ji (2002a). "Competition between surface and strain energy during grain growth in free-standing and attached Ag and Cu films on Si substrates." Appl Surf Sci **187**: 60-67.

Zhang, J. M., K. W. Xu and V. Ji (2002b). "Dependence of strain energy on the grain orientations in an fcc-polycrystalline film on a rigid substrate." Appl Surf Sci **185**: 177-182.

Zielinski, E. M., R. P. Vinci and J. C. Bravman (1994). "Effects of barrier layer and annealing on abnormal grain growth in copper thin films." J Appl Phys **76**(8): 4516-4523.

Zielinski, E. M., R. P. Vinci and J. C. Bravman (1995a). "Effects of barrier layer and processing conditions on thin film Cu microstructure." J Electron Mater **24**(10): 1485-1492.

Zielinski, E. M., R. P. Vinci and J. C. Bravman (1995b). "The influence of strain energy minimization on abnormal grain growth in copper thin films." Materials Reliability in Microelectronics V. Symposium. Mater. Res. Soc. 1995 **391**: 103-108.

Zielinski, E. M., R. P. Vinci and J. C. Bravman (1995c). "The influence of strain energy on abnormal grain growth in copper thin films." Appl Phys Lett **67**(8): 1078-1080.